Modeling Nonlinear Material Behavior at the Nano and Macro Scales

Arun K. Nair

Dissertation submitted to the faculty of the Virginia Polytechnic Institute and State University in partial fulfillment of the requirements for the degree of

Doctor of Philosophy

In

Department of Engineering Science and Mechanics

Dr. Ronald D. Kriz, Co-Chair

Dr. Diana Farkas, Co-Chair

Dr. Michael W. Hyer

Dr. John C. Duke

Dr. Surot Thangjitham

May 12th, 2008.

Blacksburg, Virginia.

Keywords: Nanoindentation, Molecular Dynamics, Embedded Atom Method, Acoustoelastic Theory, Wave propagation in Solids, Stress Induced Anisotropy, Finite Element Method.

Modeling Nonlinear Material Behavior at the Nano and Macro Scales

Arun K. Nair

ABSTRACT

Theoretical and computational methods have been used to study nonlinear effects in the mechanical response of materials at the nano and macro scales. These methods include, acoustoelastic theory, molecular dynamics and finite element models.

The nonlinear indentation response of Ni thin films of thicknesses in the nano scale was studied using molecular dynamics simulations with embedded atom method (EAM) interatomic potentials. The study included both single crystal films and films containing low angle grain boundaries perpendicular to the film surface. The simulation results for single crystal films show that as film thickness decreases, larger forces are required for similar indentation depths but the contact stress necessary to emit the first dislocation under the indenter is nearly independent of film thickness. The presence of grain boundaries in the films leads to the emission of dislocations at a lower applied stress. For a single crystal Ni thin film of a thickness of 20 nm a direct comparison of simulation and experimental results is presented, showing excellent agreement in hardness values. The effects of using different interatomic potentials and indentation rates for the simulations are also discussed. Dynamic indentation of the Ni thin film was also carried out for different frequencies. It has been found that there is a 12% increase in dislocations compared to quasi static indentation and the results are consistent with experiments.

Acoustoelastic theory was used to study how nonlinear elastic properties of unidirectional graphite/epoxy (gr/ep) effect the energy flux deviation due to an applied shear stress. It was found that the quasi-transverse wave (QT) exhibits more flux deviation compared to the quasi-longitudinal (QL) or the pure transverse (PT) due to an applied shear stress. The flux shift in QT wave due to an applied shear stress is higher than that for an applied normal stress along laminate stacking direction for the same magnitude. The QT wave has energy flux deviation due to shear stress at 0^o and 90^o fiber orientations as compared to normal stress case where the flux deviation is zero. It was found that the energy flux shift of QT wave in gr/ep varies linearly with applied shear stress. The Finite element model of the equations of motion combined with the Newmark method in time was used to confirm the flux shift predicted by theory.

Acknowledgements

I would like to thank Dr. Kriz and Dr. Farkas for being such wonderful advisors who supported and guided me throughout this research. Both of them always welcomed new ideas and discussions which were critical in finishing this research. Special thanks to Dr. Kriz for helping me, while I was going through difficult circumstances as a graduate student.

I would also like to thank Prof. Duke, Prof. Hyer and Prof. Thangitham for serving in my committee and taking the time out of their busy schedule. Thanks to Dr. Prosser for being the sixth committee member.

I am indebted to my parents, sister and grandparents (Sreedharan Nair and Shyamala Devi) for their continued support throughout my graduate life. Thanks to Aby Paul, my best friend for his valuable support and guidance, who taught me to do the right things at the right time. I also would like to express my extreme gratitude to Cranwell International Center director Kim Beisecker and the staff for their enormous help while I was in the hospital and afterwards. Special regards to Narayanan sir for his motivation and support.

Thanks to Patrick Shinpaugh and the university visualization and Animation group for helping me with software installations and Virginia Tech research computing facility especially styx and system x.

I am dedicating this dissertation to my mother (Chandramathi), sister (Kanthi) and Dr. Kriz and Kaye Kriz for their unconditional support despite the difficult challenges in their own lives.

Contents

List of Figures

List of Tables

Chapter 1

Introduction

Computational modeling of nonlinear material behavior at the macro scale has been a subject of great interest for many years using continuum theories. Recent development in manufacturing and designing of materials at the nanoscale has further enhanced the need to investigate linear elastic, nonlinear elastic and plastic behavior of materials at such a scale.

The study of mechanical properties of materials is concerned with the deformation of the material under an applied external force as well as the removal of that force. Three different types of mechanical behavior exhibited by material under loading are elastic, anelastic and plastic. Behavior of real materials is a combination of these three types of mechanical behavior and depends on applied load. An understanding of linear and nonlinear elasticity can be gained by considering interatomic bonding in molecules. The total energy of bonding is the sum of attractive and repulsive forces between atoms multiplied by the distance over which they act. Figure 1.1 shows the general shape of variation of potential energy (E) versus the separation distance (R). The equilibrium separation distance is (R_0) where the potential energy (E_0) is at a minimum. The force required to move an atom from the equilibrium position requires external force.

The potential energy curve can be approximated as a quadratic function for small displacements about R_0. The derivative of the potential energy (i.e force) is then a linear curve, thus representing linear elasticity. As the amplitude of displacement becomes larger, the potential energy cannot be represented by a quadratic function; hence, force displacement relationship is no longer linear which gives rise to nonlinear elasticity.

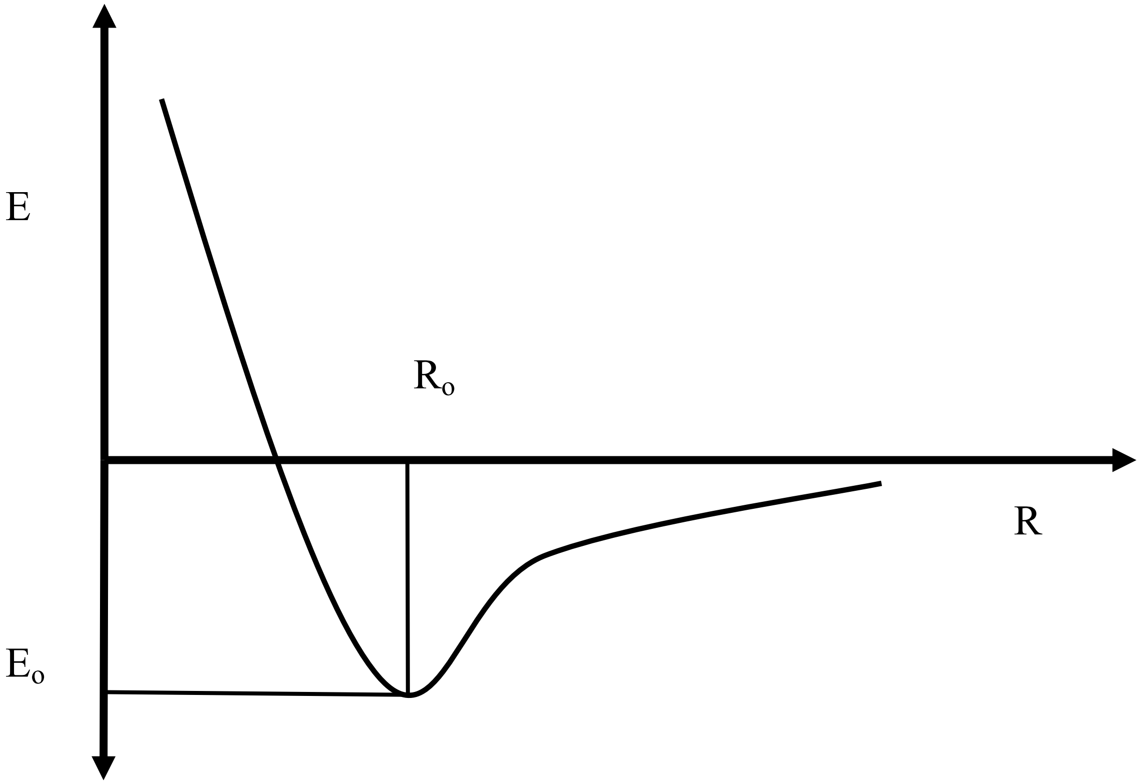

Figure 1.1 Potential Energy (E) and separation distance (R) for interatomic bonding.

The objective of this research is to study the nonlinear material behavior at nano and macro scales using computational methods. In order to study nano scale material behavior, nanoindentation of Nickel (Ni) thin films was carried out using Atomistic simulations. In this research, molecular dynamics simulation is employed to study the nano scale effects, since the continuum theory doesn't address material behavior at nano scale effectively.

However, the ubiquitousness of continuum theories cannot be ignored in this era of multiscale modeling. In order to study the nonlinear material behavior at the macro-scale, nonlinear elastic effects in graphite/epoxy (gr/ep) due to propagation of an ultrasonic wave is chosen. Even though it's interesting to develop methods to improve continuum theories and connect the nano-scale and macro-scale worlds, here the focus remains on analyzing the nonlinear material behavior at both scales separately thereby understanding the basic mechanics involved at each scales. There are two subsections in this section giving introduction to research done at both nano and macro scales.

1.1 Nanoindentation of Thin Films

Nanoindentation is a widely used testing method for the study of material properties of thin films. It is derived from a conventional hardness test, and it is routinely used for evaluation of the elastic modulus besides the hardness. In current instruments, the penetration depth can be in the nanometer range, hence the name 'nano-indentation' technique. A common assumption in the modeling and analysis of indentation is that the indented medium is semi-infinite. However, in many nanoindentation tests the analyzed material is a thin film, deposited on a substrate that can itself be a nano-scale film. These problems are of great interest due to the vast applications of thin film structures and the miniaturization of many devices and components. Nanoindentation based technology has thus been developed in recent years and is an important way of addressing the mechanical properties of thin films, such as hardness.

1.2 Nonlinear elastic effects in graphite/epoxy

Even though the relation between stress and strain in a solid body is described by Hooke's law, which postulates a linear relationship between stress and strain, this linearity breaks down when stiffnesses are found to increase with stress. This increase can be accounted for by additional terms containing the products of the strains in the strain energy density function [1] . The increase of stress is associated with the strain cubed terms or the third order elastic constants. These third order elastic constants are sixth order stiffness tensors, C_{ijlkmn} .

The third order constants have a number of applications in solid state physics including the generation of higher harmonics in finite amplitude ultrasonic waves propagating through a solid medium, certain electronic effects in semiconductors, attenuation of ultrasonic waves, interaction between light and ultrasonic waves, phonon interactions in solids, thermal expansion and the theory of anharmonic crystals [1].

In an anisotropic material three different types of waves that can be propagated through the material are quasi-longitudinal (QL), quasi-transverse (QT) and pure transverse (PT). However in an anisotropic material the direction of energy flux (energy per unit time per unit area) of an ultrasonic plane wave deviates from the intended direction of propagation as compared to an isotropic material, where the energy flux vector, E_i is parallel to the wave front n_i. This phenomenon, exhibited by anisotropic materials, is known as the energy flux deviation (Figure 1.2). The elastic coefficients of the material influence the energy flux deviation [2, 3] . Energy flux deviation was experimentally observed in quartz crystals [4] and unidirectional graphite fiber reinforced epoxy (gr/ep) [5, 6].

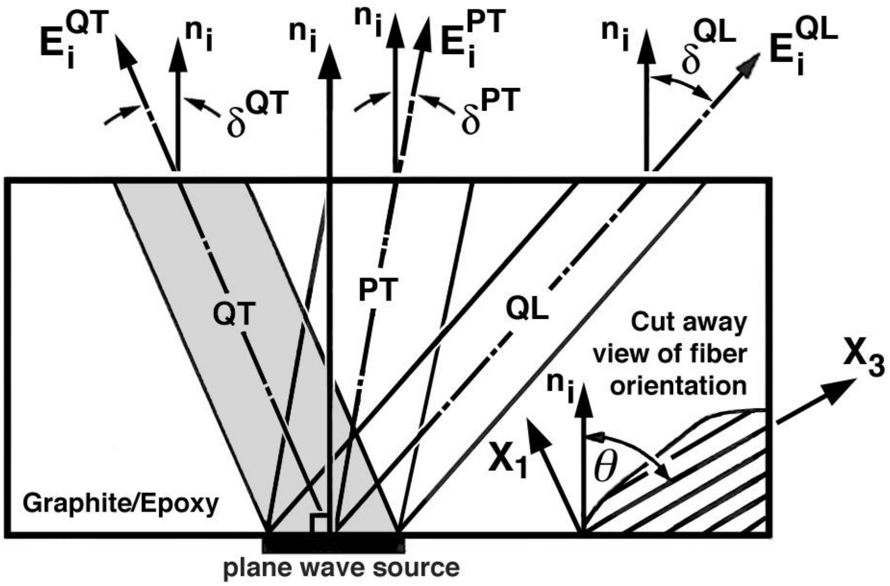

Figure 1.2 Co-ordinate axes defined and fiber orientation of gr/ep laminates.

Nonlinear elastic behavior is generally neglected in ultrasonic wave propagation due to small strains (or small amplitude) imposed on the sample; however this effect can be predominant in three cases of wave propagation as pointed out by Green [4]. First, the amplitude of the wave may be large enough to cause finite strains in the material. In the second case nonlinear behavior occurs when a small amplitude wave is superimposed on a large external static stress. Finally, nonlinear effects are caused by defects in the material. In this research the second case of nonlinear effects is studied for unidirectional gr/ep for the applied shear stress case. The motivation for this research comes from the fact that Prosser et al. [7] studied the energy flux deviation for gr/ep for the applied normal stress case using acoustoelastic theory.

Chapter 2

Background and Theory

2.1 Introduction

In this section the theory and background for nanoindentation and nonlinear elastic effects at macro scale are discussed. The section is divided in two parts; first part comprises a background to nanoindentation and then methodologies used to model nanoindentation such as molecular statics and molecular dynamics. The second part contains an introduction to the acoustoelastic theory and the method employed to find the energy flux deviation using the same. Finally, finite element equations are derived for equations of motion using the variational formulation and the procedure used to integrate these equations of motion in time is discussed.

2.2 Nanoindentation of Thin Films

Experimental studies by Gerberich et al. [8]. and Volinsky et al. [9] have shown that nanoindentation is a reliable and widely used technique for probing mechanical properties of materials.

When addressing properties at the nano-scale new phenomena may appear that is different from the more macroscopic counterparts. For example, the Hall-Petch strengthening with decreasing grain size, typical at the macroscopic scale breaks down at the nanoscale and is actually reversed when the grain sizes are less than 20 nm [10-15]. In another example, size effects have been observed in the mechanical properties of thin FCC films studied by various techniques, including nanoindentation [16-18].

To completely understand mechanical behavior at the nano scale, molecular dynamics computer simulations can be used to model material behavior under various loading conditions. These simulations can reach now the spatial scales typical of nanoindentation and can provide great detail about the mechanisms underlying materials response. Simulations have been used extensively in the past to study the indentation problem and have provided great insight into the actual process of emission of the first dislocations responsible for incipient plasticity as the films are indented [19-26]. Christopher et al. [19] have shown that atomistic modeling was able to reproduce the experimental features like piling-up of material along the indenter sides. Studies conducted by Li et al. [20] described the incipient plasticity due to indentation using atomistic simulation and finite element-modeling for Al. Atomistic/continuum modeling of nanoindentaion was also carried out by Shiari et al. [26] and Iglesias et al. [22]. Lee et al. [24] have also modeled Al and described in detail the homogenous nucleation of dislocations. Szlufarska [27] and Schuh [28] have reviewed recent advances in nanoindentation studies by atomistic modeling. Atomistic simulations also provide trends and information on the mechanisms of plasticity. Most of these studies have been performed in single crystal samples. The effects of random high angle grain boundaries present have been studied by Hasnaoui et al. [29]. Their work showed that the grain boundaries can emit, absorb and repel dislocations. The effects of thickness and geometry of the indenter in nanoindentation of Ni thin films were studied by Parakala et al. [30], showing that there is an indentation size effect irrespective of indenter tip geometries.

Nix et al. [31] have modeled indentation size effects at the micro scale using the concept of geometrically necessary dislocations and found that hardness increases as depth decreases. However, the model does not address the hardness-depth relation for indentation at the nano-scale. Huang et al. [32] developed an analytical model applicable to indentation at the nanometer scale based on maximum allowable geometrically necessary dislocations. Recently, Cordill et al. [33] compared the linear and parabolic hardening models in ultra-small cubes and films and found out that linear hardening model gave a better representation of the early trends in experiments; whereas parabolic hardening model fits later stages . Zhang et al. [34] modeled Tungsten films deposited on an Aluminum substrate using conventional mechanism of strain gradient plasticity theory (CMSG), showing that hardness at the microscopic scale decreases monotonically as the indentation depth increases and doesn't reach a constant macroscopic hardness. Several studies have been carried out on indentation size effects using plasticity theories [35-37]. Chen et al. [38] studied the size dependence in Al films on glass and showed that the hardness increases when the tip approaches the film/substrate interface.

2.2.1 Molecular Dynamics

Classical molecular dynamics [39-41] involves computing the positions and velocities of a finite number of atoms during each time step. Atoms follow Newton's second Law of motion, hence the name classical molecular dynamics. The potential energy of each atom can be computed using quantum mechanics (solving Schrodinger equation) to accurately represent the motion of each atom; however the computational cost involved would make it impossible to consider for large number of atoms.

In a standard MD simulation, general information about the system such as the number of atoms, the type, mass and atomic interactions are first defined. The initial configuration of the system, including the positions of the atoms and their initial velocities at the time t = 0, is then specified. The initial positions are defined according to the crystallographic properties of the material studied. The initial velocities are established as a function of a given initial temperature.

The value of the time step Δt, corresponding to the integration variable, also has to be assigned before the simulation process starts. This value has to be low compared to the highest frequency motion to integrate accurately over all motions, but as large as possible to increase the total time simulated. The first step of the simulation corresponds to the calculation of the forces applied to the atoms at $t = 0$. Then incrementing the value of Δt the actual positions, forces and velocities are successively computed for $t = t + \Delta t$. This process is repeated until the number of iterations chosen is reached.

MD simulation is a useful technique to compute the equilibrium configurations, transport properties or fracture mechanisms of a classical system. The sample is first prepared with a given structure with specific atomic interactions. Then the sample evolves constrained to the equations of motion until its properties do not change with time. Once the nature of the potentials has been determined empirically the MD technique follows the forces on the atoms as they migrate.

The molecular dynamics algorithm used in this research for nanoindentation is as implemented in the LAMMPS code by Plimption [42]. This is a parallelized code and all the simulations were carried out in SYSTEM X (Virginia Tech's super computer). The boundary conditions used are periodic in the directions that are perpendicular to the indentation force. A periodic boundary condition means that atoms can interact across the boundary of the simulation box. The sample sizes in the directions perpendicular to the indentation direction were chosen to be large enough to avoid spurious effects of the periodic boundary conditions used in these directions. In the direction of the indentation force we used a free surface boundary condition for the top of the film and a fixed boundary condition for the bottom of the film, representing a hard substrate. The spherical indenter used is totally rigid and exerts a force on each atom given by [42]:

$$F(r) = -k(r - R)^2 \qquad (2.1)$$

Where k is the specified force constant, r is the distance from the atom to the center of the indenter, and R is the radius of the indenter. The contact area is given by:

$$\text{Area} = 2\,\pi\,\text{Rd} \qquad (2.2)$$

Where R is the radius of the indenter and d is the indentation depth. The areas computed using equation (2.2) has been compared with the areas computed by the direct observation of the indented site. Hence it is concluded that equation (2.2) gives an accurate area as long as the indentation depth remains small compared to the indenter radius. For higher indentation depths the projected contact area is used to find the hardness and is given as

$$\text{Area} = \pi\,(2\text{Rd}-\text{d}^2) \qquad (2.3)$$

2.2.2 Embedded Atom Method

Interatomic potential is an essential part of computational studies as they determine to mimic the interaction between atoms. It is then essential to construct reliable interatomic forces that can reproduce experimental data. This is done using empirical forms which reproduce basic material properties such as lattice constant, heat of solution, and surface energies. The Embedded Atom Method (EAM) originally formulated Dawes and Baskes is a recent approach used to simulate the interaction between atoms in metals and intermetallic compounds [43]. It is based on the Hohenber-Kohn theorem [43], which states that the energy contribution of an atom on its surrounding neighbors is a function of the local electron density due to all the surrounding atoms. This approach becomes particularly important when defects such as vacancy clusters, free surfaces, grain boundaries or dislocation cores are introduced in the material.

The method provides a good description of the interatomic forces in the system, particularly for FCC metals. Based on the EAM approach, the interaction energies of the atoms are composed of two potential functions. A classical pair interaction potential, V (Morse function) describes the attractive and repulsive electrostatic interaction between two atoms. An embedding function, F, takes into account the interaction energy of each atom with the local electron density associated with the neighboring atoms. It calculates the interatomic potentials in metals and models forces between atoms as follows

$$E = \frac{1}{2}\sum_{i,j} V(r_{ij}) + \sum_{i} F(\rho_i) \qquad \rho_i = \sum_{j \neq i} \varphi(r_{ij}) \tag{2.4}$$

Where E is the total energy of the system, $V(r_{ij})$ represents the pair interaction energy between an atom i and its neighboring atom j, $\varphi(r_{ij})$ is the electronic density function, and $F(\rho_i)$ represents an embedding function accounting for the effects of the free electrons in the metal [44]. The interaction energies are however only taken into account within a selected cut-off distance (usually a second closest neighbor distance) and are considered to be zero outside this region. The embedding functions $F(\rho_i)$ and the pair interaction potentials are designed to fit the various physical properties of a system such as lattice constants, elastic constants, and formation energies of diverse defects.

2.2.2.1 EAM potentials for Ni

One of the Ni potential functions used in this research was developed by Mishin et al. [45]. This potential reproduces the perfect lattice properties as well as many properties of metastable phases calculated using first principles techniques. It is particularly important to use a potential that can reproduce off-equilibrium situations, since the atomic configurations that are encountered during indentation are under large compressive stresses and therefore far from perfect lattice equilibrium. The first principle calculations include far from equilibrium configurations such as BCC, HCP and simple cubic Nickel. The potential reproduces these metastable configurations and therefore is expected to hold for the relatively large strains around the tip of the indenter.

Another type of potential for Ni developed by Voter et al. [46], which is also used in some of the simulations done in this research. In order to mimic the classical electrostatic interaction between two spherical atoms the pairwise potential is taken to be a Morse potential. $F(\rho_i)$ is determined in such a way that the potential gives a perfect fit to the experimental values. It is also ensured that the interatomic potential and its derivatives are continuous at all geometries of the system in order to be suitable for molecular static and molecular dynamics simulations. A comparison of two potentials is shown in figure 2.1 [45].

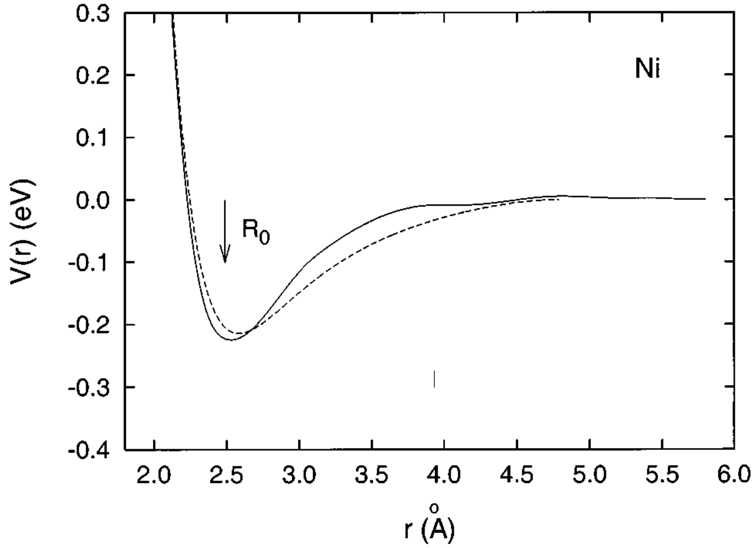

Figure 2.1 Comparison of Voter-chen potential (dashed line) and Mishin-Farkas potential (solid line).

2.2 Nonlinear elastic effects in graphite/epoxy

Tokuoka and Iwashimizu [47] derived the Christoffel equation for an isotropic material under stress assuming hyperelasticity using a plane wave solution. Man and Lu [48] later extended the applicability of Christoffel equation to general types of loading history and plastic deformations. Prosser et al. [7] studied gr/ep for applied stress along fiber axis and laminate stacking direction using acoustoelastic theory and predicted the flux deviation angle. Using Man and Lu's theory [48] Degtyar and Rokhlin [49] derived in detail the equation of motion due to wave propagation superimposed on prestressed solid. Degtyar and Rokhlin [50] also studied the elastic wave propagation between two generally anisotropic stressed solids as well as stressed solid and fluid for different materials. Recently, Zhuk and Guz [51] studied nanocomposite material with prestress, where the nonlinearity was described by the Murnaghan potential. Similarly, Parnell [52] used asymptotic homogenization theory in the deformed configuration to find the effective response of a prestressed nonlinear elastic composite bar. Even though Prosser et al. [7] studied energy flux deviations due to normal stress effects on gr/ep, the flux deviation due to shear stress was left unexplored. In this research the energy flux shift due to applied shear stress is predicted using acoustoelastic theory and these predicted values are confirmed by finite element method.

2.3.1 Acoustoelastic Theory

Nonlinear elasticity can also be understood from the perspective of energy, i.e when strain energy due to deformation is given as a polynomial of strains as [1]

$$\phi = \phi_0 + K_1 C_{ij} S_{ij} + K_2 C_{ijkl} S_{ij} S_{kl} + K_3 C_{ijklmn} S_{ij} S_{kl} S_{mn} \cdots\cdots \tag{2.5}$$

Where ϕ_0 is the initial energy, K_1, K_2 and K_3 are constants, $C_{ij}, C_{ijkl} and C_{ijklmn}$ are the first, second and third order elastic stiffness tensors and S_{ij} is the strain tensor. If the initial energy and deformation of the body are zero, the first two terms in above equation are zero.

$$\phi = K_2 C_{ijkl} S_{ij} S_{kl} + K_3 C_{ijklmn} S_{ij} S_{kl} S_{mn} \cdots\cdots$$

This third order stiffness tensor gives rise to nonlinear elastic effects and has been widely used in acoustoelastic theory for studying there effect in energy flux shifts.

The energy flux vector E_j is related to the elastic stiffness coefficients C_{ijkl} and the spatial and time derivatives of displacement vector u_i by the following equation [2, 3].

$$E_j = -C_{ijkl} (\frac{\partial u_k}{\partial x_l})(\frac{\partial u_i}{\partial t}) \tag{2.6}$$

Acoustoelastic theory is used to include the nonlinear elastic effects on the energy flux deviation. According to the theory the applied stress σ_{ij} changes the linear elastic coefficients to give an effective linear stiffness tensor using the following relation [7].

$$C^*_{nlij} = K_{nlij} + \sigma_{nj} \delta_{li} \tag{2.7}$$

Where C^*_{nlij} is the effective linear stiffness tensor, σ_{nj} is the applied stress, δ_{li} is kronecker delta and K_{nlij} is given by [7]

$$\begin{aligned} K_{nlij} &= C_{nlij} + C_{rlij}\varepsilon_{nr} + C_{nsij}\varepsilon_{ls} + C_{nlpj}\varepsilon_{ip} + C_{nliq}\varepsilon_{jq} + C_{nlijuv}\varepsilon_{uv} + C_{rlijuv}\varepsilon_{uv}\varepsilon_{nr} + C_{nsijuv}\varepsilon_{uv}\varepsilon_{ls} + \\ & C_{nlpjuv}\varepsilon_{uv}\varepsilon_{ip} + C_{nliquv}\varepsilon_{uv}\varepsilon_{jq} \end{aligned} \tag{2.8}$$

In equation (2.8) C_{nlij} is the linear elastic coefficient, C_{nlijuv} is the third order nonlinear elastic coefficient and ε_{nr} is the strain resulting from the applied stress σ_{ij}. The strain can be found as the product of compliance tensor (inverse of C_{nlij}) and the applied stress. The K_{nlij} tensor is composed of ten terms, five linear terms and five nonlinear terms. Equation (2.7) has nine nonzero terms when normal stresses are applied and shear stress is set to zero. The inclusion of shear stress terms will lead to an additional eighteen terms. This is too cumbersome to expand by hand and solve, hence a computer program was used to compute the C^*_{nlij} tensor. For example C^*_{nlij} is nonsymmetric with 81 independent terms and each of these terms is the sum of 27 terms, hence the total number of terms is 2187. Previous investigations did not include both normal and shear stress terms in equation (2.7), because only normal stresses could be measured.

Equation (2.6) can now be written as

$$E_j = -\sigma'_{ij}\left(\frac{\partial u_i}{\partial t}\right); \quad \text{where} \quad \sigma'_{ij} = C^*_{ijkl}\varepsilon'_{kl} \tag{2.9}$$

σ'_{ij} is the stress and ε'_{kl} the strain due to the wave propagation. The christoffel equation for the wave propagation in terms of the effective linear elastic coefficient assuming a plane periodic solution can be written as [47, 49, 53]

$$(C^*_{ijkl} l_l l_j - \rho v^2 \delta_{ik})\alpha_k = 0 \tag{2.10}$$

Where C^*_{ijkl} is the effective linear stiffness tensor, l_l is the direction cosine of the wave normal, δ_{ik} is kronecker delta and α_k is the eigenvector or the direction cosine of particle displacement vector corresponding to each eigenvalue ρv^2 (ρ is the density and v is velocity). The energy (from equation (2.6)) is time averaged over one cycle to get $\overline{E_i}$, where $\overline{E_i} = \sigma'_{ik}\,\alpha_k$. The total energy over one cycle is defined as $\overline{E}_T^2 = \overline{E}_1^2 + \overline{E}_2^2 + \overline{E}_3^2$, hence the direction cosines of energy flux vector is given as a=$\frac{\overline{E_1}}{\overline{E_T}}$, b=$\frac{\overline{E_2}}{\overline{E_T}}$ and c=$\frac{\overline{E_3}}{\overline{E_T}}$.

The flux deviation angle (δ) in Figure 1.2 is computed as the difference between the angle (θ) that energy flux vector makes with the x_3 axis and the wave normal vector (n_i) makes with respect to the x_3 axis. Mathematically, the flux deviation angle (δ can be represented as follows:

$$\delta = \tan^{-1}((\tan\beta - \tan\theta)/(1 - \tan\beta\tan\theta)) \qquad (2.11)$$

Where tan β=a/c is defined in terms of the direction cosines of energy flux vector. The use of tangent function takes care of the sign of the flux deviation angle for each wave QL, QT and PT.

2.3.2 Finite Element Formulation

In order to confirm the results predicted by Acoustoelastic theory, Finite element method [54] along with Newmark's method [55] in time is used to solve the equation of motion at each time step. The procedure is described here in detail.

The equation for small elastic motion due to wave propagation superimposed on a prestressed state in the absence of body forces can be written as

$$\sigma'_{ij,j} = \rho u_{i,tt} \qquad (2.12)$$

Where σ'_{ij} is the stress defined by equation (2.9), ρ is the density and u_i is the displacement as a result of wave propagation in the material. The weak form [56] is constructed by multiplying equation (2.12) by arbitrary functions which represent virtual displacements δu_i.

$$\int_V \delta u_i (\sigma'_{ij,j} - \rho u_{i,tt}) dV = 0 \tag{2.13}$$

Integrating the above equations by parts and using divergence theorem gives the weak form of the governing equations as follows

$$0 = \int_V (\sigma'_{ij} \delta\varepsilon_{ij} + \delta u_i \rho u_{i,tt}) dV - \oint_S (\sigma'_{ij} n_j \delta u_i) dS \tag{2.14}$$

Substituting $\sigma'_{ij} = C^*_{ijkl}\varepsilon'_{kl}$, $u_1 = u$, $u_2 = v$ and $u_3 = w$ and assuming plain strain conditions $(\frac{\partial u_2}{\partial x_1} = \frac{\partial u_2}{\partial x_2} = \frac{\partial u_2}{\partial x_3} = \frac{\partial u_1}{\partial x_2} = \frac{\partial u_3}{\partial x_2} = 0)$, equation (2.14) can be written over the domain Ω as

$$\begin{aligned}&\int_\Omega \left\{ \frac{\partial \delta u}{\partial x_1}\left[C^*_{1111}\frac{\partial u}{\partial x_1} + C^*_{1113}\frac{\partial u}{\partial x_3} + C^*_{1131}\frac{\partial w}{\partial x_1} + C^*_{1133}\frac{\partial w}{\partial x_3}\right] + \right.\\ &\left. \frac{\partial \delta u}{\partial x_3}\left[C^*_{1311}\frac{\partial u}{\partial x_1} + C^*_{1313}\frac{\partial u}{\partial x_3} + C^*_{1331}\frac{\partial w}{\partial x_1} + C^*_{1333}\frac{\partial w}{\partial x_3}\right] + \delta u \rho \frac{\partial^2 u}{\partial t^2}\right\} dx_1 dx_3 - \int_\Gamma (\delta u t_x n) dS = 0\end{aligned} \tag{2.15}$$

$$\begin{aligned}&\int_\Omega \left\{ \frac{\partial \delta w}{\partial x_1}\left[C^*_{3111}\frac{\partial u}{\partial x_1} + C^*_{3113}\frac{\partial u}{\partial x_3} + C^*_{3131}\frac{\partial w}{\partial x_1} + C^*_{3133}\frac{\partial w}{\partial x_3}\right] + \right.\\ &\left. \frac{\partial \delta u}{\partial x_3}\left[C^*_{3311}\frac{\partial u}{\partial x_1} + C^*_{3313}\frac{\partial u}{\partial x_3} + C^*_{3331}\frac{\partial w}{\partial x_1} + C^*_{3333}\frac{\partial w}{\partial x_3}\right] + \delta w \rho \frac{\partial^2 w}{\partial t^2}\right\} dx_1 dx_3 - \int_\Gamma (\delta w t_z n) dS = 0\end{aligned} \tag{2.16}$$

Equations (2.15) and (2.16) represent the weak formulation of the equation of motion in the x_1 and x_3 directions. Finite element approximations are sought for displacement u and w assuming that the dependence of displacement on time is separated from the dependence on x_1 and x_3 directions. The approximations take the form,

$$u(x_1, x_3, t) = \sum_{j=1}^{n} U_j(t)\Gamma_j^u(x_1, x_3)$$

$$w(x_1, x_3, t) = \sum_{j=1}^{n} W_j(t)\Gamma_j^w(x_1, x_3) \tag{2.17}$$

Where, Γ_j represents the shape functions, which are continuous in the sub-domain of the problem over an element. The selection of the shape functions [54] or interpolation functions are made in such a way that the displacements are continuous across the boundary of each element of the finite element mesh and other conditions demanded by the variational form. The coefficients of the approximating functions are the nodal displacement values in each element node. Substituting these approximations in to the weak form equations (2.15) and (2.16) and the collection of coefficients of variations of displacements and placing them in matrix form will give the following matrix equations.

$$\begin{bmatrix} [M^{uu}][0] \\ [0][M^{ww}] \end{bmatrix} \begin{Bmatrix} \{\ddot{u}\} \\ \{\ddot{w}\} \end{Bmatrix} + \begin{bmatrix} [K^{uu}][K^{uw}] \\ [K^{wu}][K^{ww}] \end{bmatrix} \begin{Bmatrix} \{u\} \\ \{w\} \end{Bmatrix} = \begin{Bmatrix} \{f^u\} \\ \{f^w\} \end{Bmatrix} \tag{2.18}$$

Where M is the mass matrix, K is the stiffness matrix, f is the force vector and u and w are the displacements in the x_1 and x_3 directions. Each sub matrix in equation (2.18) is defined as follows

$$M_{ij}^{uu} = \int_{\Omega} [\rho \Gamma_i^u \Gamma_j^u] dx_1 dx_3 \tag{2.19}$$

$$M_{ij}^{ww} = \int_{\Omega} [\rho \Gamma_i^w \Gamma_j^w] dx_1 dx_3 \tag{2.20}$$

$$K_{ij}^{uu} = \iint_{\Omega} \left(C^*_{1111} \frac{\partial \Gamma_i}{\partial x_1} \frac{\partial \Gamma_j}{\partial x_1} + C^*_{1113} \frac{\partial \Gamma_i}{\partial x_1} \frac{\partial \Gamma_j}{\partial x_3} + C^*_{1311} \frac{\partial \Gamma_i}{\partial x_3} \frac{\partial \Gamma_j}{\partial x_1} + C^*_{1313} \frac{\partial \Gamma_i}{\partial x_3} \frac{\partial \Gamma_j}{\partial x_3} \right) dx_1 dx_3 \tag{2.21}$$

$$K_{ij}^{uw} = \iint_{\Omega} \left(C^*_{1131} \frac{\partial \Gamma_i}{\partial x_1} \frac{\partial \Gamma_j}{\partial x_1} + C^*_{1133} \frac{\partial \Gamma_i}{\partial x_1} \frac{\partial \Gamma_j}{\partial x_3} + C^*_{1331} \frac{\partial \Gamma_i}{\partial x_3} \frac{\partial \Gamma_j}{\partial x_1} + C^*_{1333} \frac{\partial \Gamma_i}{\partial x_3} \frac{\partial \Gamma_j}{\partial x_3} \right) dx_1 dx_3 \tag{2.22}$$

$$K_{ij}^{wu} = \iint_{\Omega} \left(C^*_{3111} \frac{\partial \Gamma_i}{\partial x_1} \frac{\partial \Gamma_j}{\partial x_1} + C^*_{3113} \frac{\partial \Gamma_i}{\partial x_1} \frac{\partial \Gamma_j}{\partial x_3} + C^*_{3311} \frac{\partial \Gamma_i}{\partial x_3} \frac{\partial \Gamma_j}{\partial x_1} + C^*_{3313} \frac{\partial \Gamma_i}{\partial x_3} \frac{\partial \Gamma_j}{\partial x_3} \right) dx_1 dx_3 \tag{2.23}$$

$$K_{ij}^{ww} = \iint_{\Omega} \left(C^*_{3131} \frac{\partial \Gamma_i}{\partial x_1} \frac{\partial \Gamma_j}{\partial x_1} + C^*_{3133} \frac{\partial \Gamma_i}{\partial x_1} \frac{\partial \Gamma_j}{\partial x_3} + C^*_{3331} \frac{\partial \Gamma_i}{\partial x_3} \frac{\partial \Gamma_j}{\partial x_1} + C^*_{3333} \frac{\partial \Gamma_i}{\partial x_3} \frac{\partial \Gamma_j}{\partial x_3} \right) dx_1 dx_3 \tag{2.24}$$

Since the C^*_{ijkl} tensor is unsymmetric due to the applied stress it makes the stiffness matrix K unsymmertic also. Thus the finite element equations derived in this section differs from conventional finite element equations of motion where the stiffness matrix K is symmetric.

2.3.2.1 Integration in Time

The Newmark’s constant average-acceleration method is used to compute the displacements for each time step. This is an extremely well-known method, can be found in several references [55]. It is sufficient to state that the generic velocity component $\dot{U}$ and displacement component U for time t + Δ t are assumed to possess the forms

$$\dot{U}^{t+\Delta t} = \dot{U}^{t} + [(1-\delta)\ddot{U}^{t} + \delta\ddot{U}^{t+\Delta t}]\Delta t \qquad (2.25)$$

$$U^{t+\Delta t} = U^{t} + \dot{U}^{t}\Delta t + [\left(\frac{1}{2} - \alpha\right)\ddot{U}^{t} + \alpha\ddot{U}^{t+\Delta t}]\Delta t^{2} \qquad (2.26)$$

The selection of constants δ = 0.5 and α = 0.25 provides unconditional stability to the problem. The equilibrium equation at time t + Δ t can be written as

$$M\ddot{U}^{t+\Delta t} + C\dot{U}^{t+\Delta t} + KU^{t+\Delta t} = R^{t+\Delta t} \qquad (2.27)$$

Here M is mass matrix, C damping matrix, K the stiffness matrix, $\ddot{U}$ the acceleration vector, $\dot{U}$ the velocity vector, U the displacement vector, and R is the load vector for time t + Δ t. From Equations (2.25 and 2.26), the accelerations and velocity can be written in terms of unknown displacements alone. This relation is then substituted into (2.27) to compute the displacements. The initial acceleration vector is evaluated using the initial conditions, and the analysis proceeds in stepwise fashion as each of the fields is updated at the end of the specified time step. Detailed algorithm is given below.

Step 1 initial calculation.

1. Form the stiffness matrix K, mass matrix M and damping matrix C (C=0, in all simulations done in this research).

2. Initialize (displacements, velocity and acceleration).

3. Select time step size Δt, parameters δ andα. Calculate integration constants:

$$\alpha \geq 0.25(0.5+\delta)^2 \quad , \qquad \delta \geq 0.5$$

$a_0=1/\Delta t^2$; $a_2=1/\alpha\ \Delta t$; $a_3=(1/2\alpha)-1$;

Other constants a_1, a_3, a_4, a_5, a_6, a_7 are not computed since damping is assumed to be zero.

4. The effective stiffness matrix is formed

$$\widehat{K} = K + a_o M$$

Step 2 computations for each time step.

1. Calculate effective loads at time t + Δt.

$$^{t+\Delta t}\widehat{R} = {}^{t+\Delta t}R + M(a_0 U^t + a_3 \ddot{U}^t)$$

2. Solving for the displacements at time t + Δt.

$$\widehat{K} U^{t+\Delta t} = \widehat{R}^{t+\Delta t}$$

3. Compute the accelerations at time t + Δt.

$$\ddot{U}^{t+\Delta t} = a_0(U^{t+\Delta t} - U^t) - a_3 \ddot{U}^t$$

Chapter 3

Nanoindentation of Thin Films: Thickness effects

3.1 Introduction

In this chapter, effects of film thickness on indentation response, both in the elastic and the plastic regimes of single crystal films of varying thicknesses are studied. The deformation mechanism in the plastic regime was also analyzed. The Ni films are oriented in the [111] direction. The elastic responses of the films are compared with Hertzian theory. The technique for the simulation is classical molecular dynamics. The goal of the investigation is to elucidate the effects of film thickness on the elastic and plastic behavior.

3.2 Simulation Setup

In order to study the thickness effects due to indentation, samples of single crystal films were generated for different thickness. We generated samples of 7nm and 33nm by changing the dimension of the film along [111] direction (Figure 3.1). The dimensions of 52nm along the $[1\bar{1}0]$ direction and 52nm along the $[11\bar{2}]$ direction were chosen so that the sample is significantly larger than the indentation contact area at maximum depth (10nm) and the spurious effects originating from the finite size of the sample in these directions can be avoided. Before the indentation process, all the samples were relaxed for 100 ps at 300 K using molecular dynamics as implemented in the LAMMPS code [42]. This relaxation was performed with free surface boundary conditions for the top of the film and a fixed layer of atoms to represent the substrate. The boundary conditions in the directions contained in the film are periodic.

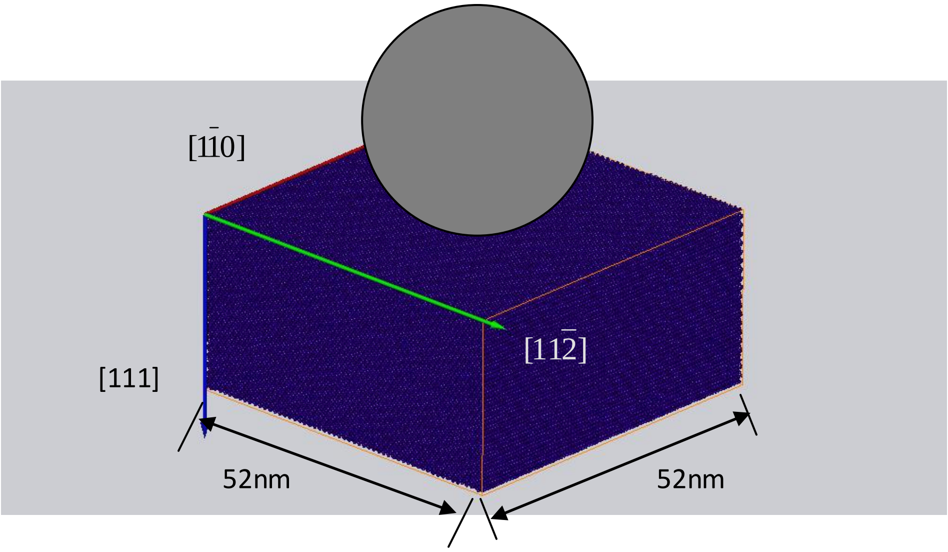

Figure 3.1: Orientation and size of the single crystal films used in the indentation simulations.

The embedded atom method is currently a common technique used in molecular dynamics computer simulation of metallic systems [43]. The method provides a good description of the interatomic forces in the system, particularly for FCC metals as discussed in chapter 2. The Ni potential functions developed by Voter and Chen [57] has been used. These potentials reproduce the perfect lattice properties well and have been tested extensively.

The molecular dynamics algorithm is used here as implemented in the LAMMPS code by Plimpton [42]. The boundary conditions used are periodic in the directions that are perpendicular to the indentation force. In the direction of the indentation force we used a free surface boundary condition for the top of the film and a fixed boundary condition for the bottom of the film, representing a hard substrate. For the indenter, we use a totally rigid spherical indenter of radius 15 nm with a force on each atom given by equation (2.1)

The indention process was started by lowering the indenter down the [111] direction into the two thin films at the rate of 1nm per 100 ps. This rate is much faster than in experiments, and is a result of the limitations of the molecular dynamics technique, even using massively parallel simulations, as done here. The simulation was performed at 300^{o} K with the bottom three atomic layers fixed in the [111] direction. The top of the film surface was treated as a free surface. Periodic boundary conditions were imposed in the $[1\bar{1}0]$ and $[11\bar{2}]$ directions. The atomic positions are monitored at 10 ps intervals until the indentation process is completed after the tip reaches a maximum depth. Contact stresses are obtained as force divided by contact area with the contact area (equation 2.3) between the indenter and the film.

In order to selectively visualize interior defects, we have employed a visualization technique based on the centrosymmetry parameter that was proven effective for the studies of dislocation emission in FCC crystals and is described by Kelchner et al. [58]. Centrosymmetry parameter values between 3 and 20 are typical of dislocation cores and stacking faults. Values of centrosymmetry parameter larger than 20 (red color) correspond to atoms at the surface. The atoms with centrosymmetry parameter lower than 3 are located near perfect lattice positions and are not displayed for visualization purposes.

3.3 Results and Discussion

3.3.1 Effect of film thickness in the elastic regime

Forces versus indenter displacement results in the elastic regime are plotted for the films of two different thicknesses in Figure 3.2. The Hertzian theory [59] prediction for a semi-infinite film indented by a spherical indenter is also shown for comparison. The force in Hertzian theory is given by:

$$P = (4/3)\, E\, R^{1/2}\, h^{3/2} \qquad (4.1)$$

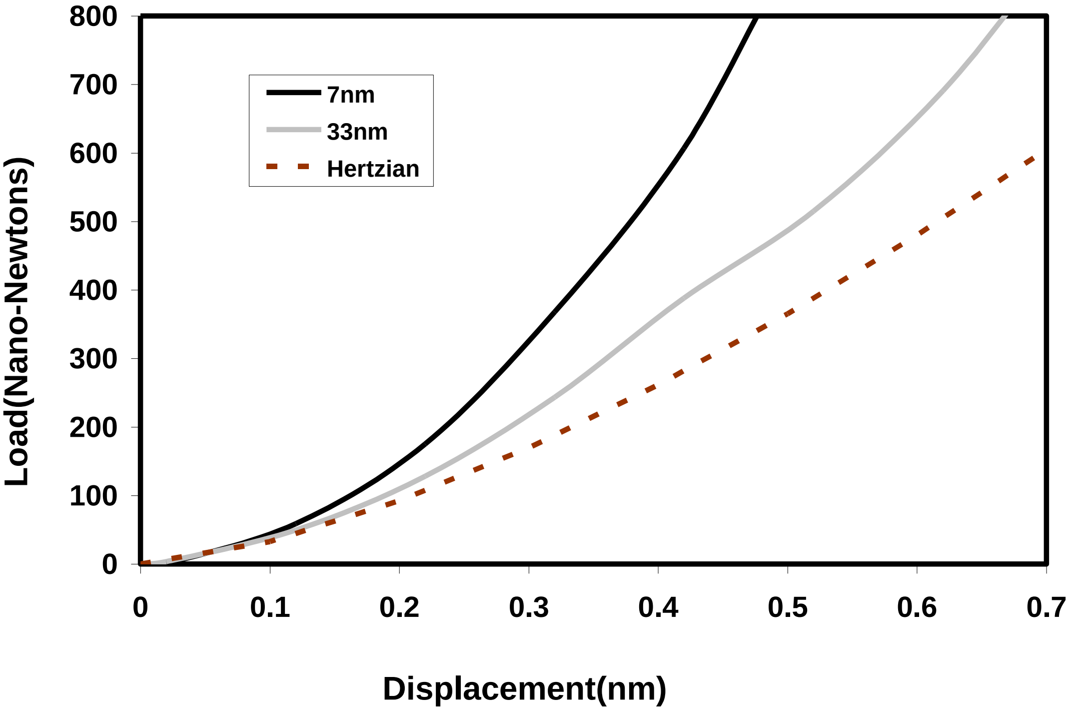

Figure 3.2: Force versus indenter displacements curves obtained in the elastic regime for films of 7nm and 33nm thicknesses. The Hertzian theory predictions for a semi-infinite film are shown for comparison along 7nm and 33nm films thicknesses.

Where E is the modulus of elasticity of Ni (220 Gpa), R radius of the indenter of 15 nm and h is the indentation depth. These results show that indentation into these thin films only follow the Hertzian predictions for a semi-infinite crystal in the very initial stages of the indentation. These results show that in the elastic region, the thinner films require higher forces to achieve the same indentation depth than the thicker films. As expected, the deviation from the Hertzian theory is larger for the thinner films.

3.3.2 Effect of film thickness on the initial plastic event

Figure 3.3a shows the forces for which the first dislocation is emitted under the indenter, constituting the initial plastic event. The force values depend on film thicknesses, with the first dislocation appearing at lower indentation depths and requiring higher forces for the thinner films.

In order to find the stress required to emit the first dislocation and to observe the effect of thickness in single crystal films, the contact pressure under the indenter on the film surface was plotted against the indentation depth for different values of film thickness, as shown in Figure 3. 3b. The contact pressure was calculated from the force of the indenter and the contact areas directly observed in the sample. As the film thickness increases, the first dislocation appears at larger indentation depths. However, the contact pressure necessary for the initiation of plasticity in these single crystal films is mostly independent of the film thickness. This implies that the contact stress required for the emission of the first dislocation is not significantly dependent on the film thickness, and independent of the different elastic deformation and stress fields created by the indentation of films of various thicknesses. The contact pressure under the indenter necessary for the homogenous nucleation of the first dislocation is a material dependent quantity and is not affected by film thickness. The thickness independent contact pressure for our [111] single crystal film is approximately 16 GPa. Hardnesses of 5 to 6 GPa were experimentally observed in the nanoindentation of Ni films with the (100) orientation [18] at a depth between 0.01μm and 0.1μm. Pan et al[60] report experimental values of 6 to 7 GPa for nanocrystalline Ni. One important reason why the value obtained in the simulations is higher is the fact that the experiments are performed on films that contain grain boundaries and other defects, providing sites for heterogeneous nucleation of dislocations.

It is shown in the current study that the critical stress needed to initiate plasticity in single crystals through homogeneous nucleation of dislocations is independent of the film thickness. Several experimental studies ([61], [62], [63]) have shown that the onset of plasticity in micro and nano pillars is size-dependent. This suggests that in these experiments heterogeneous nucleation of dislocations is responsible for the onset of plasticity.

Another reason why the hardness obtained in the simulations can be higher than the experimental values is that hardness increases with decreasing penetration depth. Zong et al[18] have reported that this phenomenon is significant in the nanoscale and the hardness increases by a factor of 2 when depth decreases from 500 to 30nm. In addition, Zhang et al. [34] and Qu et al. [37] found similar effects at the micron to sub-micron scale.

Hence the value of 16 GPa for the initial plastic event is reasonable for the hardness of Ni thin films at the nanoscale, considering our indentation depths are less than 10 nm.

3.3.3 The plastic region

Figure 3.4 shows the full results for the indentation process well into the plastic region. Figure 3.4a shows the results in terms of the loading curves and figure 3.4b shows the contact pressure curves. The results indicate that the thinner films are harder in the plastic regime, due to the effects of the substrate. In order to understand the reasons for this behavior, in the following section we analyze the deformation mechanism in detail.

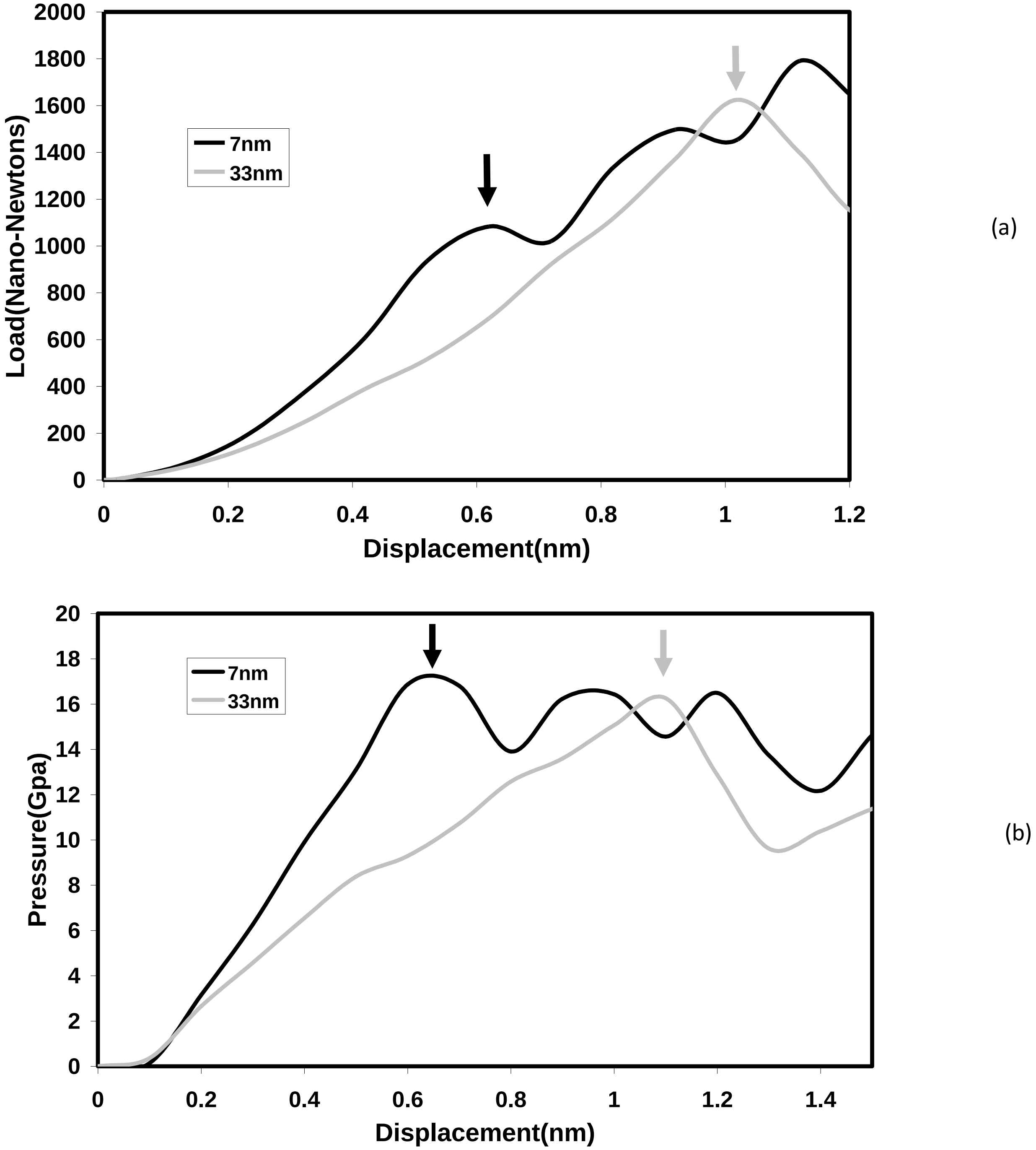

Figure 3.3: The initial plastic event indicated by the arrows for films of both thicknesses. (a) Force versus indenter displacements curves. (b) Contact pressure (GPa) vs. indenter displacement curves.

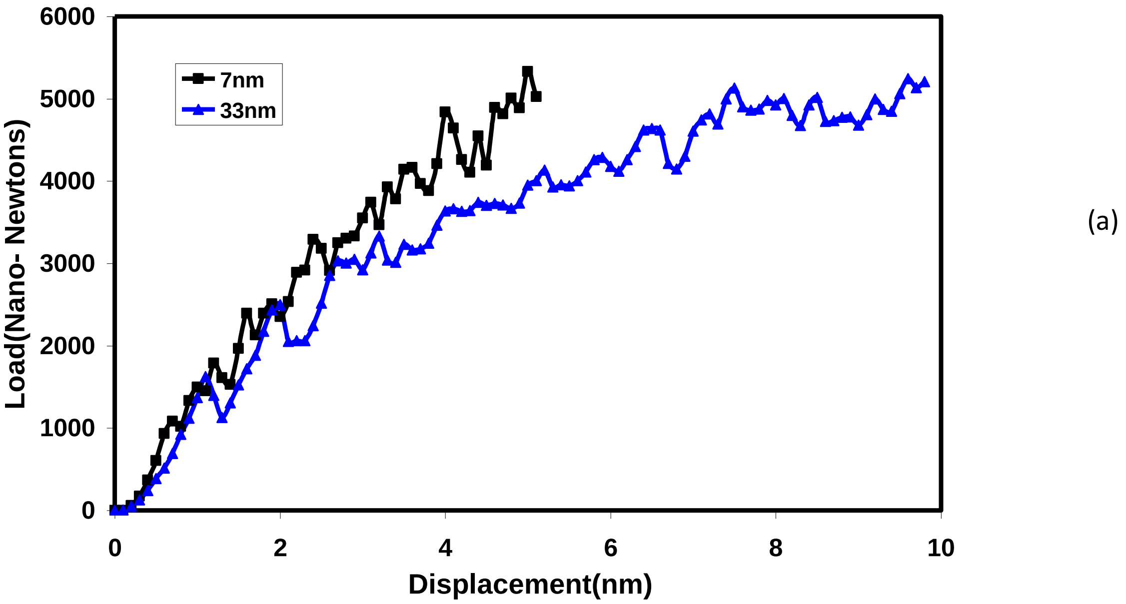

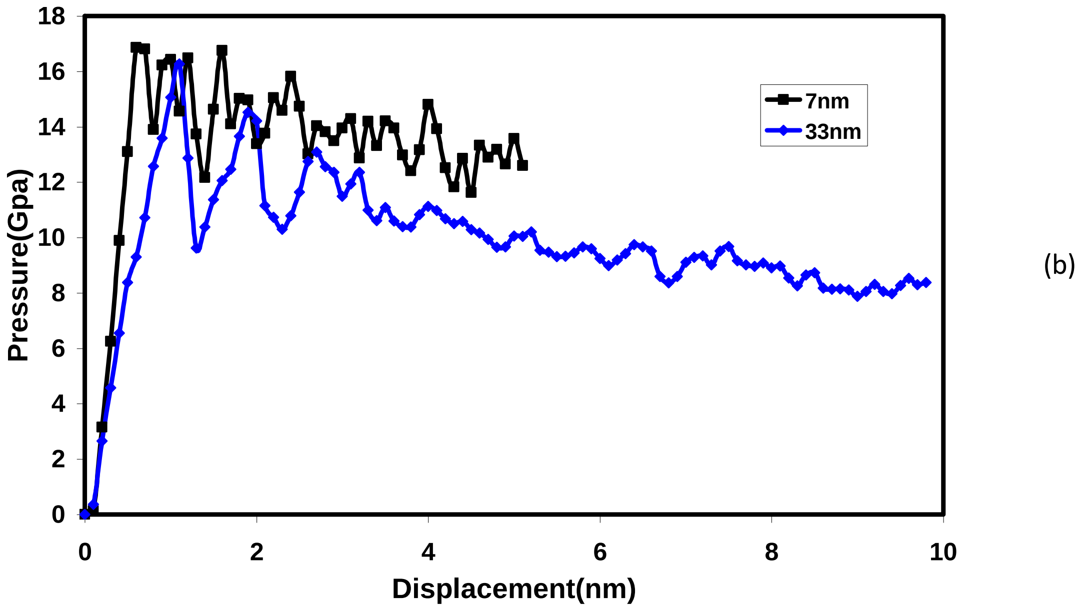

Figure 3.4: Loading (a) and Contact pressure (b) vs. indenter displacement curves for films of 7nm and 33nm in the plastic regime.

3.3.4 Deformation Mechanism in Nanoindentation

The atomistic visualization of the indentation simulations showed the mechanisms responsible for the plastic deformation in these films. In the initial phase of plastic behavior, homogenous nucleation of the dislocations are observed directly under the indenter and as the force of the indenter increases dislocation loops are formed (Figure 3.5). This phenomenon is consistent with the studies done by Li et al. [20] and Lee et al. [24] where they observed the incipient plasticity is initiated by the homogenously nucleated glide loops. These dislocation loops then start to grow and expand inside the film and forming prismatic partial glide loops. Figure 3.5 shows dislocation loops that were observed after the initial dislocation burst for the 33 nm sample at various indentation depths. Figure 3.6 shows in detail one such prismatic loop, where each side of the loop consists of stacking-fault and are bounded by Shockley partials. The prismatic partial loops glide down to the hard substrate as the indentation depth increases and cannot penetrate the substrate. It gets reflected back as shown in Figure 3.5. This phenomenon was not observed by Lee et al. [24] for Al since the bottom surface was imposed as a free boundary condition; hence the loop passed through the substrate leaving an impression of a parallelogram. Our simulation also indicates that loops are emitted not only in one direction but in multiple directions (Figure 3.5 c&d). As the film thickness decreases, loops cannot move as easily due to the fact that there is less space available. In order to understand the effects of this constraint on the plastic deformation process, we analyzed quantitatively the number of dislocations emitted by counting the atoms that have centrosymmetry parameters between 3 and 10 and are located in the dislocations. This number of atoms should be a good quantitative indication of the dislocation activity as indentation progresses. Figure 3.7 shows the number of atoms in the dislocations as a function of depth for both films. These results show that film thickness has a significant effect on the number of dislocation emitted. This explains the increased hardness observed for the thinner films.

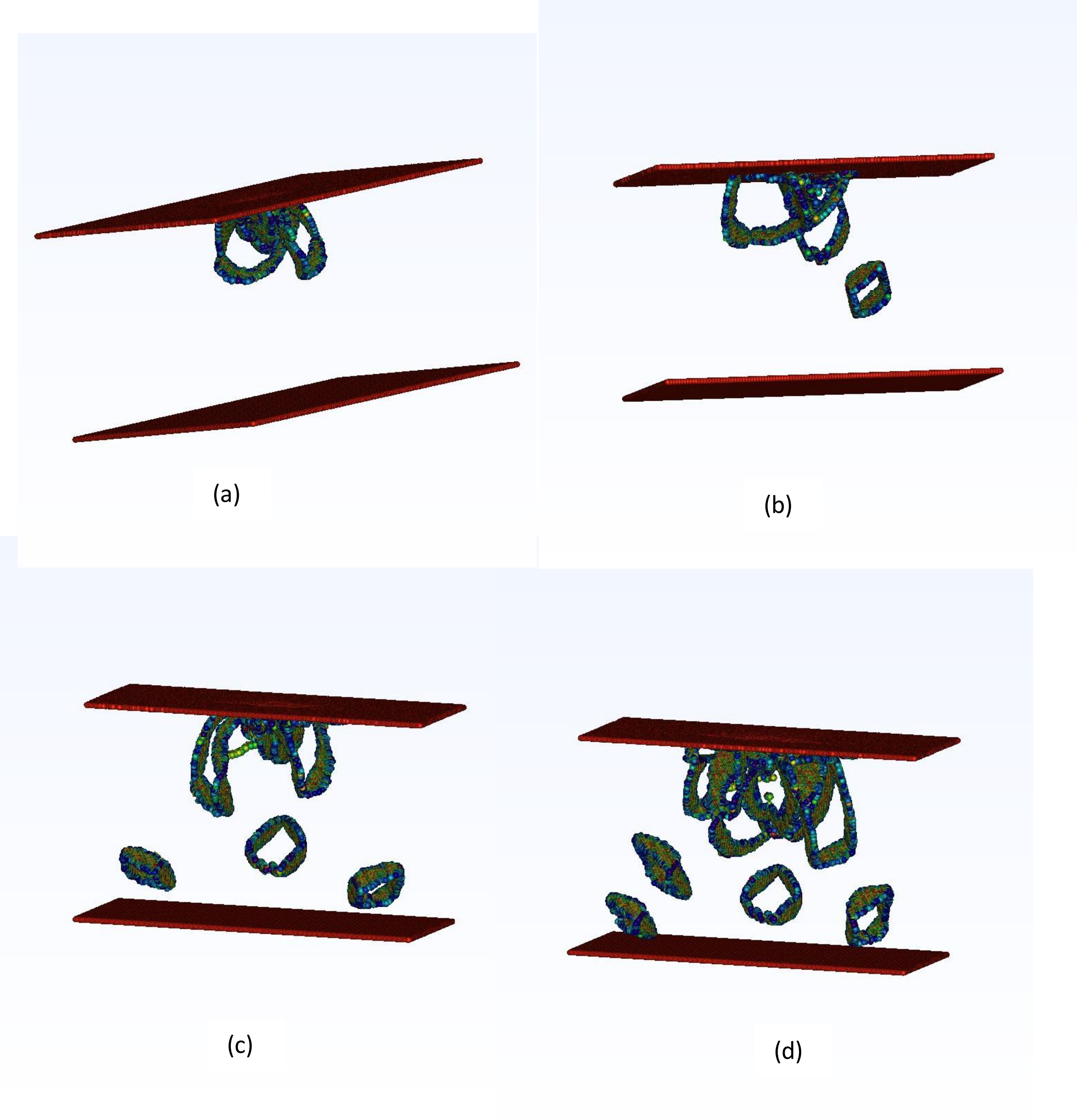

Figure 3.5: Visulaization of the dislocation emission process in the 33 nm film due to indentation at depths of (a) 1.2nm (b) 1.4 nm (c) 1.6 nm (d) 2 nm. Red atoms indicate free surface boundary condition for the top of the film and a fixed substrate for the bottom of the film. Each side of the loop consists of stacking-fault and is bounded by Shockley partials (blue colored atoms). (Movie_1)

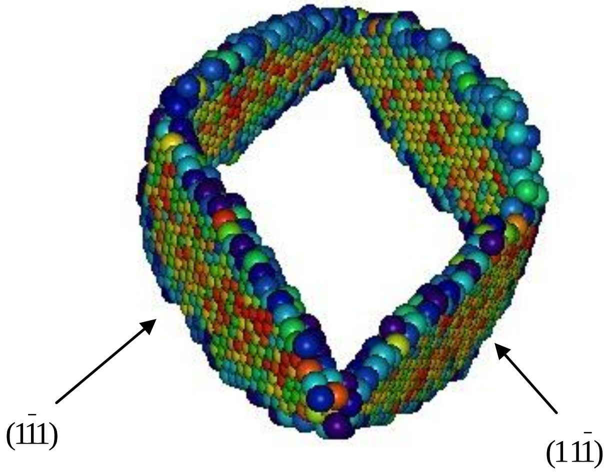

Figure 3.6: Enhanced view of one of the emitted dislocation loops.

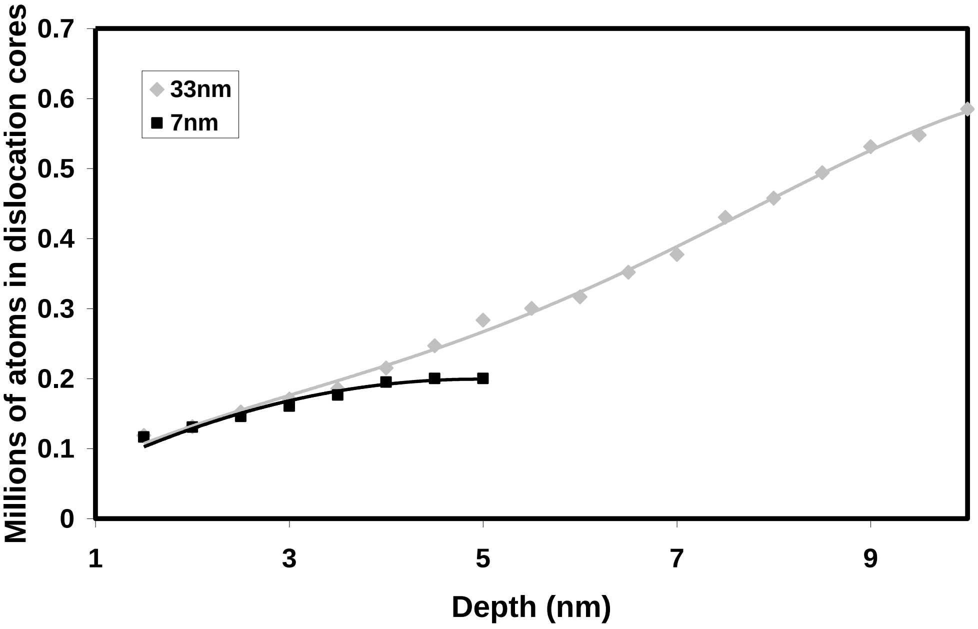

Figure 3.7: Number of atoms contained in the dislocations emitted for films of 7nm and 33nm versus depth of indentation.

Chapter 4

Nanoindentation of Thin Films with Low Angle Grain Boundaries

4.1 Introduction

In this chapter the thickness effects of single crystal films as well as films containing grain boundaries are studied. The indentation is carried out for smaller depths to study the elastic and initial plasticity effects. The simulation procedure is explained and results are discussed at the end of the chapter.

4.2 Simulation Setup

In order to study the thickness effects due to indentation, samples of single crystal films and films containing pre-existing low angle boundaries were generated for different thickness. Samples of 4nm, 6nm, 8nm and 12.8nm were generated by changing the dimension of the film along [111] direction (Figure 4.1(a), 4.1(b)). The dimensions of 25nm along the $[1\bar{1}0]$ direction and 25nm along the $[11\bar{2}]$ direction were chosen so that the sample is significantly larger than the indentation contact area at maximum depth (2.5nm) and the spurious effects originating from the finite size of the sample in these directions can be avoided.

For each film thickness a single crystal sample and two additional samples were generated. These two samples, labeled sample 1 and sample 2 contained three grains each of two different low angle grain boundary configurations. They were created for each thicknesses using the Voronoi grain growth method [11-13] and random orientations, not to exceed 10 degrees. The low angle grain boundaries were pure tilt in character located all parallel to the [111] direction, and were characterized by exactly the same parameters for all film thicknesses. Because they were pure tilt the indentation direction coincided with [111] in all grains and all samples. All the samples were relaxed for 100 ps at 300 K using molecular dynamics as implemented in the LAMMPS code [42]. Figure 4.1(a) shows the orientation of the film for the single crystal and Figure 4.1(b) shows the structure and orientation of the relaxed samples that contained low angle boundaries used for indentation (sample 1). Sample 2 was characterized by low grain boundary parameters different from sample 1, but again maintained the same for all film thicknesses. The film surfaces were always oriented normal to the [111] direction and all low angle boundaries were pure tilt boundaries perpendicular to the film surface.

The main difference between the parameters of the grain boundaries in samples 1 and 2 is the misorientation angles. Figure 4.1(c & d) shows the difference in grain boundary structure for the grain boundary in the center of the simulation block for sample 1 and sample 2. For sample 1, the misorientation angle is about 5 degrees and the dislocations cores that make up this low angle boundary are non-overlapping. For sample 2 the misorientation is 10 degrees and the dislocations cores that make up this low angle boundary are very near each other.

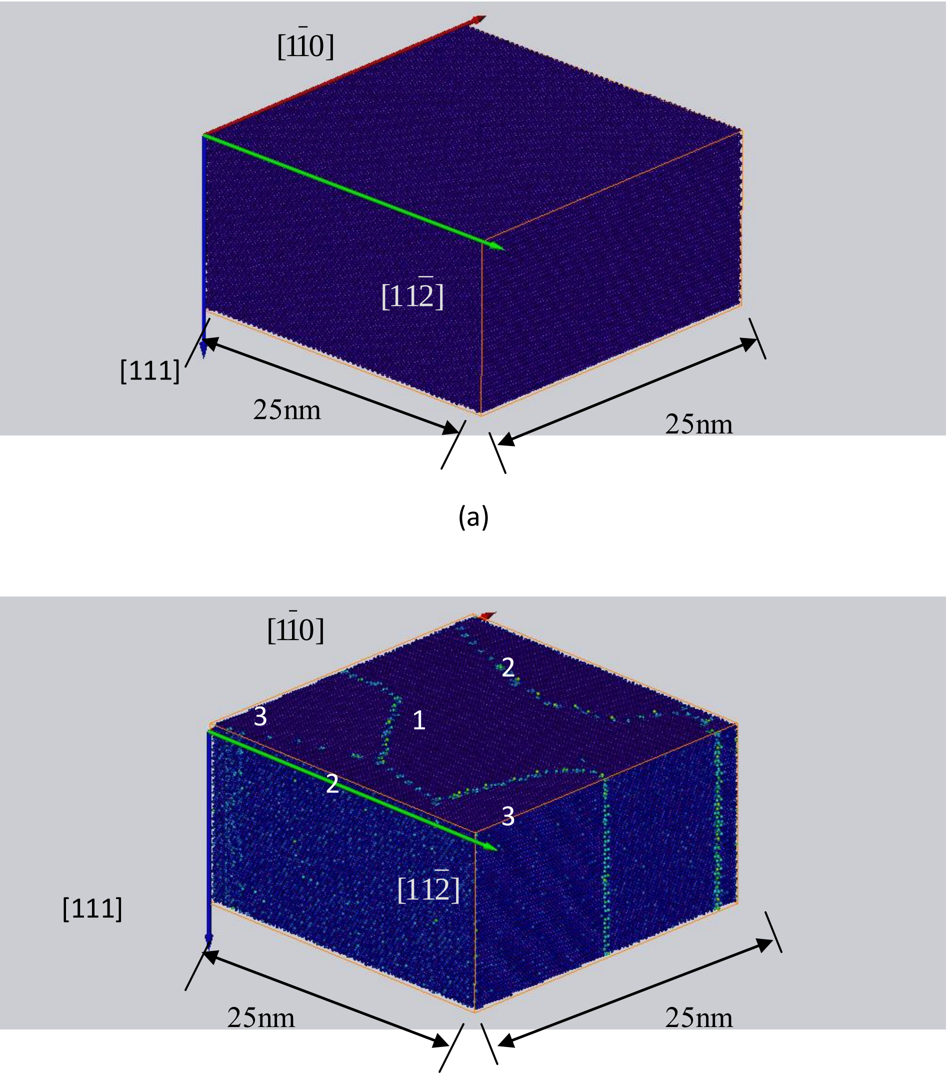

(a)

(b)

Figure 4.1: a) Orientation and size of the single crystal film used in the indentation simulations and b) Orientation and size of the sample containing low angle boundaries used in the indentation simulations. The sample contains three grains as indicated. c) Detailed view of the center of sample 1 showing the grain boundary structure. d) Detailed view of the center of sample 2 showing the grain boundary structure.

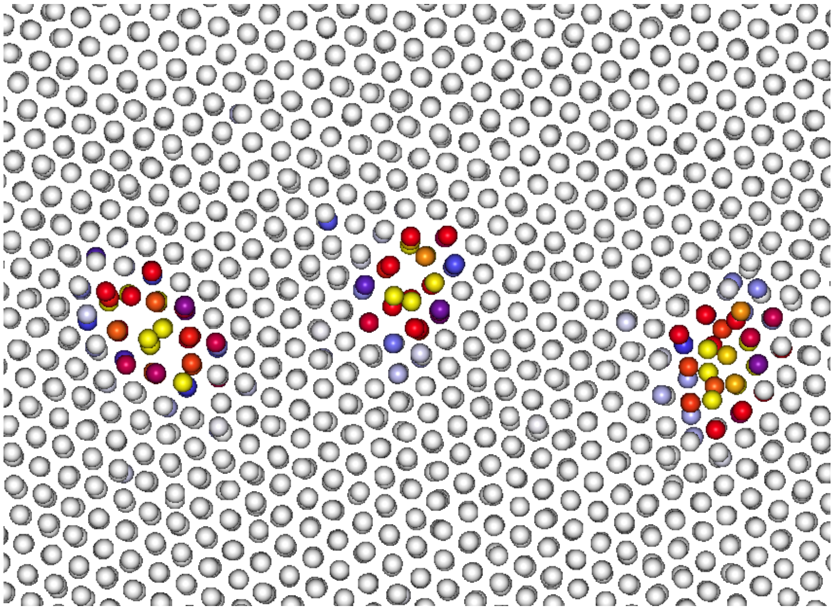

(c)

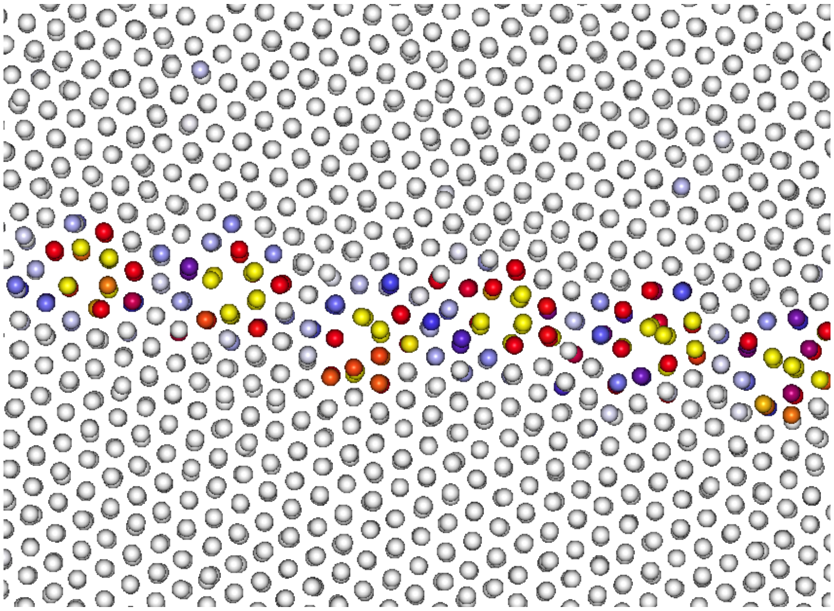

(d)

4.3 Indentation and Visualization of Results

The simulations were performed using the LAMMPS code [42] in which a rigid spherical indenter with a radius of 30 nm was chosen. The indention process was started by lowering the indenter down the [111] direction into the various thin films at the rate of 1nm per 100 ps. This rate is much faster than in experiments, and is a result of the limitations of the molecular dynamics technique, even using massively parallel simulations, as done here. The simulation was performed at 300 K with the bottom three atomic layers fixed in the [111] direction. The top of the film surface was treated as a free surface. Periodic boundary conditions were imposed in the $[1\bar{1}0]$ and $[11\bar{2}]$ directions. The atomic positions are monitored at 10 ps intervals until the indentation process is completed after the tip reaches a maximum depth, which was taken as 20% of the overall thickness for each sample. The force from the indenter is obtained using the atomic positions corresponding to each time step and the force given by equation (2.1). The contact area between the indenter and the film is subsequently used to obtain contact pressures. The contact area is computed using equation (2.2).

In order to selectively visualize interior defects, the visualization technique based on the centrosymmetry parameter was employed which was proven effective for the studies of dislocation emission in FCC crystals [58]. Centrosymmetry parameter values between 3 and 6 are typical of dislocation cores and stacking faults. A centrosymmetry parameter value larger than 20 indicate the atoms at the surface. The atoms with centrosymmetry parameter lower than

3 indicate atoms in the near perfect lattice positions and are not displayed for visualization purposes.

4.4 Results and Discussions

4.4.1 Effect of film thickness in single crystals

Force versus indenter displacement results are plotted for single crystal films of different thickness in Figure 4.2. Figure 4.2 shows that the elastic part of the load-displacement curves depends on the film thicknesses. Hertzian theory [59] prediction for a semi-infinite film indented by a spherical indenter is also shown for comparison. The force in Hertzian theory is given by:

$$P= (4/3)\, E\, R^{1/2}\, h^{3/2} \qquad (4.1)$$

Where E is the modulus of elasticity of Ni (220 Gpa), R radius of the indenter 30 nm and h is the indentation depth. These results show that indentation into these thin films only follow the Hertzian predictions for a semi-infinite crystal in the very initial stages of the indentation. For the 6 nm film the deviation starts at approximately 0.15 nm indentation depth. For the 8 nm film the deviation is observed at an indentation depth of 0.2 nm and for the 12 nm film agreement with equation 4 is maintained up to indentation depth of 0.3 nm. These values indicate that the effects of the hard substrate are felt elastically for indentations greater than 2.5% of the film thickness. After these values, even in the elastic region, the thinner films require higher forces to achieve the same indentation depth than the thicker films. Figure 4.2 also shows the forces and depths for which the first dislocation is emitted under the indenter. These values depend on film

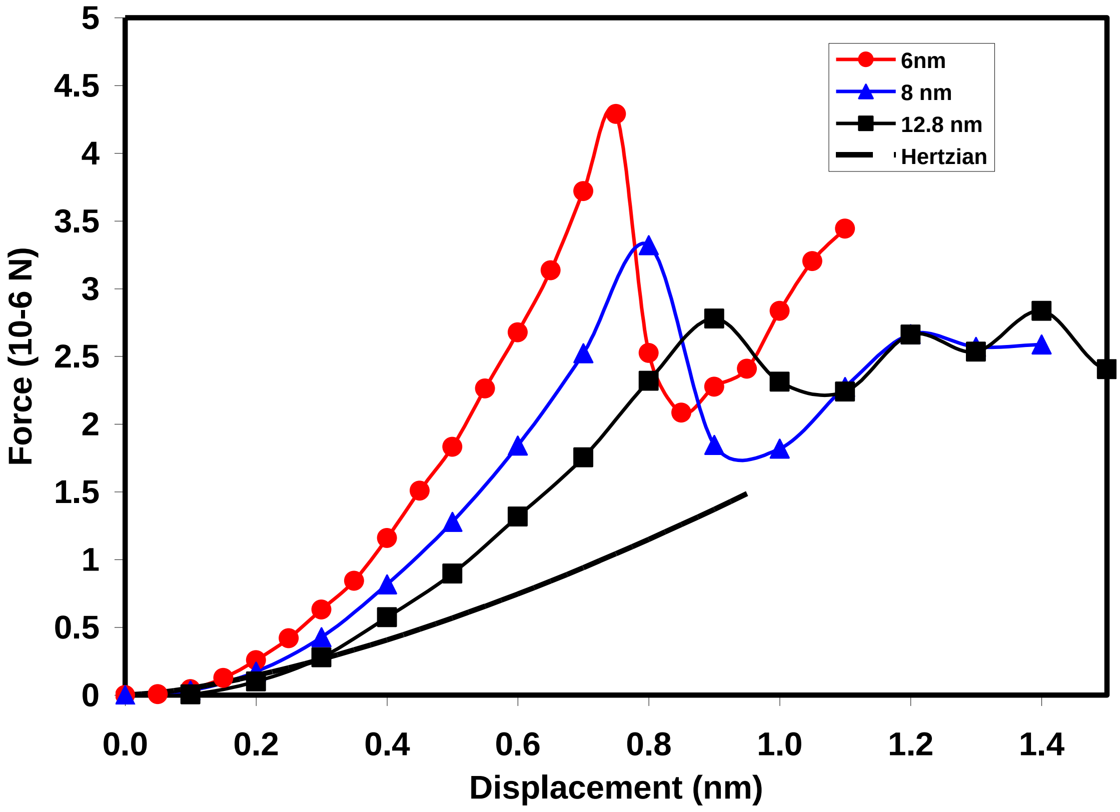

Figure 4.2: Force versus indenter displacements curves obtained for the single crystals films of various thicknesses. The Hertzian theory predictions for a semi-infinite film are shown for comparison.

thicknesses, with the first dislocation appearing at lower indentation depths and requiring higher forces for the thinner films. The atomistic visualization of the indentation simulations showed the mechanisms responsible for the plastic deformation in these films. In the initial phase of plastic behavior, homogenous nucleation of the dislocations are observed directly under the indenter and as the force of the indenter increases dislocation loops are formed. These dislocation loops then start to grow and expand inside the film. Figure 4.3 shows dislocation loops that were observed after the initial dislocation burst for the 6.0 nm and 12.8 nm samples. This phenomenon is consistent with the studies done by Li et al. [20] and Lee et al. [24] where they observed the incipient plasticity is initiated by the homogenously nucleated glide loops. Differences in the loops configurations are observed in the plastic part of the indentation. As the film thickness decreases, loops cannot move as easily due to the fact that the space available for the dislocation loop is smaller. This impediment to the motion of dislocation loops leads to hardening of the material in the plastic region as the thickness decreases.

In order to find the stress required to emit the first dislocation and to observe the effect of thickness in single crystal films, the contact pressure under the indenter on the film surface was plotted against the indentation depth for different values of film thickness, as shown in Figure 4.4. The contact pressure was calculated from the force of the indenter and the contact areas directly observed in the sample. As the film thickness increases, the first dislocation appears at larger indentation depths. However, the contact pressure necessary for the initiation of plasticity in these single crystal films are mostly independent of the film thickness. This implies that the contact stress required for the emission of the first dislocation is not significantly dependent on the film thickness, and independent of the different elastic deformation and stress fields created by the indentation of films of various thicknesses. The contact pressure under the indenter necessary for the homogenous nucleation of the first dislocation is a material dependent quantity and is not affected by film thickness.

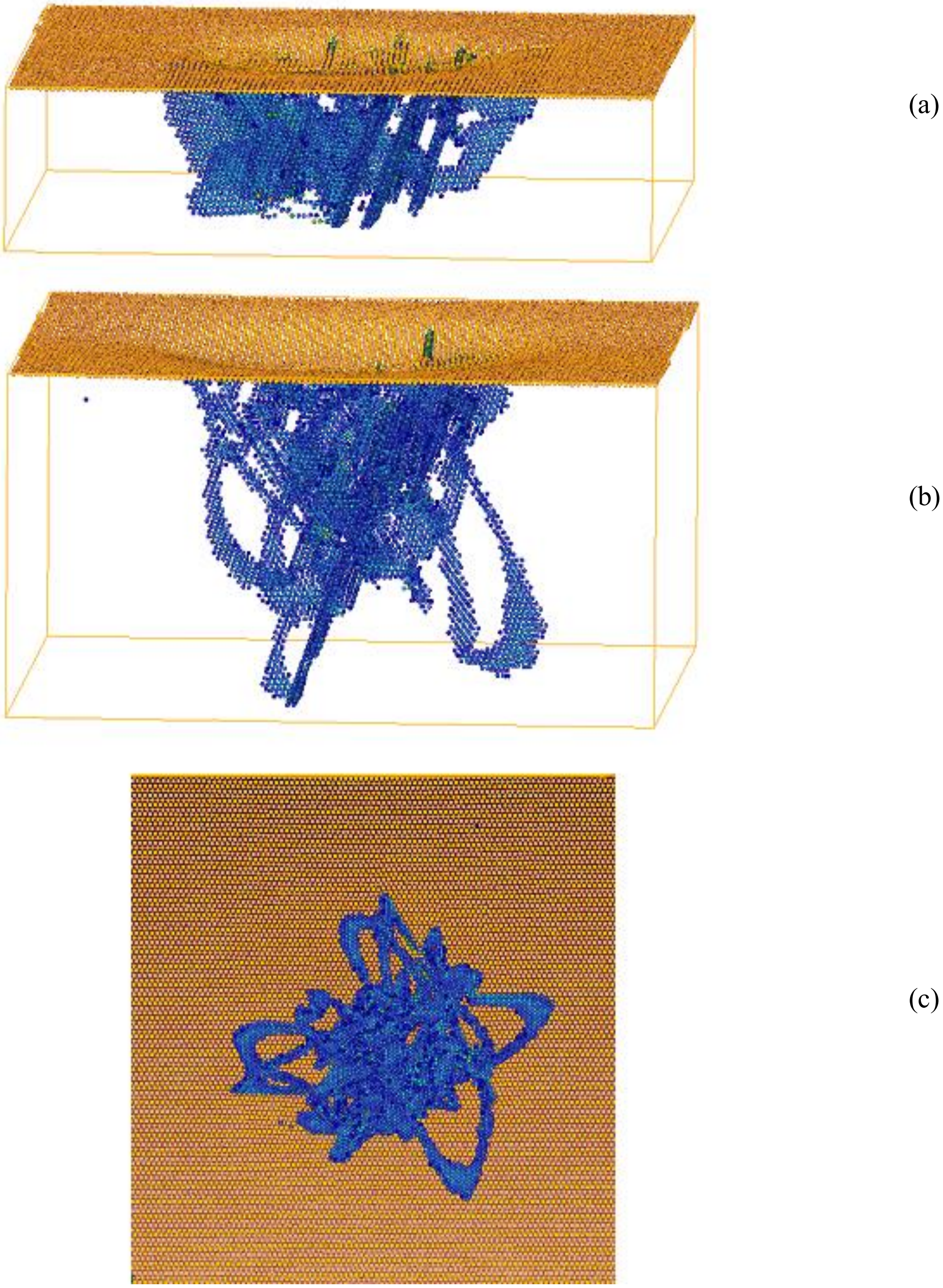

Figure 4.3: Dislocations emitted in the indented single crystal films after the first burst with indent depth of (a) 0.9 nm in 6 nm thick film and (b) at a depth of 1.5 nm in 12.8 nm thick film (c) Top view of the indented 12.8 nm film.

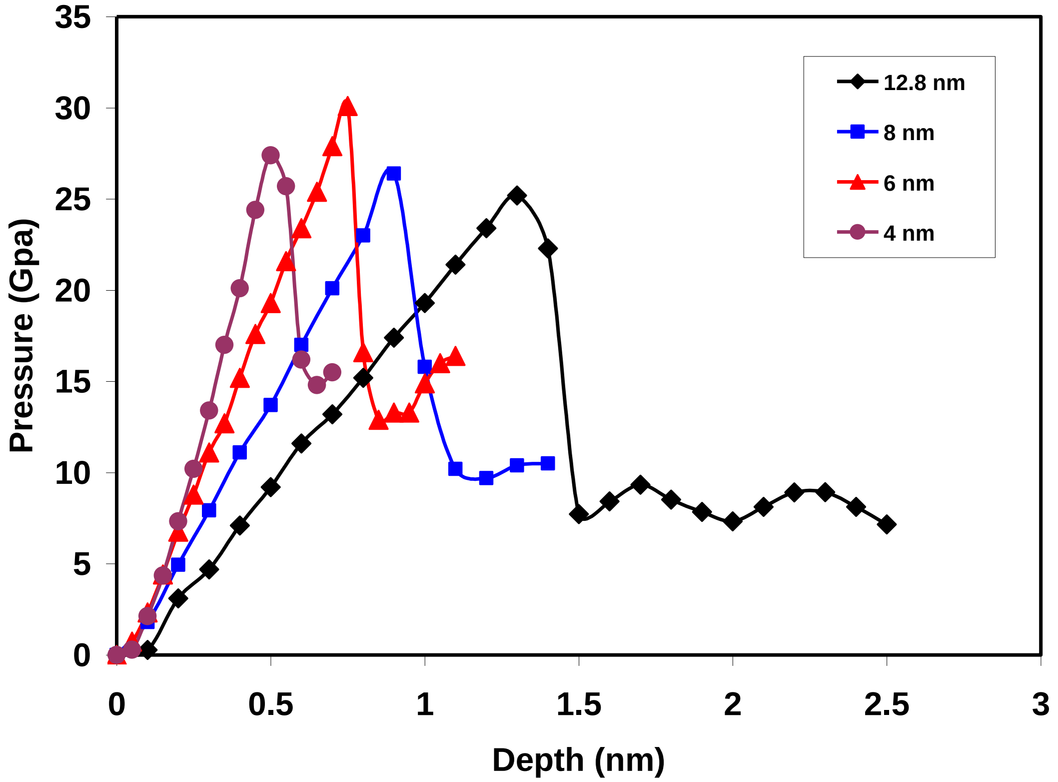

Figure 4.4: Contact pressure (GPa) vs. indenter displacement for single crystal films of varying sample thickness.

The thickness independent contact pressure for our [111] single crystal film is approximately 28 GPa. Hardnesses of 5 to 6 GPa were experimentally observed in the nanoindentation of Ni films with the (100) orientation [18] at a depth between 0.01µm and 0.1µm. Pan et al. [60] reported experimental values of 6 to 7 GPa for nanocrystalline Ni. One important reason why the value obtained in the simulations is higher is the fact that the experiments are performed on films that contain grain boundaries and other defects, providing sites for heterogeneous nucleation of dislocations. In chapter 3 the hardness value obtained is 16 Gpa using interatomic potential developed by Voter et al. [46].This clearly indicates that the interatomic potential used for simulations also affects the hardness value

It is shown in the current study that the critical stress needed to initiate plasticity in single crystals through homogeneous nucleation of dislocations is independent of the film thickness. It is the heterogeneous nucleation of dislocations that in our study presents size dependence. This is a very important conclusion, since several experimental studies [61-63] have shown that the onset of plasticity in micro and nano pillars is size-dependent. This suggests that in these experiments heterogeneous nucleation of dislocations is responsible for the onset of plasticity.

Another reason why the hardness obtained in the simulations can be higher than the experimental values is that hardness increases with decreasing penetration depth. Zong et al. [18] has reported that this phenomenon is significant in the nanoscale and the hardness increases by a factor of 2 when depth decreases from 500 to 30nm. In addition, Zhang et al. [34] and Qu et al. [37] found similar effects at the micron to sub-micron scale. Hence the value of 28 GPa is reasonable for the hardness of Ni thin films at the nanoscale, considering our indentation depths are less than 3 nm. Furthermore, the indenter shape and size have also been shown to have an effect on the observed hardness [36, 64].

4.4.2 Effect of low angle grain boundaries (LAGB’s)

In the samples containing low angle grain boundaries (LAGB’s), the expectation is that these defects will constitute preferred sites for first dislocation emission. This was indeed observed in our simulations and an example is shown in Figure 4.5. In most cases the dislocations were first emitted from these preexisting defects. However, we observed an important size effect in the role of the low angle grain boundaries. Our results indicate that in the thinner defective films there were dislocations emitted in areas of the film with no defects. For these very thin films (4 nm) the grain boundaries were not effective emission sites for the dislocations. For the relatively thicker films the dislocations were clearly emitted from the grain boundaries. This is in contrast to the behavior observed in the single crystal where the first dislocation is always emitted from directly underneath the indenter. The observed size effect indicates that the emission of dislocations from these low angle grain boundaries is easier as the film thickness increases. Sample dimensions have been shown to affect crystal plasticity and strength [61, 65].

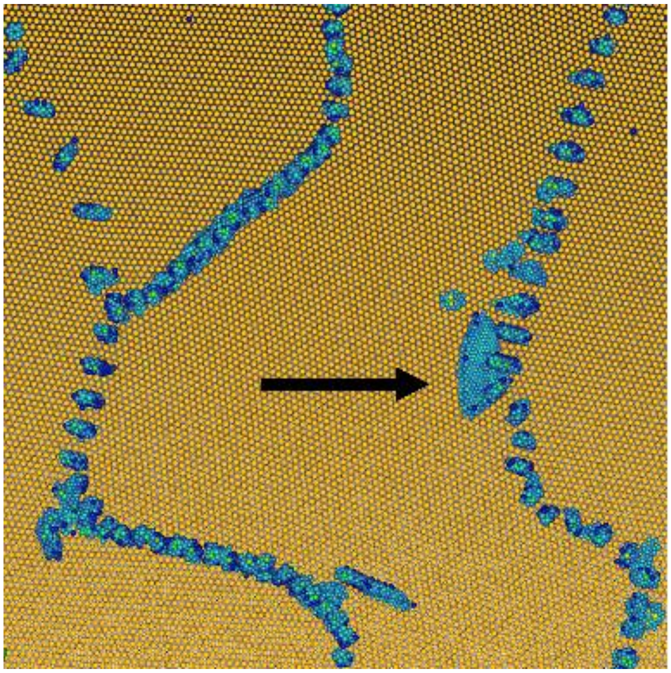

Figure 4.5: Front view of the first dislocation emitted in the film of 12.8 nm thickness containing low angle boundaries. The dislocations are emitted from the boundary area.

In order to find the stress required in emitting the first dislocation and the effect of thickness in the samples containing the low angle grain boundaries, contact pressure of the indenter with film surface is plotted against the indenter depth for all thicknesses for single crystals as well as films containing grain boundaries referred here as sample 1 and sample 2 (Figure 4.6). These results indicate that the films containing the low angle boundaries present an elastic response (slope of pressure curve) that is higher for films at low thicknesses. This behavior is similar to that of the single crystal films. As the thickness of the film increases, another trend is apparent, namely that as film thickness increases, as in figures 4.6a to 4.6d, the effect of preexisting grain boundaries is stronger. In very thin films, the difference between the responses of a single crystal film and the films containing low angle boundaries in the initiation of plasticity is not significant. As the film thickness is increased, emission of dislocations from the low angle boundaries occurs at lower stresses and the behavior differs significantly from that of single crystal films of the same thickness. Figure 4.7 shows the peak contact pressures for all samples tested as a function of film thickness. The peak pressure decreases as the film thickness increases. Despite different misorientation angles, samples 1 and 2 shows similar basic trends. Analyzing the differences in the response of the two samples we note that the sample where the dislocations comprising the boundary are individually resolved with no overlapping cores presents slightly more efficient heterogeneous nucleation sites. A larger number of samples containing different types of grain boundaries would be required to obtain correlations between the grain boundary structure and its efficiency as heterogeneous nucleation site that are statistically meaningful.

These results can be interpreted using a simple model as follows: In the larger films, the initial defects provide sources to form dislocation loops, while in the smaller films these sources can still be present but there is not enough space between the surface of the film and the substrate to generate a dislocation loop. To interpret these results quantitatively, we postulate that the stress necessary to emit the first dislocations from the grain boundary as a loop is composed of two parts. The first is the stress necessary to form the dislocation within the grain boundary and the second is the stress necessary for that dislocation to bow out and be emitted into the bulk of the film. The first part can be expected to be independent of film thickness and the second part can be treated in analogy with the stress necessary to activate a Frank-Read source.

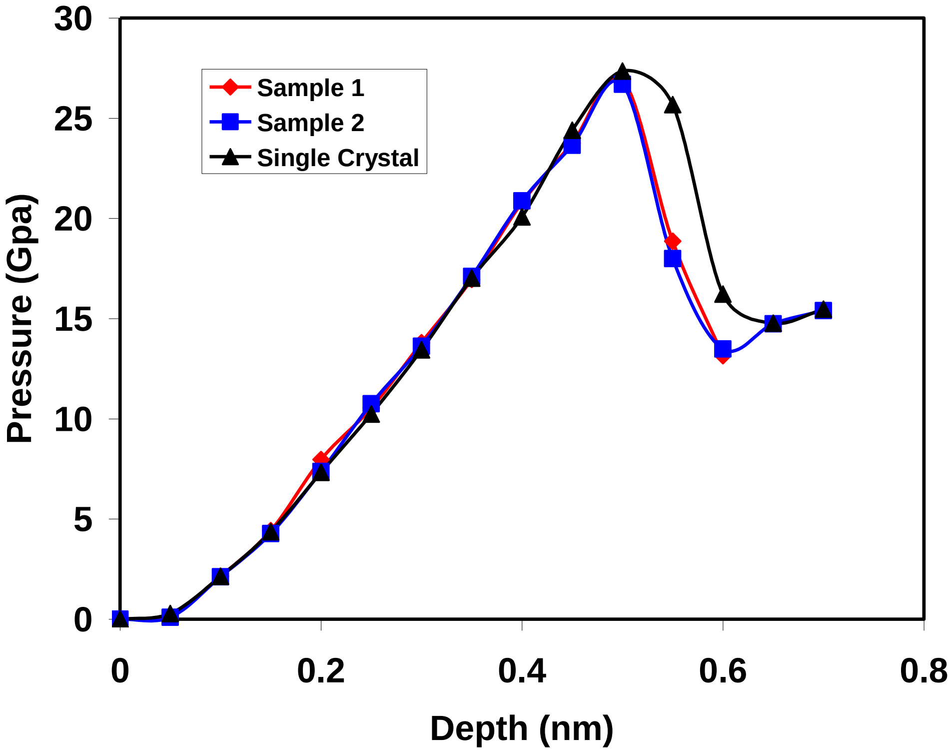

(a)

Figure 4.6: Effect of low angle boundaries for films of a) 4nm b) 6nm c) 8nm d) 12.8nm

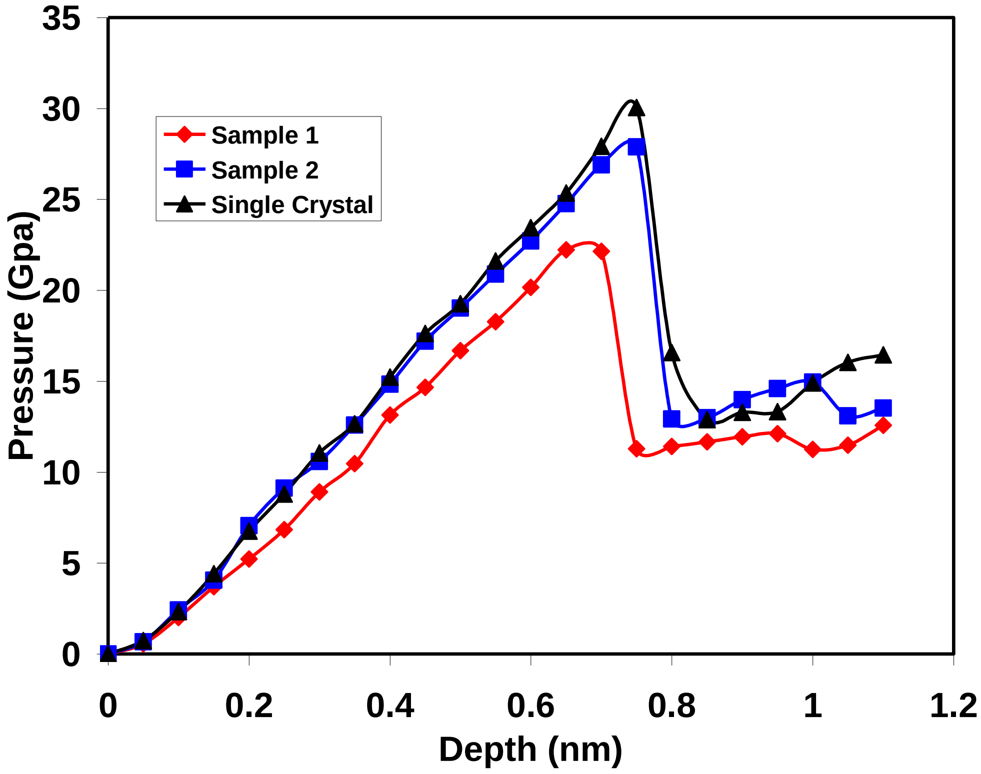

35
30
25
20
15
10
5
0
Pressure (Gpa)
0
0.2
0.4
0.6
0.8
1
1.2
Depth (nm)
Sample 1
Sample 2
Single Crystal

(b)

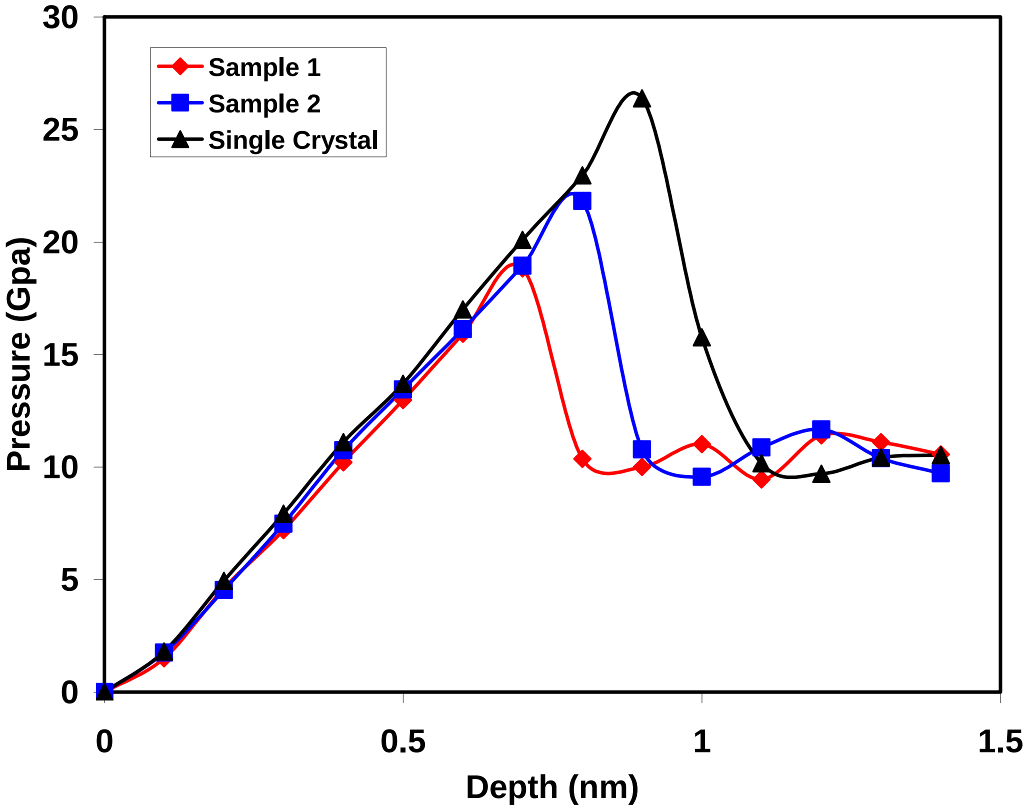

30
25
20
15
10
5
0
Pressure (Gpa)
0
0.5
1
1.5
Depth (nm)
Sample 1
Sample 2
Single Crystal

(c)

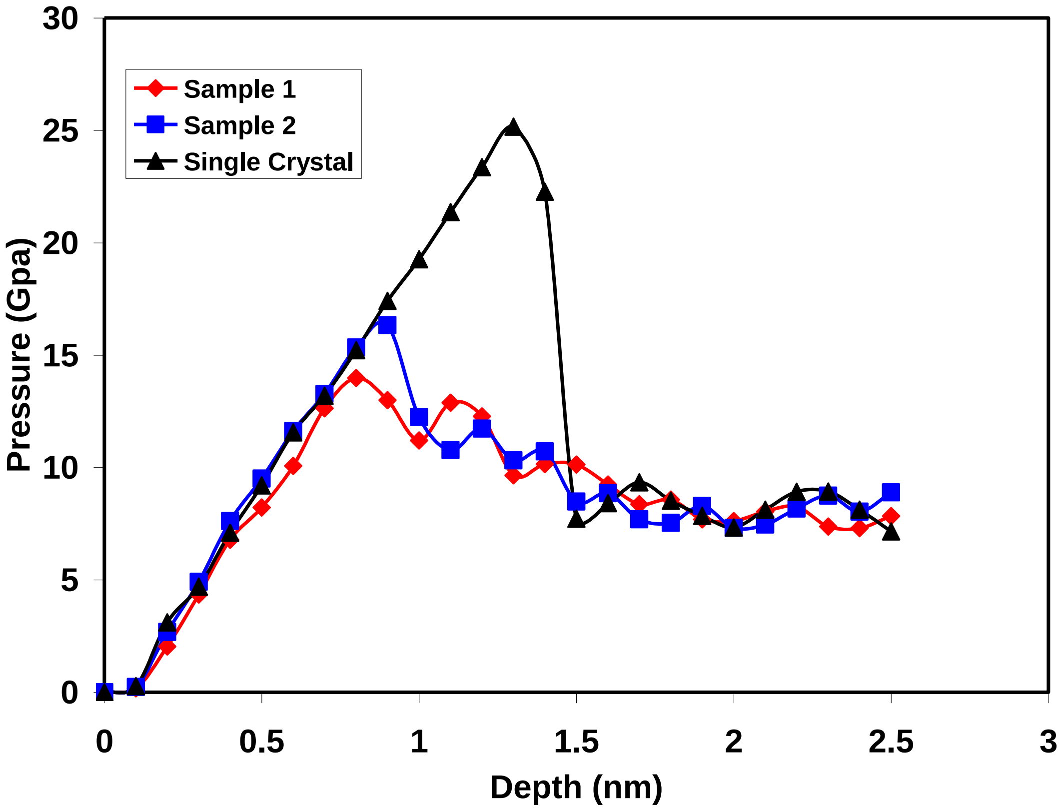

(d)

In this scheme the stress necessary to emit the dislocations from the defective films is given by [66]

$$\sigma^* = \sigma_0 + 2\mu b / L \qquad (4.2)$$

Where σ_0 is the stress to form the dislocation at the grain boundary site, μ is the shear modulus of nickel with a value of 76 MPa, the Burgers vector b = 0.25 nm and L the diameter of the dislocation loop. L is limited by the film thickness and equation (4.2) can be used to fit our data using the film thickness as the maximum dislocation loop diameter. If the data of figure 4.7 are fit to equation (3.2) in this manner, we obtain a value of σ_0 of approximately 14 GPa. This value is about half of that required to emit the first dislocation in single crystal films and it represents the stress necessary to create a dislocation in the boundary. In this model, the stress necessary to emit a dislocation from the LAGB is clearly size dependent, as shown in Figure 4.7. The critical step in the model is to break this stress into two parts. One is size independent and it corresponds to the formation of the dislocation inside the boundary, a necessary first step in the emission process. This value is not the same as the size independent value to nucleate a dislocation homogeneously in the single crystal. On the contrary, it is significantly lower because of the fact that the dislocation is formed in the boundary region. The second part of the emission stress is the stress necessary to bow out this dislocation away from the boundary into the grain. This stress depends on the bow out radius and is limited by the film thickness, giving the observed size dependence.

After the yield point the contact pressure decreases significantly in all cases, and it is approximately the same for the single crystals and the samples containing low angle boundaries. This points out to the role of the low angle boundaries in making the initial emission of the first dislocation easier but not significantly affecting the response after that initial yield event.

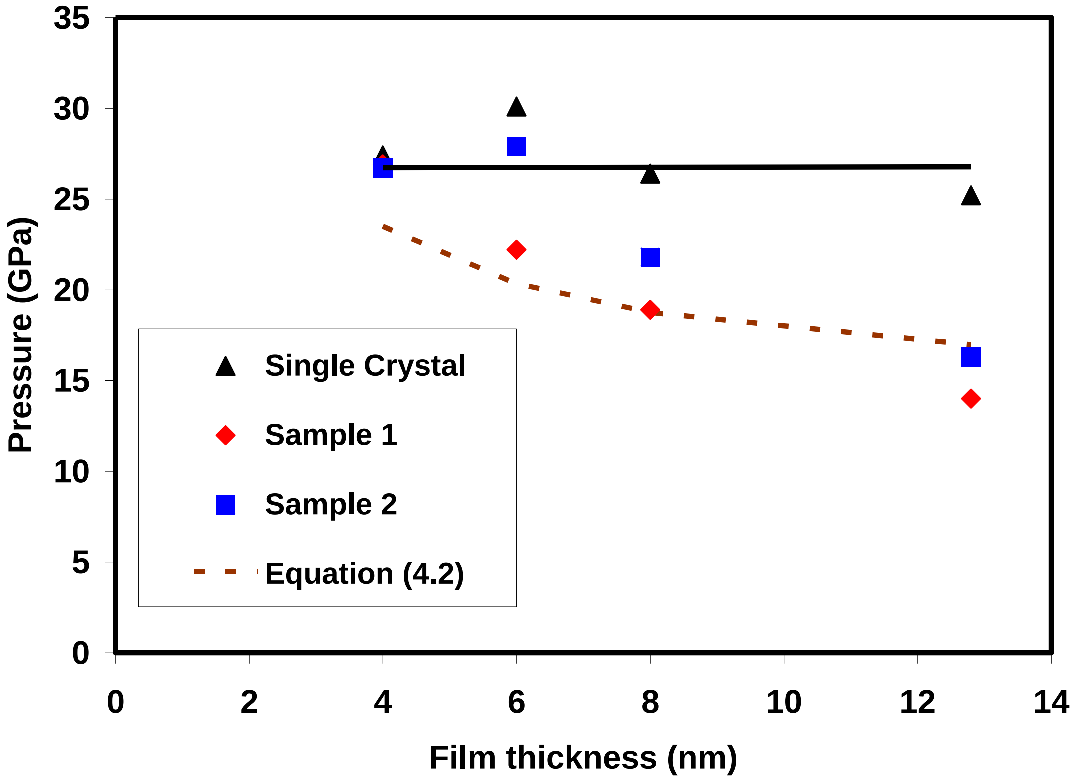

Figure 4.7: Peak contact pressures for all samples tested as a function of film thickness. Predictions of pressure using equation (5) are shown using dashed line.

The stresses observed after dislocation emission are significantly dependent on the film thickness. Figure 4.8 shows the contact pressure values observed after the initial dislocation emission event. For the thicker films the contact pressure values after the initial burst are significantly lower than those observed in the thinner films. There are two factors that may contribute to this effect. The first is that for the thinner films the initial burst occurs at lower indentation depths and there is a well known dependence of hardness on indentation depth for films, where the square of the hardness increases linearly with the inverse indentation depth (see for example Zhang et al. [34]. The second factor is the fact that, as shown in Figure 4.3, there are more dislocations emitted in the thicker films thus relieving stress. This results in lower hardness after the burst for the thicker films. These two factors can contribute to a very significant decrease of the hardness after the burst as the indentation depth is increased. Note that Figure 4.8 shows the contact pressures after the dislocation burst as a function of film thickness and therefore cannot be directly compared with the indentation size effects studied by Zhang et al. [34], even if they show similar trends.

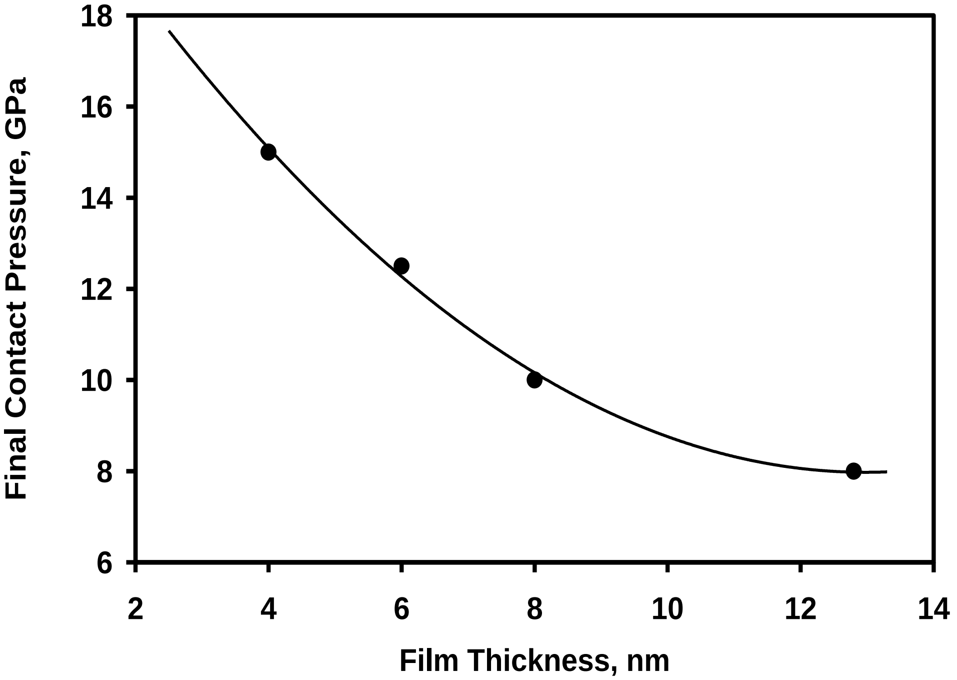

Figure 4.8: Final contact pressures as a function of film thickness

Chapter 5

Nanoindentation of Thin Films: Simulations and Experiments

5.1 Introduction

One of the most important applications of nanoindentation is the determination of the mechanical properties of thin films. In nanoindentation tests, the properties of the thin film may be measured without removing the film from the substrate as is done in other types of testing. The spatial distribution of properties, in both lateral and depth dimensions may be measured. Apart from testing films in situ, nanoindentation techniques can also be used for films made as free standing microbeams or membranes [67].

A simulated load depth curve allows comparisons to be made with actual experimental data. For example, such comparisons may yield information about nonlinear events such as cracking or phase changes that might occur with an actual specimen during an indentation test. In this chapter molecular dynamics simulation is used to study different aspects of nanoindentation such as indentation rate effects, substrate properties and different radius effects in the elastic and plastic regions of the pressure versus displacement plot. The simulation results for two different interatomic potentials are compared with experimental results for a 20 nm thick Ni film. These simulation methodologies are helpful in capturing the experimental effects in future studies of nanoindentation.

5.2 Simulation Setup

A sample of single crystal film was generated for a thickness of 20 nm oriented in [111] direction. The dimensions of the sample are 52 nm along the $[1\bar{1}0]$ direction and 52 nm along the $[11\bar{2}]$ direction. The sample size is significantly larger than the indentation contact area at maximum depth, and the spurious effects originating from the finite size of the sample in these directions can be avoided. Before the indentation process, all the samples were relaxed for 100 ps at 300 K using molecular dynamics as implemented in the LAMMPS code [42]. This relaxation was performed with free surface boundary conditions for the top of the film and a fixed layer of atoms to represent the substrate. The boundary conditions in the directions contained in the film are periodic.

In order to study the effect of different interatomic potential the 20 nm thick film with [111] orientation is used and potential developed by Mishin et al [45] and Voter et al [46] was employed to carry out the comparison. All other simulations carried out in this chapter used Voter potential. To analyze the influence of rate (velocity of indenter) in nanoindentation, indentation was carried out for two different indenter velocities. In the first case indenter velocity was chosen as 0.1nm per 100ps and in the second case it was one fourth of the first case (0.25 nm per100ps). Two different types of boundary conditions are used to represent different properties of substrates as described below.

Two different substrate effects studies carried out here are one where the substrate is hard and is not allowed to expand and another allowing substrate an in-plane expansion. For the indenter velocity comparison and substrate studies, the film thickness is 12.8 nm with (111) orientation. This selection was done to save computational time. Finally, comparison of the pressure versus depth results from the MD simulation was compared with experimental results for the 20nm Ni single crystal film.

5.3 Results and Discussion

5.3.1 Indenter speed effects

Figure 5.1 show that two different indenter velocities have no significant effect on the thin film in the elastic region and the hardness values. In the plastic region however the oscillations in the pressure versus depth curve indicate that the dislocations emitted in this region are more captured by the slower velocity as compared to the faster one. Overall response of the material in this region is not affected by the indentation rates. Studies done by Parkala et al [30] show that the nanoindentation hardness has no strain rate dependency in both nanocrystalline and commercial pure nickel in the range of 0.05–0.15 s^{-1}. However, there are slight sensitivities to the change of strain rates in the nanocrystalline pure Ni in indentation depths less than 500 nm with Berkovich, Cubecorner, and Conical indenters.

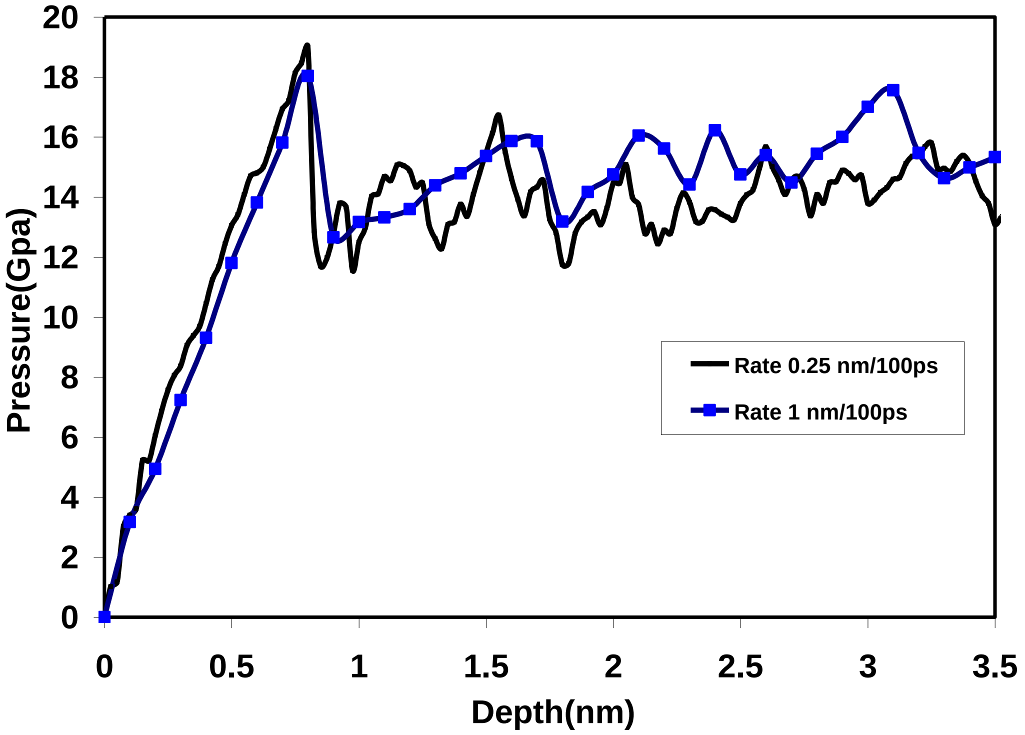

Figure 5.1 Comparison of pressure curves for indentation rate effects for a 12.8 nm Ni thin film.

5.3.2 Boundary conditions representing the substrate

Two boundary conditions studied here are Bc-1 (Thin film on a hard substrate, with no in-plane expansion) and Bc-2 (Thin film on a substrate that allows an in-plane expansion). Figure 5.2 shows that Bc-1 and Bc-2 show no effect in the elastic region. However, in the plastic region the pressure curves start to deviate at about 15% of the film thickness. This implies that the substrate is having an effect on the indentation process at such depths. Similar substrate effects have been observed by Saha and Nix [68] where the hardness has an effect on the substrate chosen for nanoindentation. Studies by Wang et al [69] show that the intrinsic film hardness can be acquired with indentation depths of less than 12% and 20% of the film thickness for soft films on hard substrates.

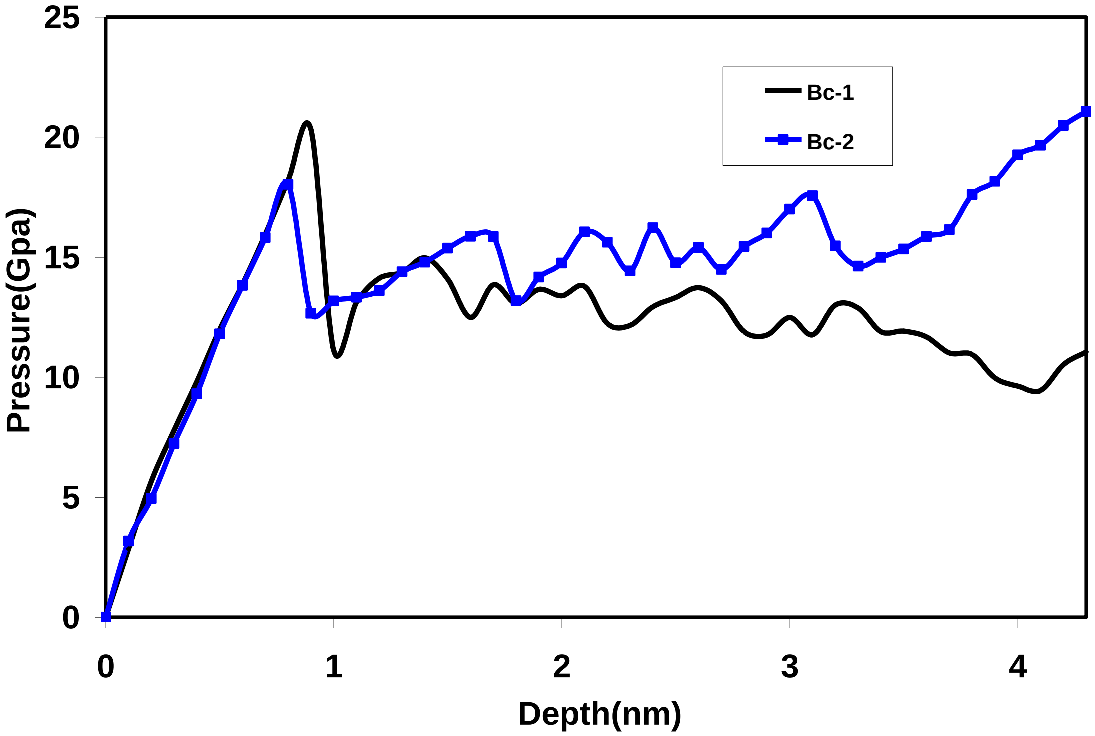

Figure 5.2 Comparison of pressure versus depth curves for two different boundary conditions for a 12.8 nm Ni thin film.

This is consistent with the experiments where the maximum depth of penetration is restricted to 10% of the film thickness, although research suggests that this rule has no physical basis[70].

5.3.3 Effects of the indenter radius

In order to study the effect of different radaii in nanoindentation the pressure versus displacement curves are plotted for two different radiuses of 15 nm and 30 nm. Figure 5.3 shows that the stress required to emit the first dislocation is independent of the radius of the indenter.

The elastic region shows a radius effect since the pressure has an inverse square root relation with the radius of the indenter as defined by the Hertzian theory. As the indentation depth increases, the effect of different radii becomes more obvious, due to substrate effects. Indentation hardness tests done in sub micron scale by Lu and Bogy [71] using finite elements show that for an aluminum layer on a silicon substrate, the hardness is relatively insensitive to the tip radius. On the contrary, for a silicon layer on an aluminum substrate, the hardness is much more sensitive to the tip radius.

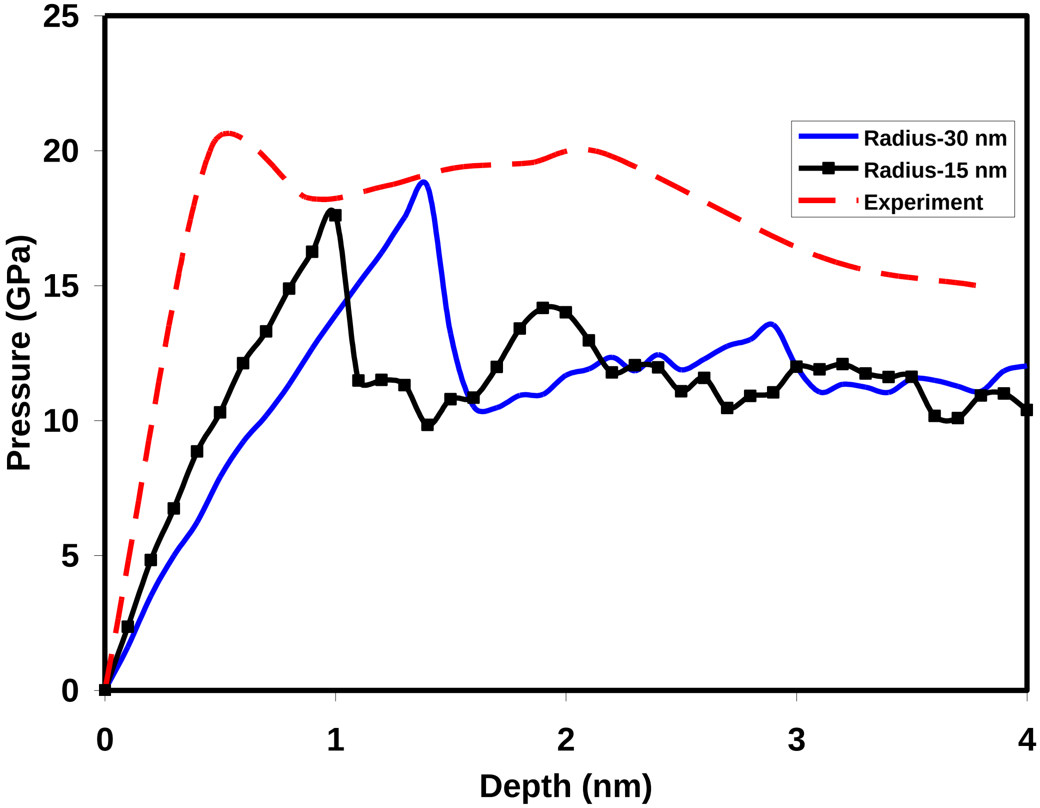

Figure 5.3 Comparison of pressure versus depth for different radaii for 20 nm Ni film.

5.3.4 Effects of the interatomic potential used.

In order to see which interatomic potential mimics the experimental results, two interatomic potentials for Ni were used. The pressure versus displacement curves (figure 5.4) indicate that the Voter-chen potential (hardness value 18.67 GPa) and the experimental results (hardness 20GPa) have approximately the same hardness value. The area used for the computation of pressure for both simulation and experiments are using equation (2.3). Since the experiments uses Berkovich tip, so for higher indentation depths the area function used here doesn't sufficiently represent the area. The Mishin potential however gives a high hardness of 27 GPa. This is due to the fact that the Mishin potential has been fitted to many more parameters compared to Voter potential and makes the movement of atoms harder. In the plastic region the experimental results follows neither of the two potentials and has higher pressure values. The experimental results also shows that the boundary condition one (Bc-1) is a better representation of experiments as compared to Bc-2, where the material shows hardening.

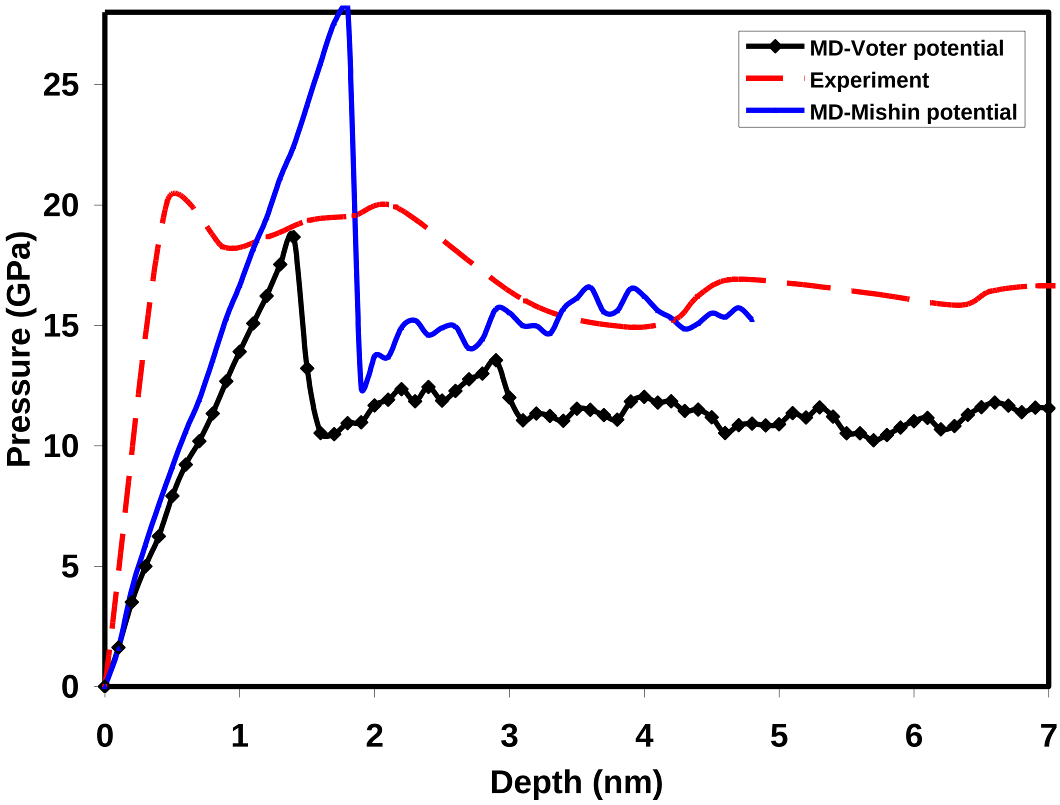

Figure 5.4 Comparison of experimental results with Voter and Mishin potentials for 20 nm Ni film.

Chapter 6

Dynamic Nanoindentation (Nano-Jackhammer effect)

6.1 Introduction

Dynamic indentation techniques are frequently used to measure the hardness of bulk and thin films. In some nanoindentation instruments this method is used to measure the contact stiffness. Dynamic indentation can be used to find the elastic modulus for viscoelastic solids [72, 73]. However, the oscillation alters the measured hardness value of ductile metallic materials.

Application of molecular dynamics simulation to study the cyclic plasticity has been explored by a limited number of researchers. For example, the atomic-scale material response of an FCC copper crystal substrate due to single and repeated indentation by a metal like or a covalent rigid tips was studied by Komvopoulos and Yan [74]. They investigated the evolution of deformation and heating in the substrate with indentation cycles and reported that the cyclic indentation gives rise to behaviors resembling cyclic hardening and softening observed at the macroscale. Cheong and Tanaka [75] have performed molecular dynamics simulation to study inelastic deformation and phase transformation of silicon single crystals under cyclic nanoindentation.

Analysis of quasi-static and dynamic indents have been performed recently [76] by a theory to describe this significant effects of the oscillations. The effect has been termed “Nano-Jackhammer Effect“. The objective here is to model the dynamic nanoindentation using molecular dynamics simulation and compare it with quasi-static indentation case and with the experimental results.

6.2 Simulation Setup

In the experimental setup 20 nm Ni/Al_2O_3 film with orientation in the (111) direction and a 50 nm radius Berkovich tip was used. The Quasi-static (DC loading) displacement rate was about 1 nm/s (20 μN/s loading rate) and the dynamic (AC loading) displacement rate was about 1 nm/s. Four different frequencies at which the indentation was carried out were 7.5 Hz, 25 Hz, 50 Hz and 75 Hz all with displacement amplitude of +/- 1 nm. A dynamic indent consists of a monotonic (quasi-static) loading rate of about 20 μN/s with an AC oscillation (dynamic portion) superimposed on top of the monotonic loading. The resulting loading curves are shown in figure 6.1.

In our simulation the embedded atom method (EAM) and molecular dynamics computational techniques [42] were used to examine the indentation of nickel thin film under both static and dynamic conditions in an effort to mimic the experiments. The simulation modeled contained a 20 nm thick Ni film, oriented along the [111] direction to mimic the experiments, and described by the Voter et al EAM interatomic potential [77]. The film contained up to 5.2 million atoms and the indentation was carried out using a spherical indenter of 30 nm radius. Periodic boundary conditions were used along the directions perpendicular to indentation direction. The rate of indentation for quasi-static case is 1 nm per 100 ps. For the dynamic conditions two different frequencies were considered (a) the indenter was moved 0.3 nm into the material and 0.1 nm up in each cycle (frequency-1) and (b) the indenter was moved 1.1 nm into the material and 1 nm up in each cycle (frequency-2). Since the molecular dynamics simulation has time scale limitation compared to experiments, we introduce a non dimensional parameter β which is given as

$$\beta = \frac{\text{Frequency of Indenter } (\nu) \text{ x Amplitude } (\lambda)}{\text{Average velocity of Indenter } (V)} \qquad (6.1)$$

This non dimensional parameter is defined in order to do a qualitative analysis of MD results and experiments. The values of β used for simulation and those of the experimental data are given in table 6.1.

Molecular Dynamics	**β**
Quasi-static case	0
frequency-1	1
frequency-2	10.5
Experiments	
Quasi-static case	0
Frequency 7.5 Hz	7.5
Frequency 25 Hz	25
Frequency 50 Hz	50
Frequency 75 Hz	75

Table 6.1 Non dimensional parameter for MD and Experiments.

The parameter β is actually the ratio of the oscillations amplitude to the net advance of the indenter during a cycle.

6.3 Results and Discussions

In order to compare the dynamic and quasi-static indentations, force of the indenter was plotted with depth of indentation for quasi-static and dynamic cases. Figure 6.1(a) shows the experimental results for dynamic nanoindenation of 20 nm thick Ni film oriented in [111] direction for quasi-static and four different dynamic frequencies [76]. Figure 6.1(b) shows the resulting loading curves for both static and dynamic conditions for molecular dynamics simulations. In figure 6.1(b) the average forces at indentation depths are plotted for both frequencies, and it is obvious that there is an effect due to dynamic indentation compared to quasi-static case. So, the higher the frequency, the lower the force required in the plastic region to penetrate in to the material. This qualitative analysis is comparable to experimental results which show similar effects. The results show that the effect is significant.

Figure 6.2 shows the dislocations emitted under the indenter for a penetration depth of 2.6 nm under both static and dynamic (β=1, case) conditions. The figures showing dislocations are created using the centro-symmetry parameter [58]. Atoms in perfect lattice positions are omitted, atoms in dislocation cores and stacking faults are shown in blue and atoms at the top surface of the film are shown in red. There are clearly more dislocations under dynamic loading conditions. This can be explained by the fact that when the indenter goes into the material it generates dislocations. When the indenter retrieves some of the dislocations are elastically recovered (figure 6.3), however the remaining dislocations act as source for new dislocations when the indenter comes back into material in the next cycle. This makes the material softer in the plastic region with increasing frequency. A quantitative analysis of the number of atoms in dislocation cores and stacking faults in both cases yields a 12% increase in dislocation emission under the dynamic loading with respect to the same penetration depth in the static case. Figure

6.4 shows the pressure versus non dimensional parameter at an indentation depth of 3.5 nm for both simulation and experiments. Even though the stresses predicted by simulations are somewhat below the experimental value, the trend indicates that stress at depth 3.5 nm decreases as β increases for both simulation and experiments. Compared to quasi-static indentation, dynamic loading of the indenter tip acts like a nano-sized jackhammer and generates more dislocations due to the added source of energy from the oscillation.

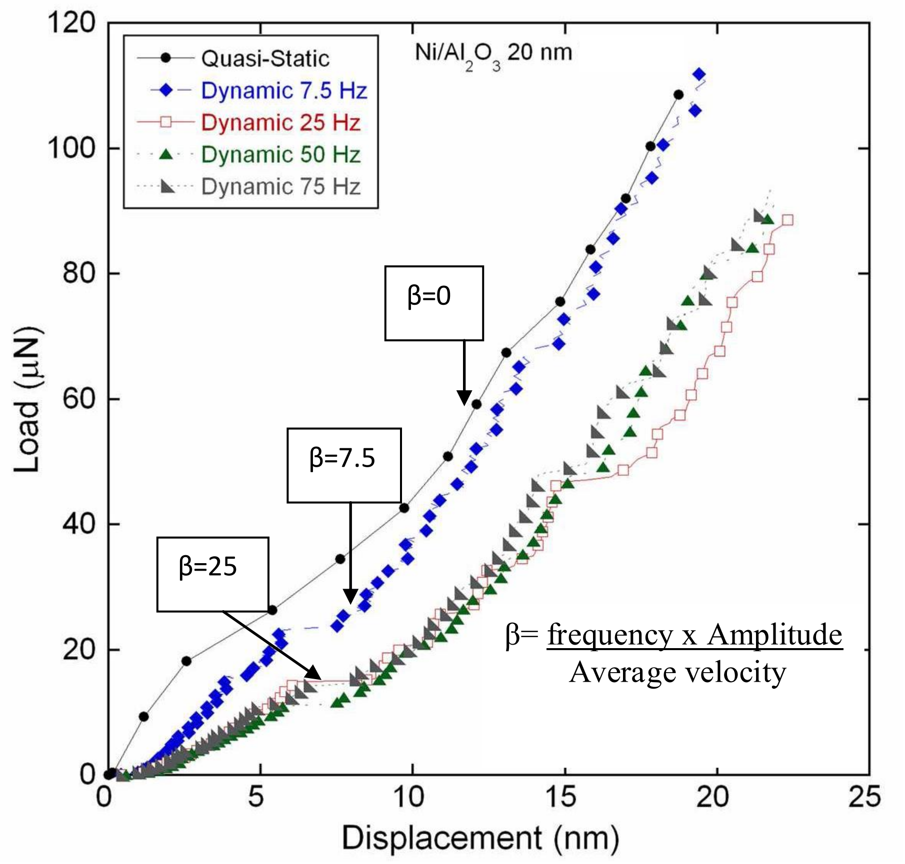

(a)

Figure 6.1 (a) Experimental results showing load-displacement curves of the first 20 nm of displacement for five different types of quasi-static and dynamic loading parameters performed on the Ni (111) /Al2O3 20 nm thick film [76]. (b) Loading curves for both static and dynamic condition from MD simulations.

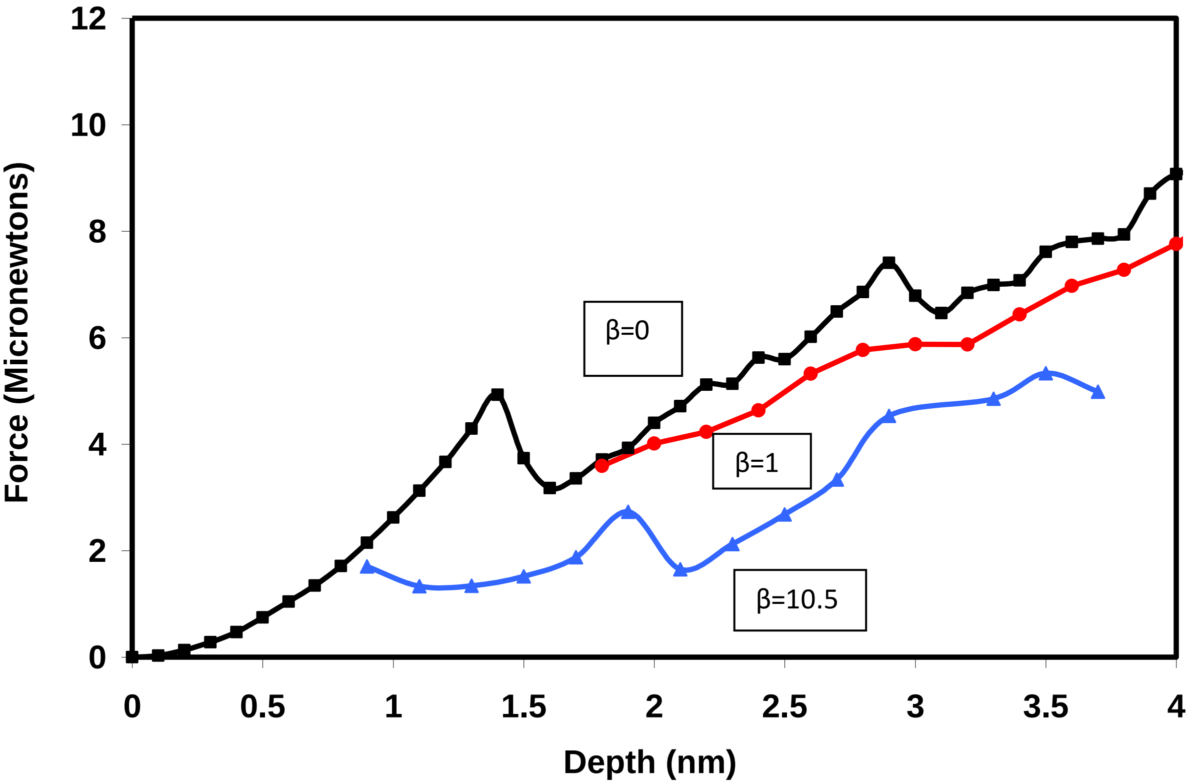

Force (Micronewtons)
0
2
4
6
8
10
12
0
0.5
1
1.5
2
2.5
3
3.5
4
Depth (nm)
β=0
β=1
β=10.5

(b)

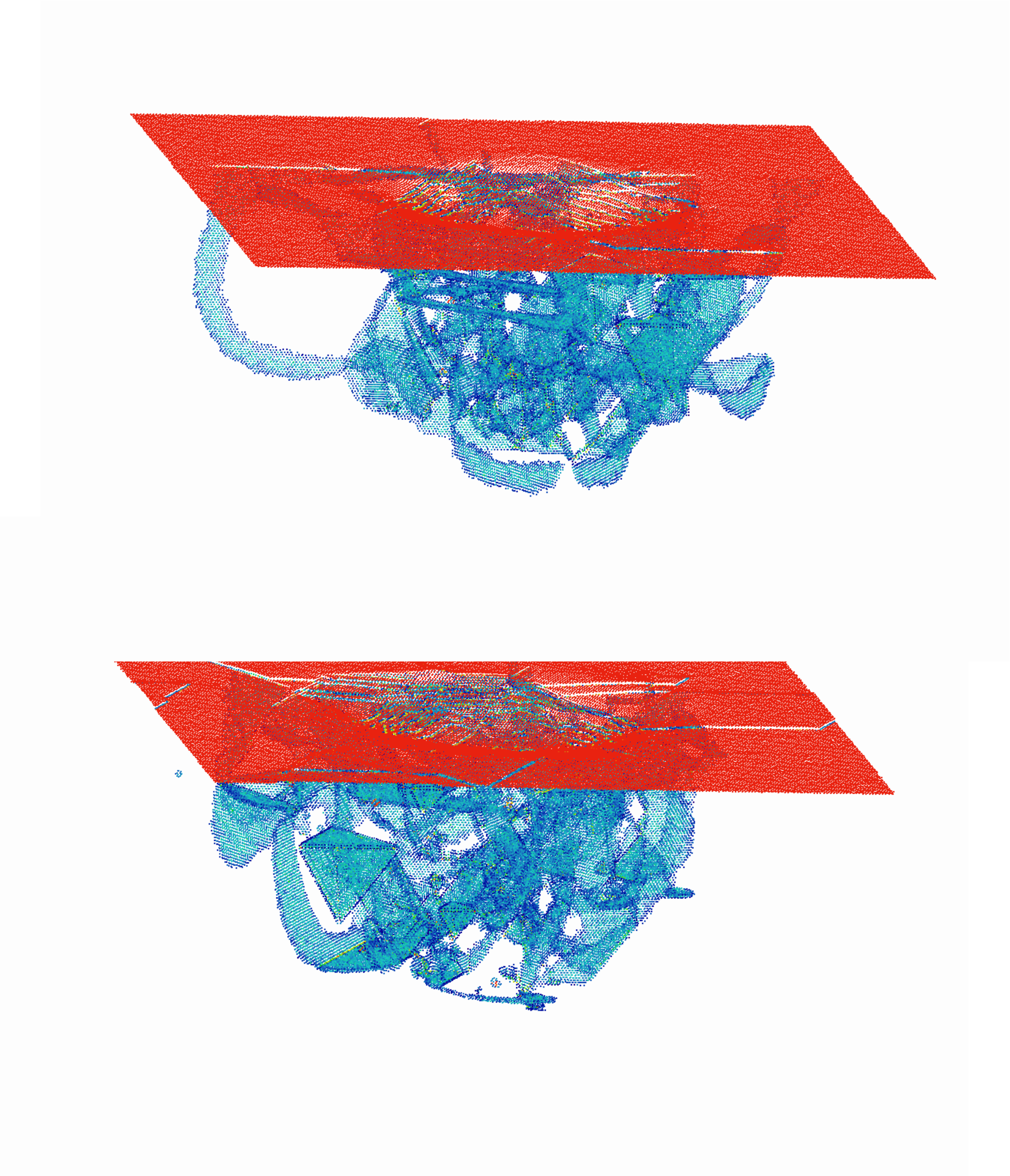

Figure 6.2 Dislocations emitted under the indenter for a penetration depth of 2.6 nm under static(top) and dynamic (bottom) conditions. Atoms in perfect lattice positions are omitted, atoms in dislocation cores and stacking faults are shown in blue and atoms at the top surface of the film are shown in red.

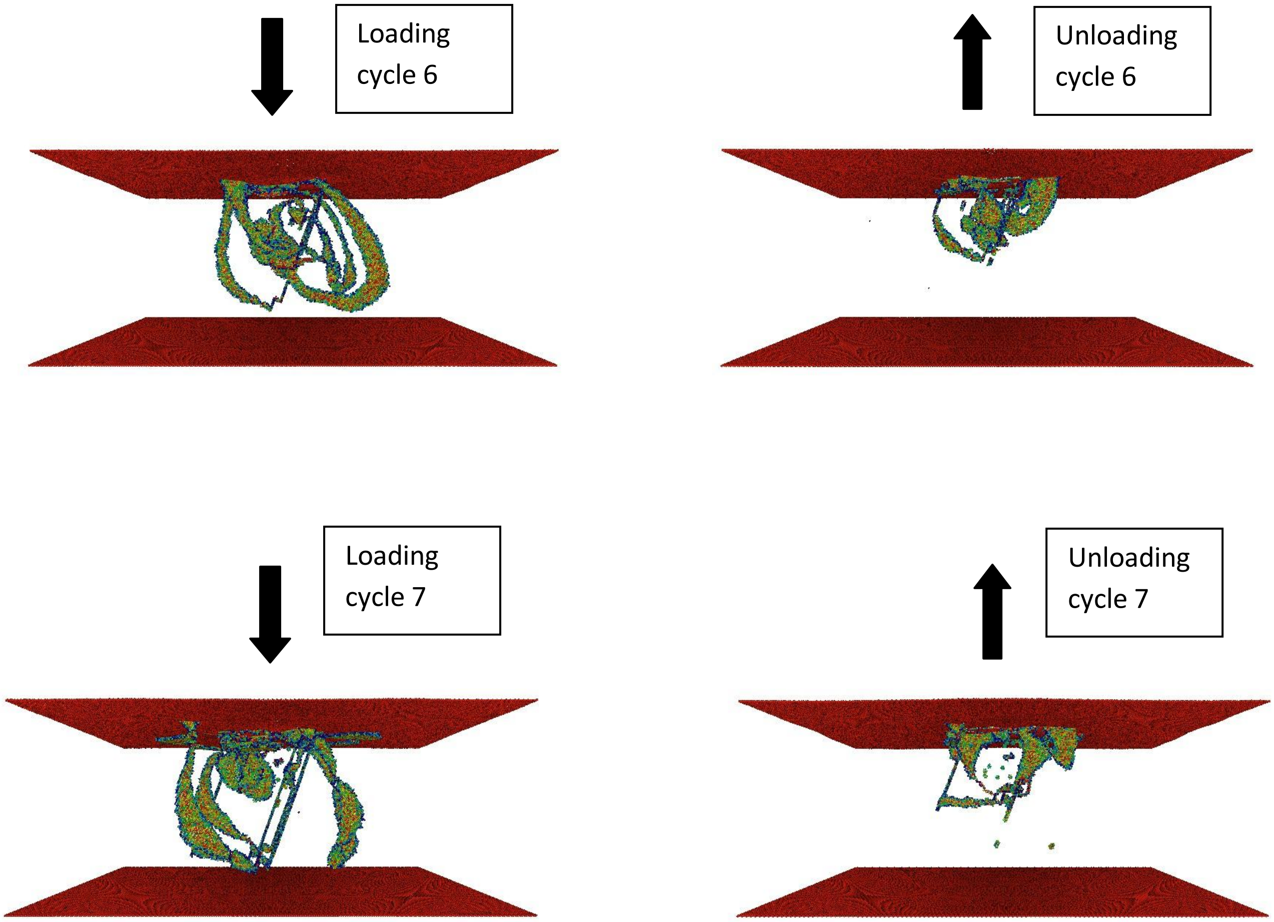

Figure 6.3 Dislocations emitted under the indenter for β=10.5 for cycles 6 and 7. Red atoms indicate free surface boundary condition for the top of the film and a fixed substrate for the bottom of the film. Each side of the loop consists of stacking-fault and is bounded by Shockley partials (blue colored atoms).

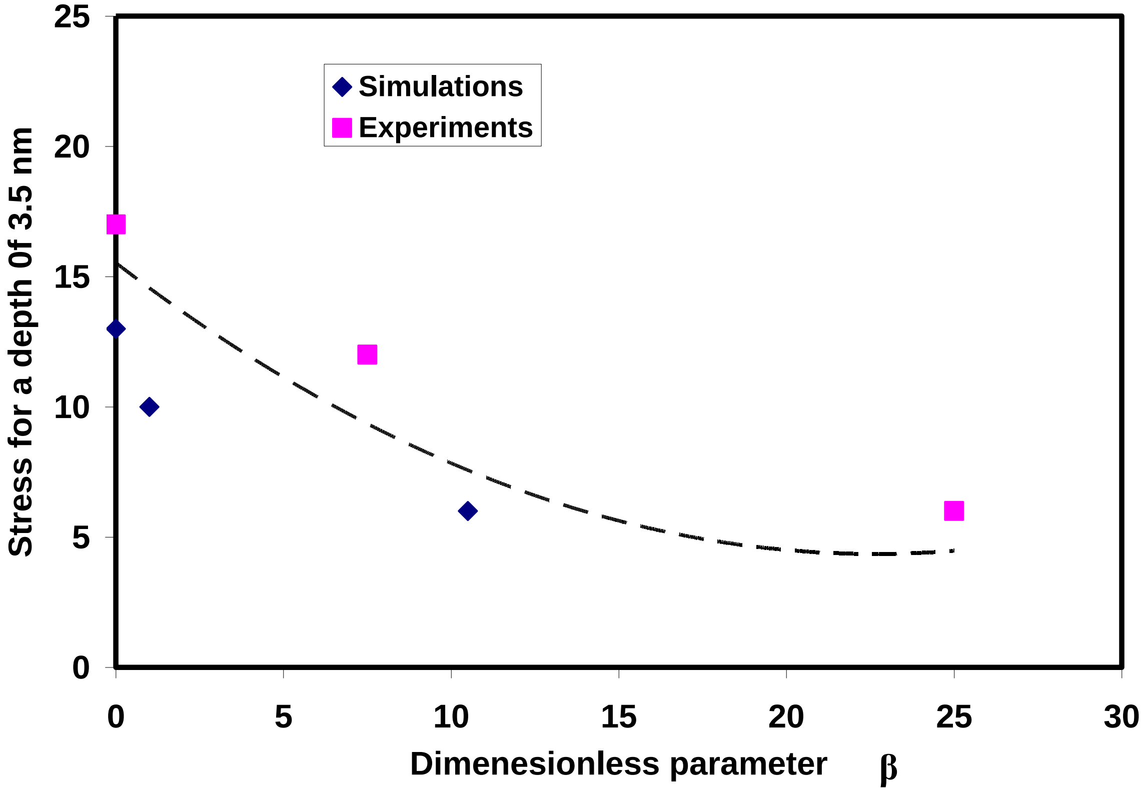

Figure 6.4 Comparison of MD and Experimental results for a depth of 3.5 nm.

Chapter 7

Nonlinear elastic effects in graphite/epoxy

7.1 Introduction

In this chapter acoustoelastic theory is used to predict the energy flux deviation in unidirectional gr/ep for zero stress state, applied normal and shear stresses as a function of fiber orientation angle. Flux shifts are also computed for comparing which waves generate maximum flux shifts for different fiber orientation angles. This was done for normal and shear stresses. Figure 7.1 shows the additional flux shift for QT waves generated due to an applied shear stress. Appendix A has the detailed description about the procedures involved in computation of energy flux

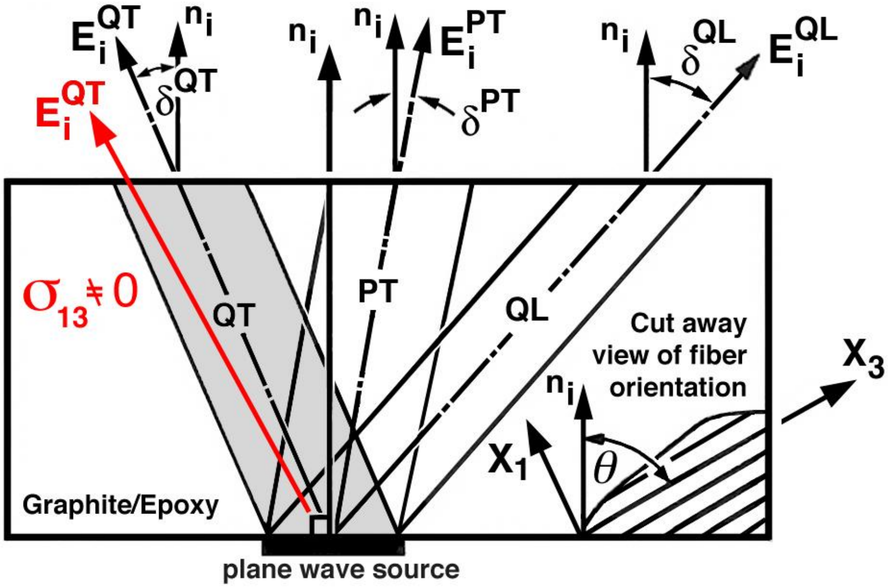

Figure 7.1 Additional flux shift in QT wave due to applied shear stress.

7.2 Computational Modeling

It was assumed that unidirectional gr/ep is transversely isotropic (hexagonal symmetry) for the computation of flux deviation angle for different stress states. The x_3 axis was taken as the fiber orientation axis and x_1 axis the laminate stacking direction. A positive flux deviation is defined as the energy flux deviation from the x_3 axis towards the x_1 axis; while a negative flux deviation implies that the energy deviates towards the x_3 axis. The elastic coefficients for gr/ep [7] are given in table7.1 and the nonlinear coefficients [7] in table 7.2. In both tables, the Voigt notation is used to simplify index tensor notation.

C_{ij}	(GPa)
C_{11}	14.26
C_{12}	6.78
C_{13}	6.5
C_{33}	108.4
C_{44}	5.27

Table 7.1 Linear elastic coefficients.

C_{ijk}	(GPa)	C_{ijk}	(GPa)
C_{111}	-214	C_{155}	-49.1
C_{112}	-89	C_{344}	-47
C_{113}	-4	C_{133}	-243
C_{123}	6.5	C_{333}	-325
C_{144}	-33.4		

Table 7.2 Third order (nonlinear) elastic coefficients.

Using equation (2.11) the flux deviation angles for the zero stress state were found for 0^o to 90^o of fiber orientation angle. The flux shift of QL, QT, and PT waves are computed for a shear stress of 0.1 GPa in the x_1x_3 plane and then a comparison of flux shift of QT wave was done with normal stress of 0.1 GPa along x_1 axis and 1.0 GPa along x_3 axis. In order to study the effect of shear stress in flux shift, the flux shift was found for QT wave under different shear stresses. In all of the above cases the flux shift was computed for fibers oriented from 0^o to 90^o at an interval of 1^o.

7.3 Results and Discussions

In this research the energy flux deviation of elastic wave propagating through gr/ep is measured due to an applied shear stress using acoustoelastic theory. Figure 7.2 shows the flux deviation angle for zero stress. All three wave forms QL, QT and PT exhibit flux deviation due to the anisotropy of gr/ep. QL and QT has more flux deviation as compared to PT. These results are in excellent agreement with that of Prosser et al. [7] and Kriz and Ledbetter [78]. The flux shift was also observed in gr/ep due to the moisture absorption by the matrix or fiber degradation [79].

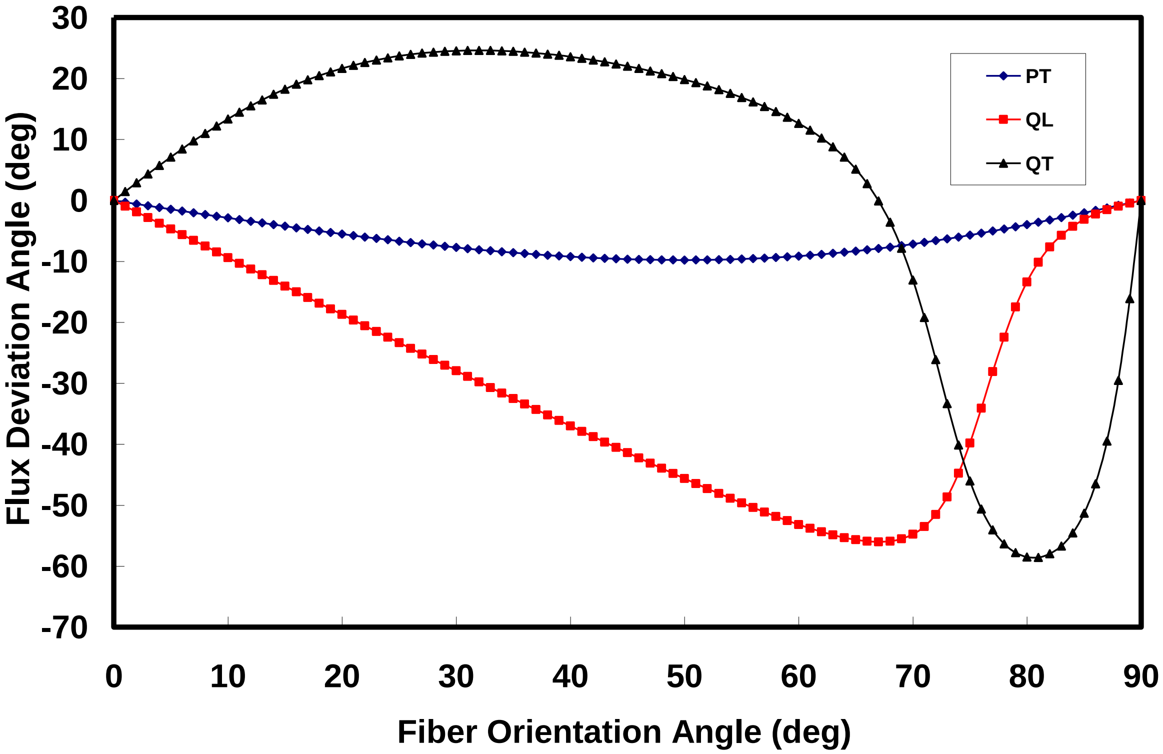

Figure 7.2: Energy flux deviation angle of QL, QT and PT waves in gr/ep with respect to fiber orientation angle under no applied stress.

In order to study the effect of normal stress on energy flux deviation, first a normal stress of 0.1 GPa was applied along the x_1 axis and then the flux shift due to each stress was plotted with respect to the fiber orientation angle. The QT wave exhibits the largest energy flux shift due to an applied normal stress along the x_1 axis while QL and PT has significantly small flux shift, this is consistent with Prosser et al. [7], thus expressing confidence in the results that follow.

A shear stress of 0.1 GPa is applied in the x_1x_3 plane in order to find the energy flux shift of QL, QT and PT as a function of fiber orientation angle (Figure 7.3). It is obvious from figure 7.3 that QT has the most flux shift, while QL and PT has flux shifts close to zero. The QT wave has a flux shift at 0^0 and 90^o due to the applied shear stress as compared with applied normal stresses which has zero flux shifts at 0^0 and 90^o. The QT wave has the maximum flux shift at 90^o fiber orientation of 12^o. The nonzero flux shifts at 0^0 and 90^o due to the shear stress is the result of the shear strain that is induced in the material. Unlike the strains caused by normal stresses, this small shear strain affects the particle vibration in the direction of the flux shift. A comparison is done for the flux shift of QT wave for normal stress of 0.1 GPa along x_1 and 1.0 GPa along x_3 axis with a shear stress of 0.1 GPa (Figure 7.4) in the x_1-x_3 plane. As the figure 13 indicates the flux shift in QT wave due to shear stress is larger than that of the normal stress cases. The higher flux deviation of QT wave due to the shear stress compared to that of normal stress can be explained by the fact that the effective stiffness tensor C^*_{nlij} has more components associated with the shear stress than normal stress. Moreover the values of these components are higher (more than 1% in some of the components) than that of the normal stress. Appendix A demonstrates which terms contribute the flux shift in QT waves due to shear stress.

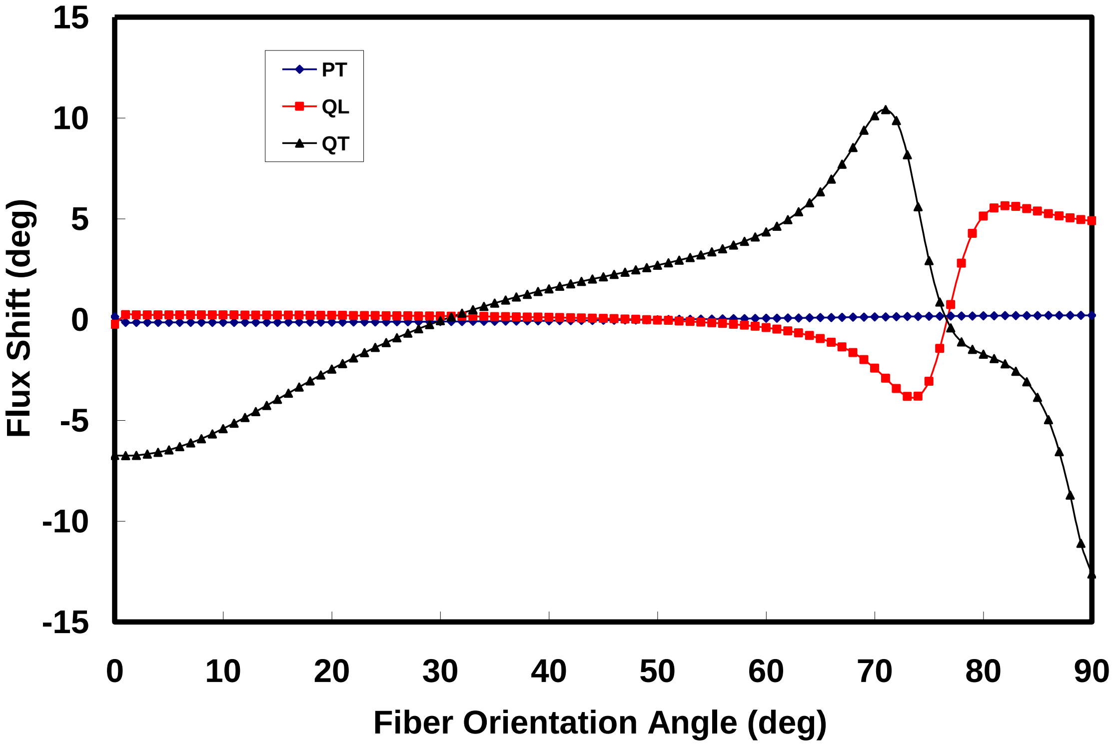

Figure 7.3: Energy flux shift of QL, QT and PT waves in gr/ep with respect to fiber orientation angle due to an applied shear stress of 0.1 GPa in the x_1-x_3 plane.

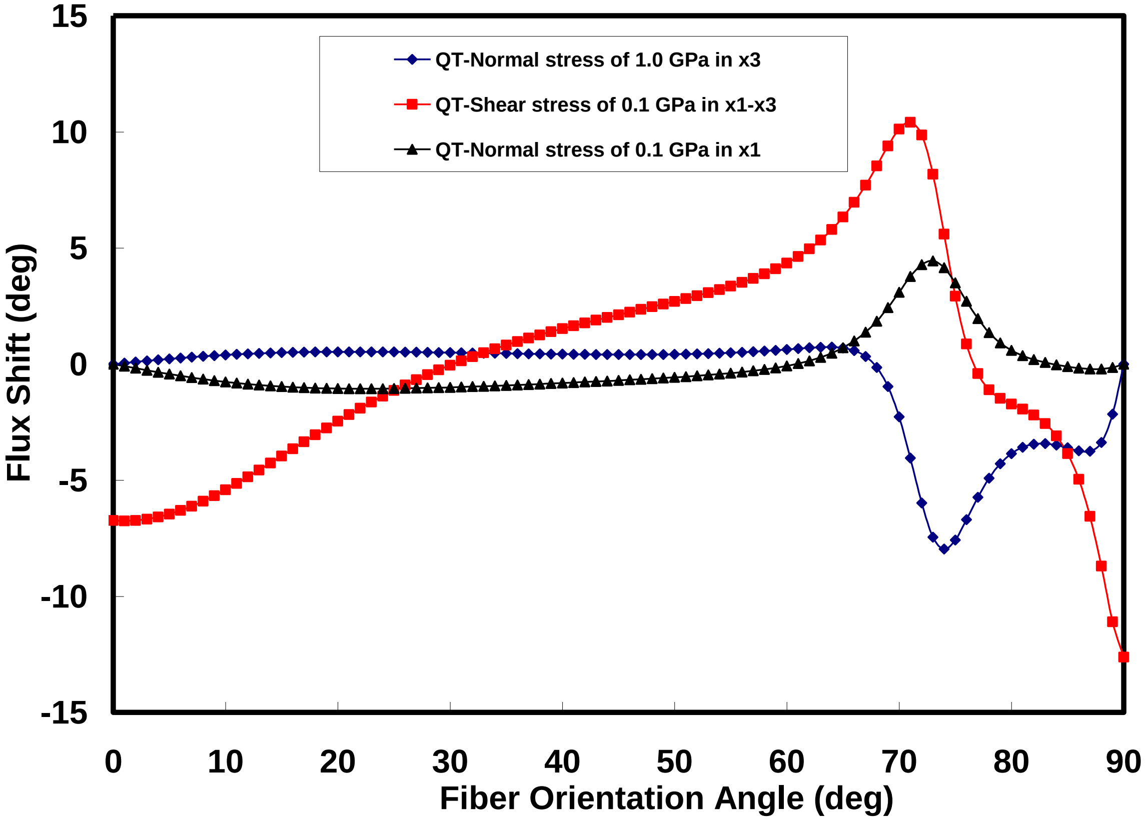

Figure 7.4: Comparison of flux shift of QT wave due to an applied shear stress of 0.1 GPa and an applied normal stress of 0.1 GPa along x_1 axis and 1.0 GPa along x_3 axis.

Since the QT wave has significant flux shift, shear stresses of 0.01 GPa, 0.02 GPa, 0.04 GPa, 0.08 GPa and 0.1 GPa are applied and the corresponding flux shift was plotted for QT wave with respect to fiber orientation angle (Figure 7.5), thus depicting that as shear stress increases the flux shift also increases. It is also found that the flux shift of QT wave has a linear variation with applied shear stress (Figure 7.6).

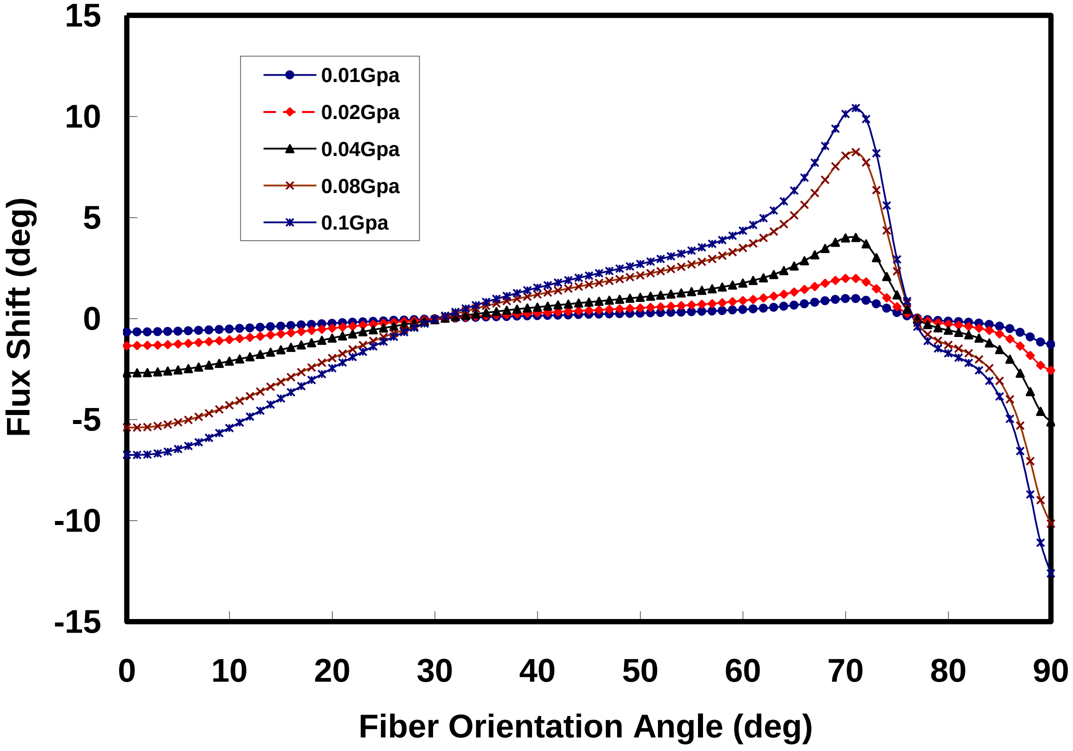

Figure 7.5: Energy Flux shift of QT wave in gr/ep as a function of fiber orientation angle due to applied shear stress of 0.01 GPa, 0.02 GPa, 0.04 GPa, 0.08 GPa and 1.0 Gpa in the x_1-x_3 plane.

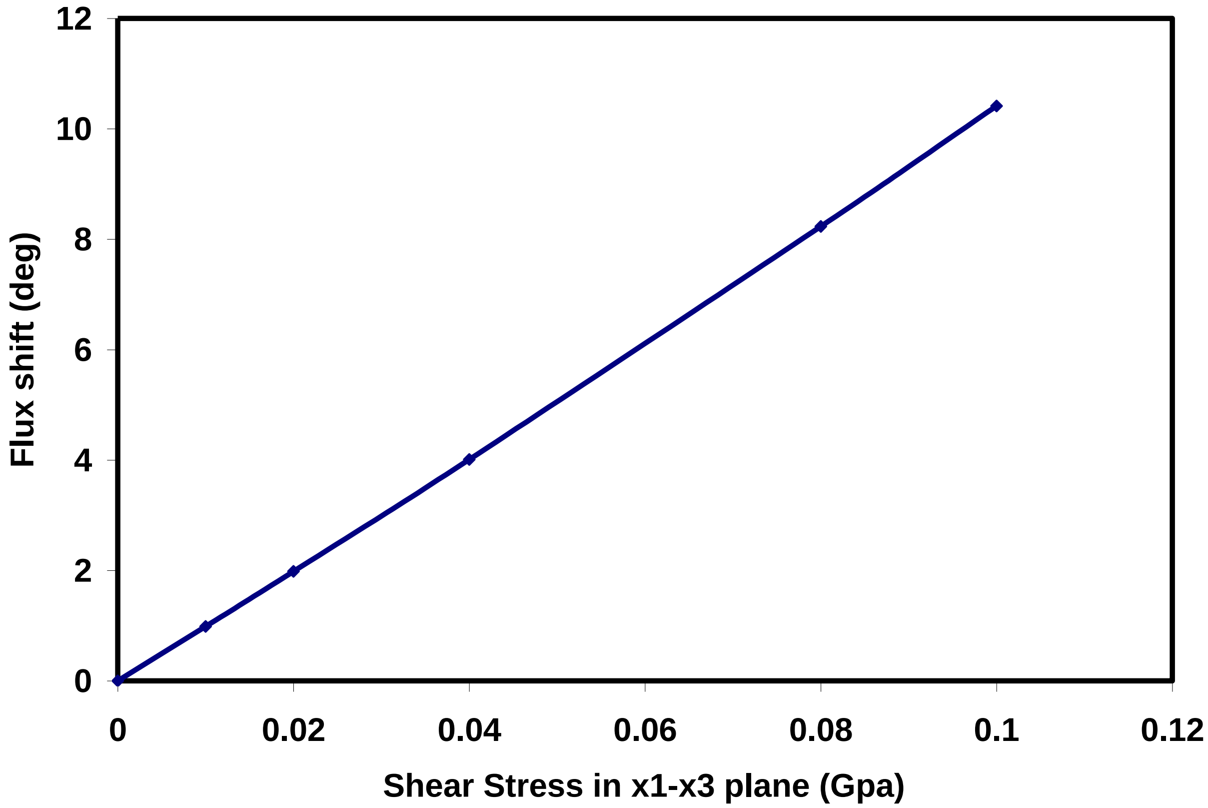

Figure 7.6: Energy Flux shift of QT wave in gr/ep as a function of applied shear stress in x_1-x_3 plane.

Chapter 8

Finite Element Verification of Energy Flux Shift

8.1 Introduction

In order to verify the energy flux shifts predicted by acoustoelastic theory due to an applied shear stress, finite element equations of motion is formulated and the energy flux deviations are computed. The computation of energy flux deviation was done for both zero stress state and applied shear stress state for every 10° interval of fiber orientation angle.

Finite element method has been used along with Newmark's method for predicting the flux deviations in unidirectional graphite/epoxy by Kriz and Heyliger [80] for QL and QT waves. The flux deviations were measured from the deformed mesh. Later the same methodology was employed to find the magnetic flux generated from a series of piezomagnetic materials embedded on a silicon substrate excited by elastic waves [81]. In this chapter the first part discusses the comparison with previously obtained results and second part compares the energy flux shift from finite element with flux shift predicted by acoustoelastic theory.

8.2 Stress waves in purely elastic media when applied stress is zero

Comparisons were made to test the accuracy of finite element equations developed in chapter 2 with known results.

8.2.1 Waves in a 1-D isotropic material

In this section the finite element model is used to study wave in 1-D isotropic material and results are compared with exact solution.

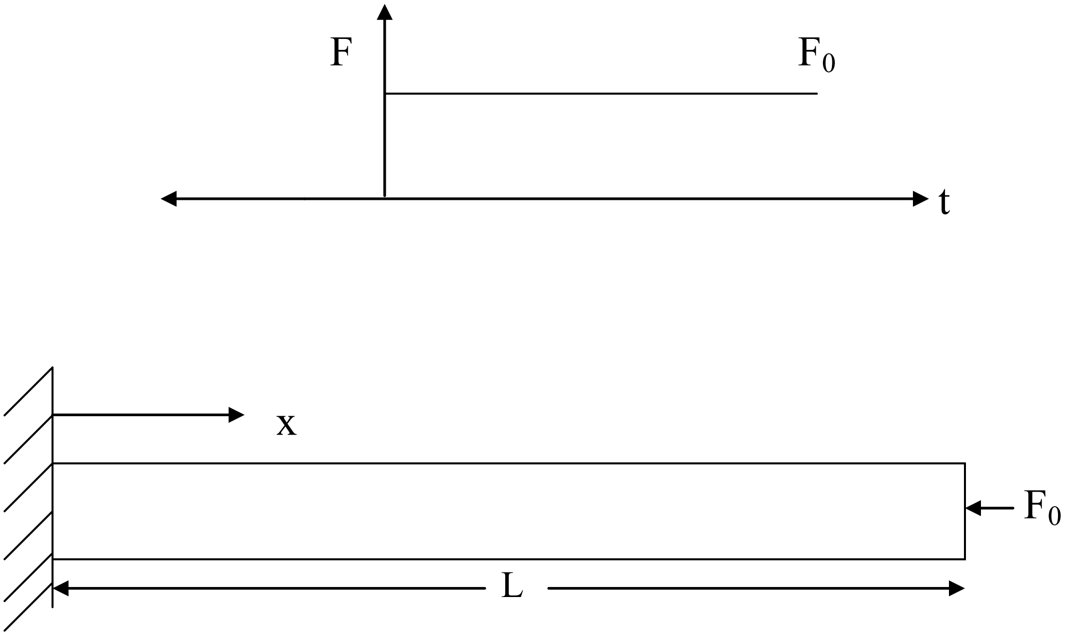

Figure 8.1 Problem geometry and constant force function.

Exact solution [82] for the problem above (Figure 8.1)is given by the following equation.

$$u(x,t) = \frac{8FL}{\rho A \pi^2 a^2} \sum_{n=1,2..}^{\infty} \frac{(-1)^{(n-1)/2}}{n^2} \sin(\frac{n\pi x}{2L})(1-\cos(\frac{n\pi a t}{2L})) \qquad (8.1)$$

Where F is the force applied, L is the length of the bar, A area of cross section, wave velocity, a= $\sqrt{\frac{E}{\rho}}$, t is the time and x is distance of any point inside the bar from the fixed end. The displacements are computed for x_1=L and x_1=L/2 for each time step and plotted against time (Figure 8.2).

In the finite element approximation to the problem 160 square elements were used where each element is a four noded quadrilateral isoparametric element with bilinear strain field. Each node has two degrees of freedom for the two displacements. The Newmark integration method was used for computing the displacements for each time step. IMSL subroutine DLSLRG was employed to solve the set of finite element equations, this subroutine is capable of solving a symmetric and unsymmetric set of linear equations. Two hundred time steps were used, each of which was 4.0e-6 sec. The Newmark constants α =0.25 and δ=0.5 were used as required by the constant-average-acceleration method. Numerical values used for this example are E = 1.0e7 lb/in^2, ν = 0.33, G = 3.76 e06 lb/in.^{2}, F = 4.0 lb, L = 40.0 in., ρ= 2.539 lb s^2/in^4, and A = 4 in^2. The displacements at the end and middle of the 1-D bar are plotted against time for both exact solution and the FEM results as shown in figure 8.2.

8.2.1.1 Results and Discussion

It is evident that the finite element method gives excellent results in comparison with the exact solutions for wave propagation in one-dimensional bar. The displacements at the end and middle of the 1-D bar are plotted against time for both exact (equation 8.1) and FEM results as shown in Figure 8.2. Hence it is evident from the Figure 8.2 that the finite element method gives excellent results in comparison with the exact solutions for wave propagation in one-dimensional bar. In order to check the deformed mesh, a sinusoidal force was applied to the bar and the deformed mesh was plotted (Figure 8.3) with respect to time. The number of elements in the mesh was increased to 640 and a time step of 0.25sec was used.

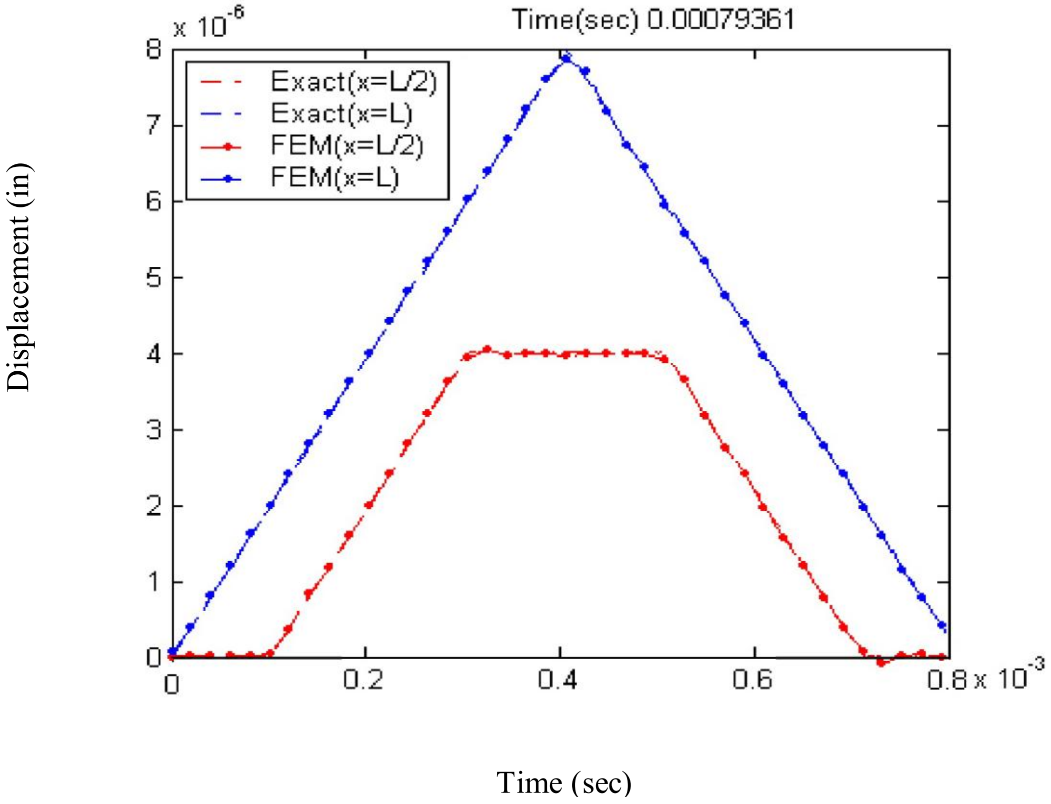

Figure 8.2 Comparison of Exact solution and FEM

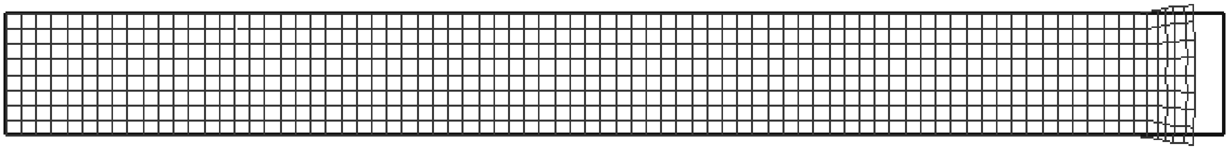

Time =1.25sec

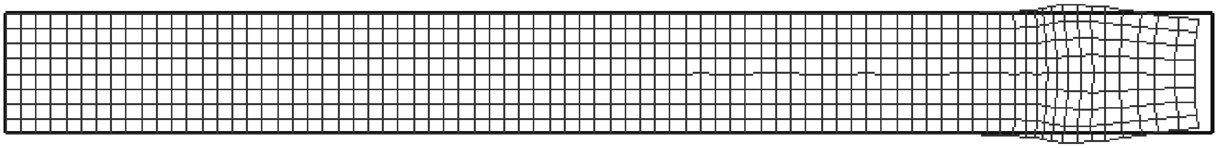

Time =2.5sec

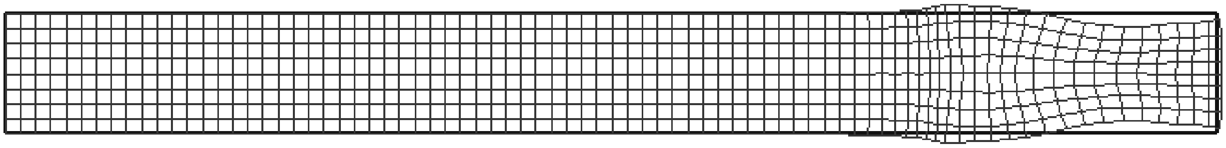

Time =3.75sec

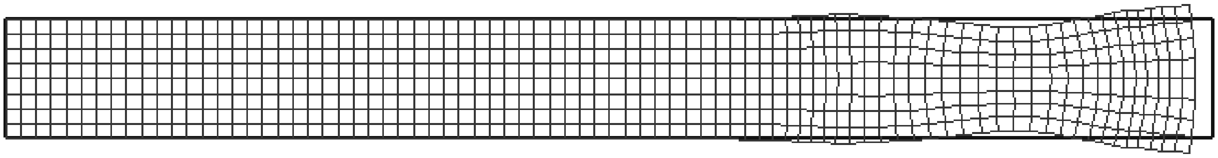

Time =5.0sec

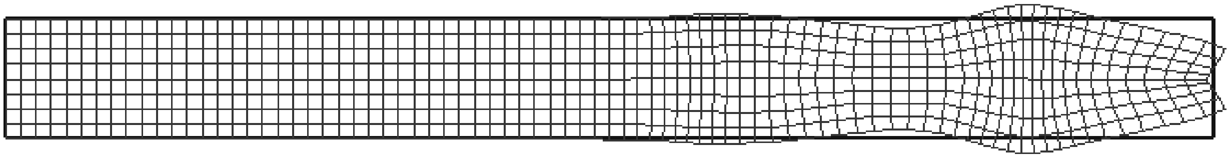

Time =6.25sec

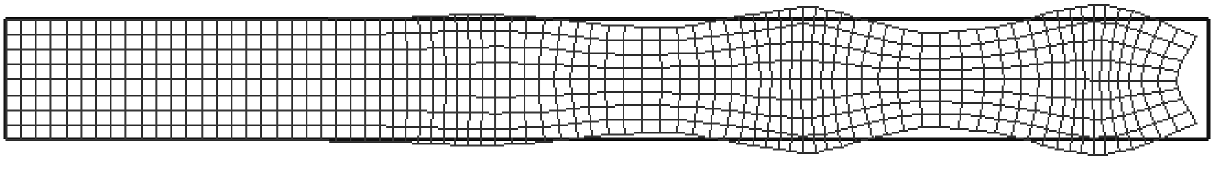

Time =8.75sec

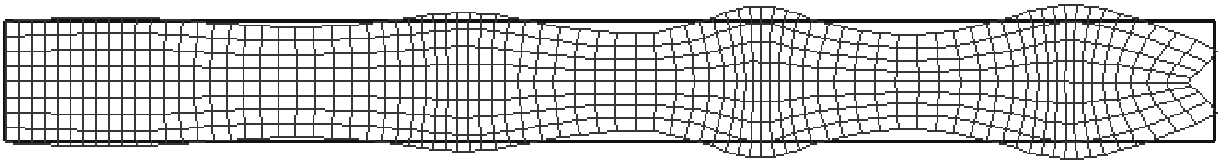

Time =12.5sec

Figure 8.3 Wave in 1-D bar due to sinusoidal force.

8.2.2 Dispersion of waves

When using finite elements to model wave propagation, dispersion is observed when wave velocity is a function of the number of elements contained within the wave length of a propagating wave. Here the study of dispersion in unidirectional graphite/epoxy, which is hexagonal and highly anisotropic. The objective is to study the effect of anisotropy on the flux deviation (group velocity) propagation direction as a function of different fiber orientations, 0 to 90 degrees.

In general the actual wave "group" velocity vector, energy flux deviates from the wave "phase" velocity, which propagates normal to the plane wave front. Between 0 and 90 degrees, group velocity deviates from the phase velocity and the pure transverse (T) wave becomes a quasi-transverse (QT) wave. At 0 and 90 degree fiber orientations the group and phase velocities are the same. This case is used here for simplicity to study dispersion of pure transverse (T) waves before we study dispersion at various fiber orientations.

In the accompanying figures 8.4 and 8.5 six different cases are outlined for a 30x60 FEM mesh. This small mesh size allows us to simulate many different cases of interest in a reasonable time using desktop computers. Increasing the number of elements at the boundary transducer results in an increase in the number of elements contained in the propagating T waves. For 12, 16, 20, and 24 elements per transducer wave length, we observe 3, 4, 5, and 6 elements respectively contained with in the propagating T wave. Another important observation is the increasing wave velocity with increasing number of elements per wave length contained in the propagating T wave. This is expected since larger number of elements contained in a propagating wave approach the ideal case of a wave propagating in a nondispersive continuum. With only 4 elements per transducer wave length the propagating T wave is alter by the FEM mesh, that is the group velocity is zero, which demonstrates significant dispersion. Dispersion exists even at 24 elements per transducer wavelength. However 24 elements per transducer wave length will require larger FEM meshes where QT waves are predicted to deviate as much as 25 degrees to the left. As in most cases when modeling complex phenomena simplifying approximations are necessary and results must be interpreted within these approximations.

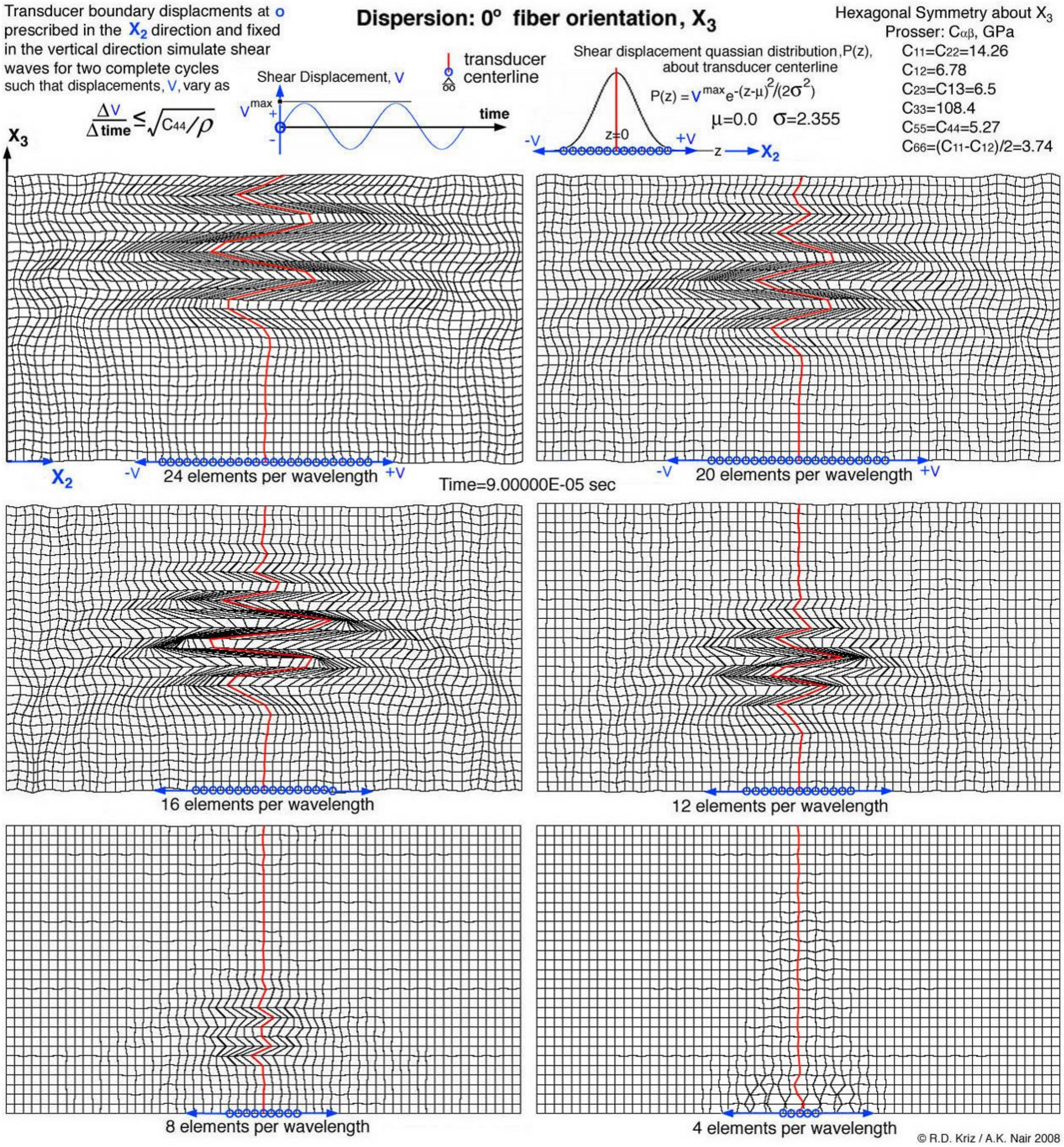

Figure 8.4 Wave dispersion in grapite/epoxy for 0° fiber orientation. (Movie_2)

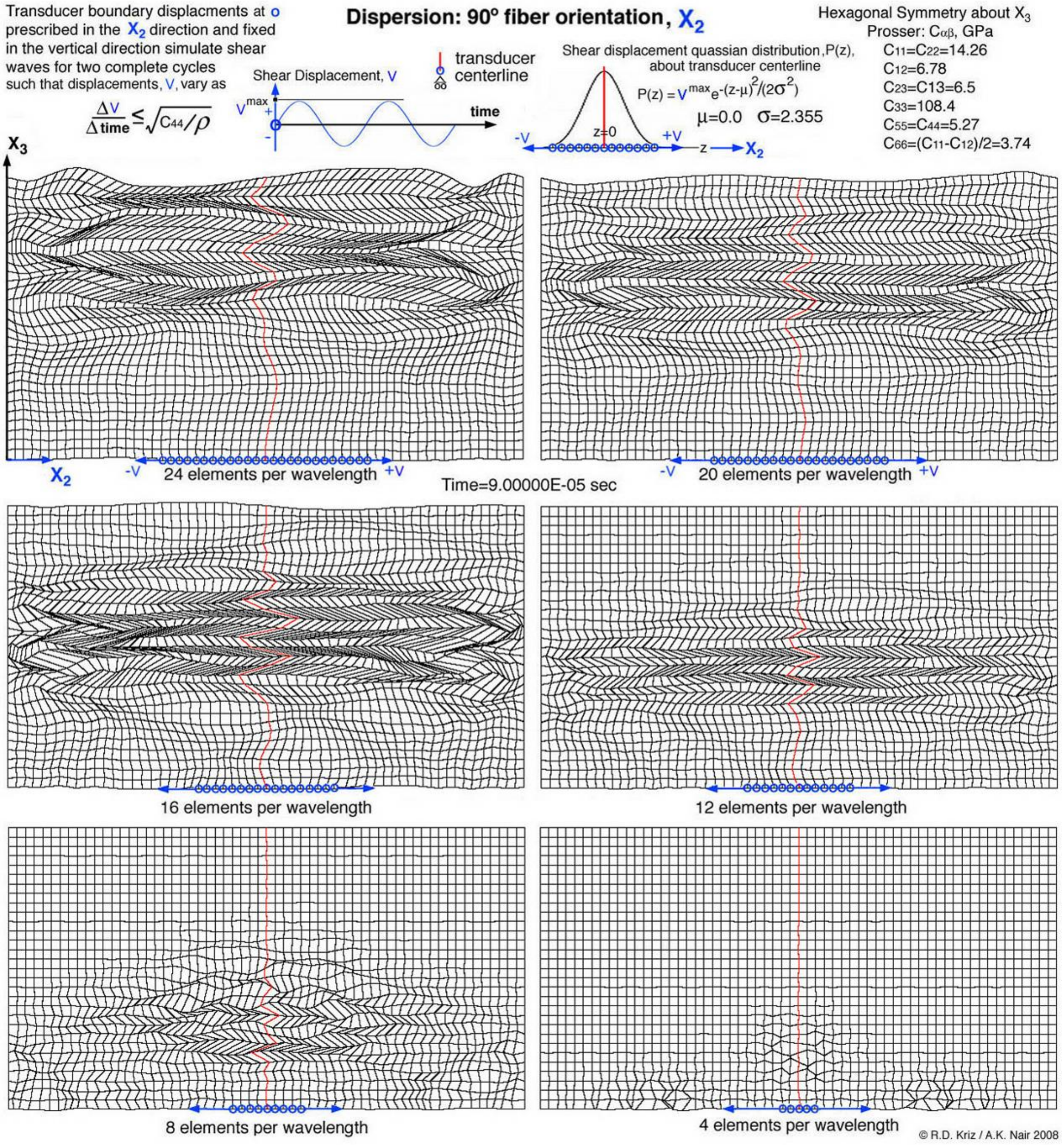

Figure 8.5 Wave dispersion in grapite/epoxy for 90° fiber orientation (Movie_3)

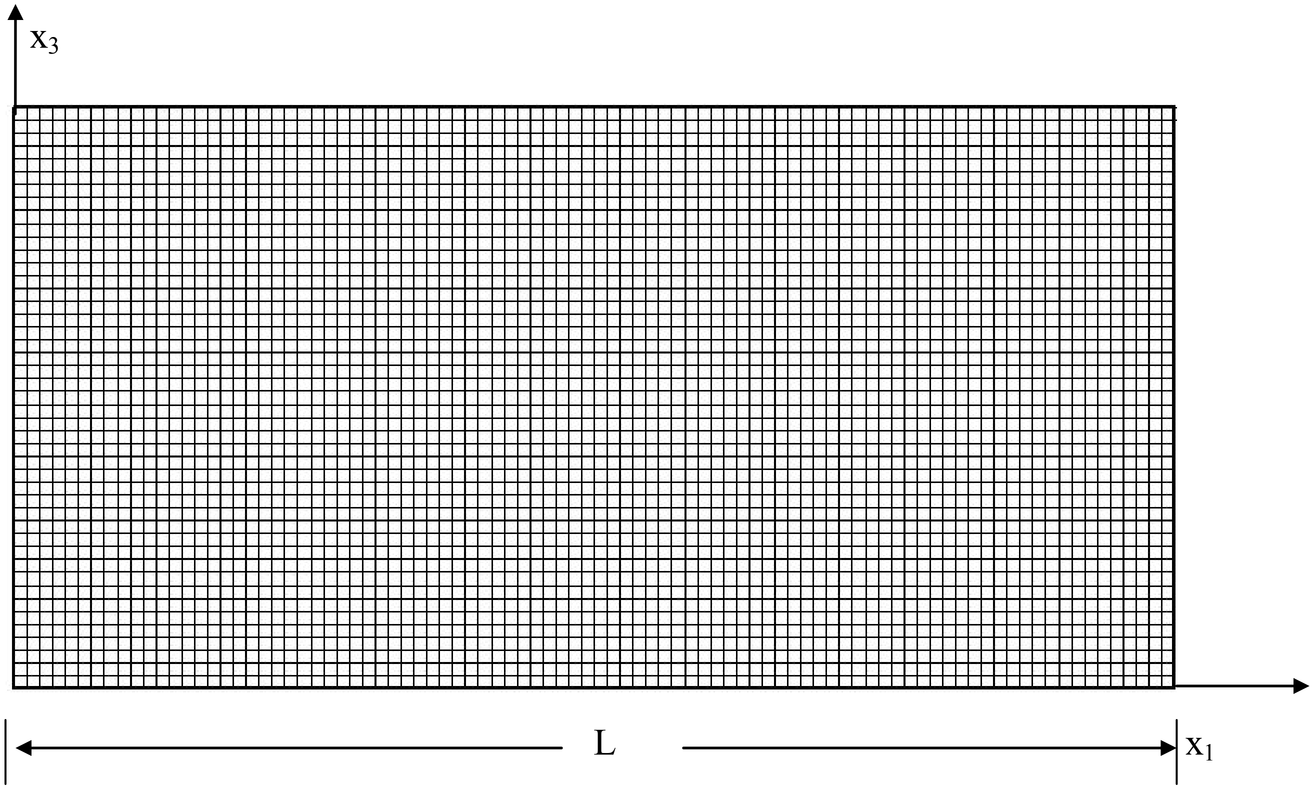

Figure 8.6 Finite element mesh and geometry of the problem.

8.2.3 Stress waves in graphite/epoxy

In order to check the validity of the code for anisotropic material, the behavior of stress waves in a graphite/epoxy plate is studied and results are compared with Kriz and Heyliger [80] . A rectangular orthotropic plate of graphite/epoxy in oriented in the x_1-x_3 plane with the fibers oriented at an angle of θ from the vertical direction (figure 8.6). The plate displacements are fixed to zero at the boundaries $x_1 = 0$ and $x_1 = L$. The other two surfaces are traction-free. This plate is modeled using a rectangular mesh of 4050 square four-noded elements in total in which 90 elements are in the x_1-direction and 45 elements are in the x_3-direction. The constants used for the constant-average acceleration Newmark method are $\delta = 0.5$ and $\alpha = 0.25$, density of graphite/epoxy is taken as 1610 Kg/m^3. After a preliminary parametric study (section 8.2.2), it was determined that a minimum of 24 elements per wavelength and 20 time increments per wave period could be used without inducing significant discretization errors. Sinusoidal displacements were imposed in the vertical (x_3) direction at 25 consecutive nodes along a bottom region of the plate for a time period of $2\text{x}10^{-05}$ sec (with a frequency of 50,000 cycles/s). The material properties used were those of graphite epoxy and are given in Table 8.1.

8.2.3.1 Results and Discussions

In order to visualize and study the wave propagation through the material both deformed mesh and energy flux contours (computed using equation (2.9)) are plotted in figure 8.7 for fiber orientation angle of 40°. Unlike an isotropic material, a wave propagating in an anisotropic material will deviate from its normal. From the energy flux contours (figure 8.7) it is clear that two waves are generated in the plate: the quasi-longitudinal wave (QL) and the quasi-shear wave (QT). As predicted by this model and that of Kriz and Heyliger [80] the QL wave is faster than the QT wave and is the first to reach the surface to be reflected. The reflected wave returns along the same path to the source of the original displacement. The energy flux contours clearly indicate that the propagation of energy by the QL and QT waves in the plate at these two different times.

When the nodes are displaced vertically energy is distributed to both QT and QL waves, however parametric studies conducted showed that if nodes are displaced horizontally (sheared) more energy can be preferentially fluxed to QT wave compared to QL wave. This is important because acoustoelastic theory predicts more flux shifts for QT wave under an applied shear stress state. Figure 8.8 shows the energy flux contours for both vertical and horizontally displaced nodes.

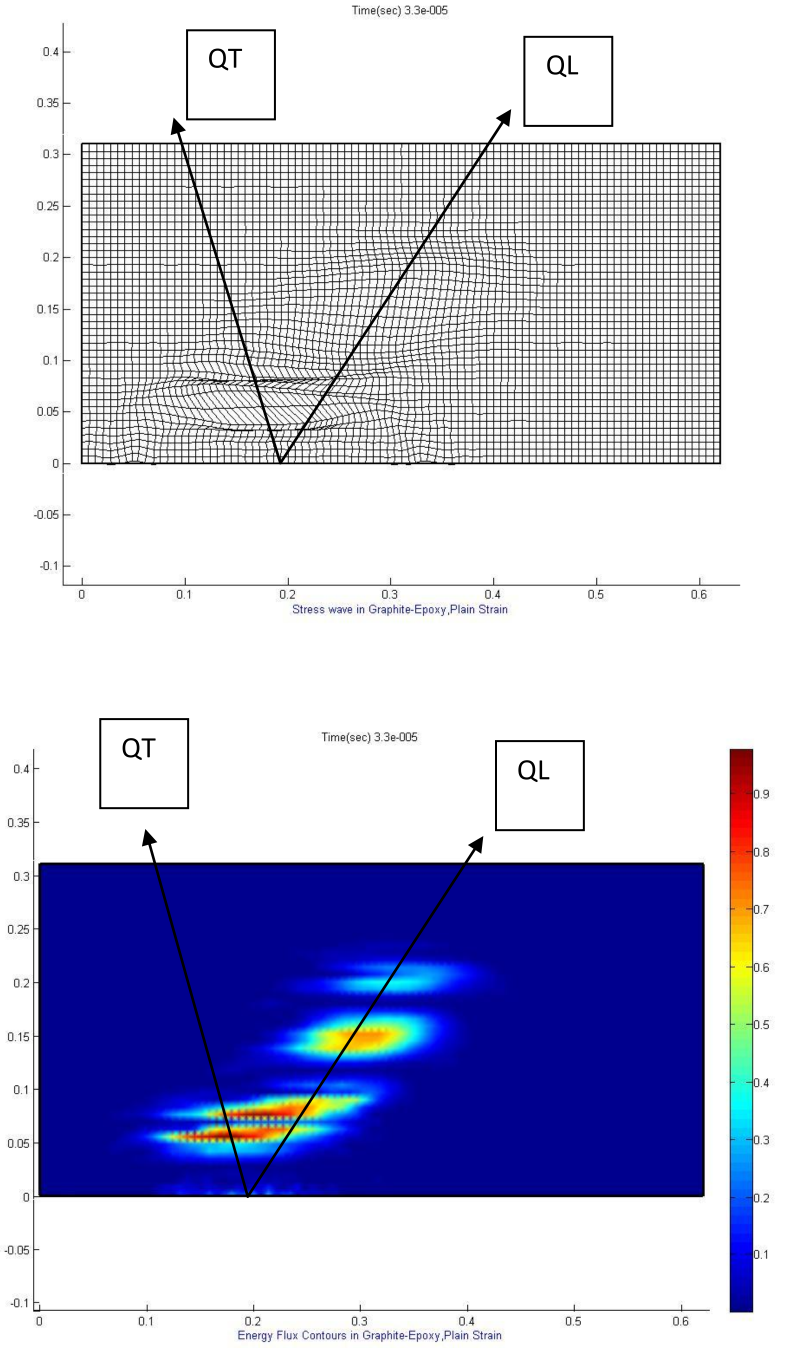

Figure 8.7 Deformed mesh and Normalized energy flux contours in gr/ep.

Fourth order elastic stiffness Components (GPa)	**Applied stress is zero (GPa)**	**Applied shear stress of 0.1 GPa. (GPa)**
C^*_{1111}	**14.26**	**14.225**
C^*_{1113}	**0**	**-0.5347**
C^*_{1311}	**0**	**-0.6347**
C^*_{1313}	**5.27**	**5.235**
C^*_{1131}	**0**	**-0.6347**
C^*_{1133}	**6.5**	**6.465**
C^*_{1331}	**5.27**	**5.235**
C^*_{1333}	**0**	**0.3983**
C^*_{3113}	**5.27**	**5.235**
C^*_{3311}	**6.5**	**6.465**
C^*_{3313}	**0**	**0.2983**
C^*_{3111}	**0**	**-0.5347**
C^*_{3133}	**0**	**0.2983**
C^*_{3131}	**5.27**	**5.235**
C^*_{3331}	**0**	**0.3983**
C^*_{3333}	**108.4**	**108.366**

Table 8.1 Material properties used for Finite element simulations.

8.3 Stress waves in graphite/epoxy due to applied shear stress

In this section the method to find the flux shift for QT wave in graphite/epoxy due to an applied shear stress from the finite element model is explained and the comparison to flux shift predicted by acoustoelastic theory is carried out.

The graphite/epoxy plate is oriented in the x_1-x_3 plane with the fibers oriented at an angle of θ from the vertical direction (figure 8.6). The plate displacements are fixed to zero at the boundaries $x_1 = 0$ and $x_1 = L$. The other two surfaces are traction-free. This plate is modeled using a rectangular mesh of 4050 square four-noded isoparametric elements in which 90 elements are in the x_1-direction and 45 elements are in the x_3-direction. The constants used for the constant-average acceleration Newmark method are $\delta = 0.5$ and $\alpha = 0.25$ density of graphite/epoxy is taken as 1610 $\mathrm{Kg/m^3}$. After a preliminary parametric study (section 8.2.2), it was determined that a minimum of 24 elements per wavelength and 20 time increments per wave period would reduce wave dispersion. Sinusoidal displacements were imposed in the horizontal (x_1) direction at 25 consecutive nodes along a bottom region of the plate for a time period of $2\text{x}10^{-05}$ sec (with a frequency of 50,000 cycles/s) in order to flux more energy in to the QT wave. The material properties used are given in table 8.1. It is evident from table 8.1 column 3 that there are additional stiffness C^*_{ijkl} components due to the applied shear stress and these are incorporated in the finite element equations. These fourth order coefficients correspond to an applied shear stress of 0.1 GPa, this stress state gives high flux shift as discussed in chapter 7. Unsymmetry of fourth order stiffness makes the element stiffness matrix unsymmetrical. Finite element simulations are conducted for 0, 10, 20, 30,40, 50 and 60 degree fiber orientation angles for both zero stress state and applied shear stress state to find the deviation angles and hence the flux shift.

8.3.1 Finding the Energy Flux Deviation

In order to find the energy flux deviation following steps are followed

(1) Draw the centerline from where the wave is propagated (Figure 8.8 a, b). Even number of elements (24) and odd number of nodes (25) makes it easier to pick exactly the middle node which is the center of the transducer.

(2) Another line is drawn through the center of the energy flux contours connecting back to the center node representing the center of transducer (Figure 8.8 (b)).

(3) If both the centerline and the line joining the center of energy flux contours coincide then the flux deviation is zero, or else the angle is measured between them.

(4) Steps 1-3 are repeated for each fiber orientation angles of 0 to 60 degrees with an increment of 10 degrees for both zero stress state and applied shear stress cases. The flux deviation angles are computed for 3 different time steps ranging from the launch of the wave from the bottom of the plate and before the wave reach the top of the plate. These values are averaged to get flux deviations and hence the flux shift.

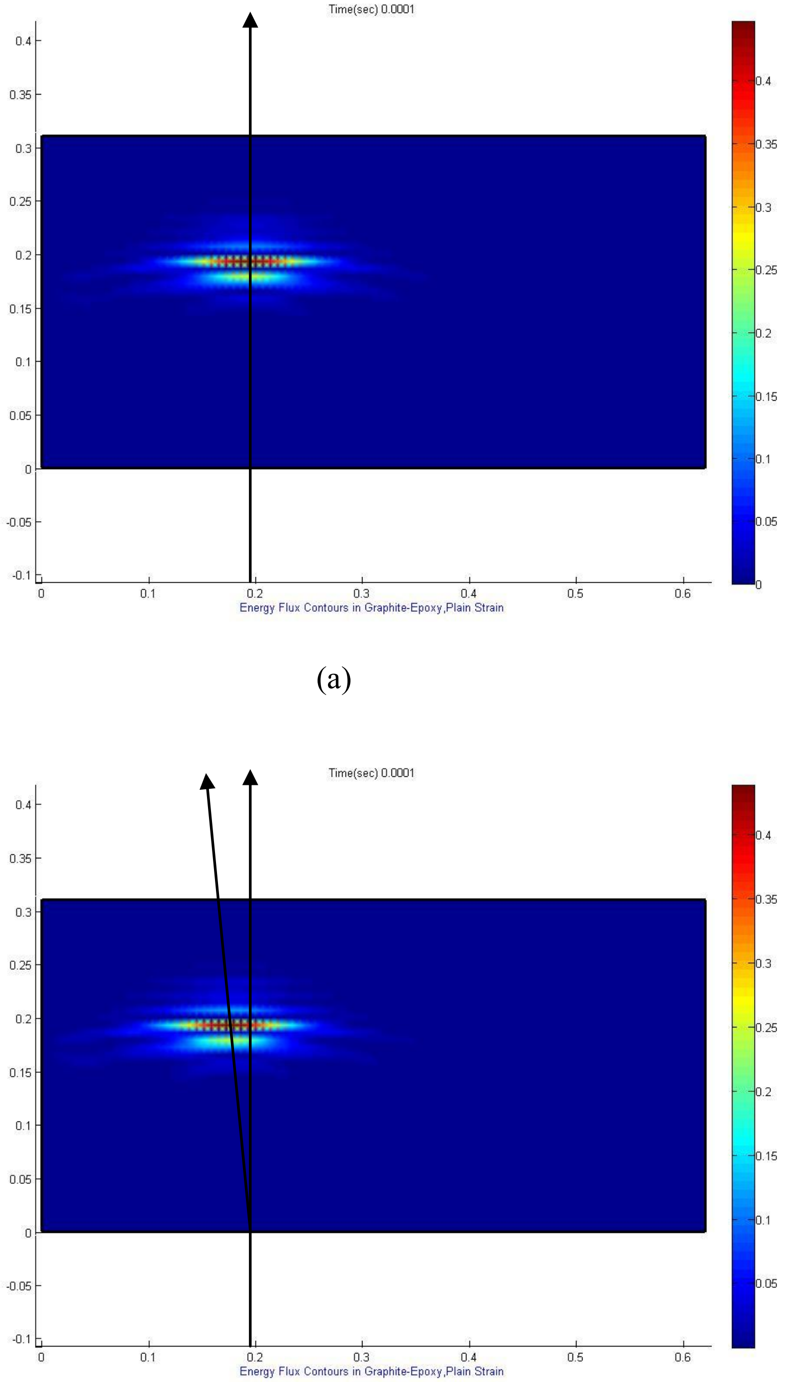

(a)

(b)

Figure 8.8 Normalized energy flux contours for (a) Zero stress state (b) Applied shear stress case for 0 degree fiber orientation. (Movie_4)

8.3.2 Results and Discussion

Due to the way in which the transducer was oscillated, it is interesting to note that no significant amount of energy is fluxed into the QL wave for low fiber orientation angles, however some when the fiber orientation angle becomes higher QL waves are visible. This is true for both zero stress state and applied stress state (Figures 8.9, 8.10). The QL wave is the fastest wave launched in the material and once it gets to the top surface it is reflected back. Figures 8.9 and 8.10 also show that the QT wave starts deviating towards the left side from the center line of the transducer for fiber orientation angle from 0 to 30 degrees. As the fiber orientation angle reaches 30 degrees QT wave starts to deviate towards the centerline of the transducer.

It is obvious from Figure 8.8b that due to the applied shear stress the energy flux deviation is not zero for the QT wave when the fiber orientation angle is 0 degrees. Hence there exists a flux shift. This is consistent with what acoustoelastic theory predicts. The QT flux shift is found for every 10 degree fiber orientation till 60 degrees using the methodology discussed in section 8.3.1. These results are plotted in figure 8.11. It is clear from figure 8.11 that the FEM predicts the trend of flux shift for QT wave due to applied shear stress. This is an independent confirmation of the flux shifts.

Since the energy is found from the stresses which are secondary variable in a finite element model, the convergence rate is slow. This can be overcome by having more elements in the mesh. However the computational cost for this will be high because the stiffness matrix is unsymmetric. To counter the computational limitations other algorithms need to be explored that can deal with unsymmetric set of equations.

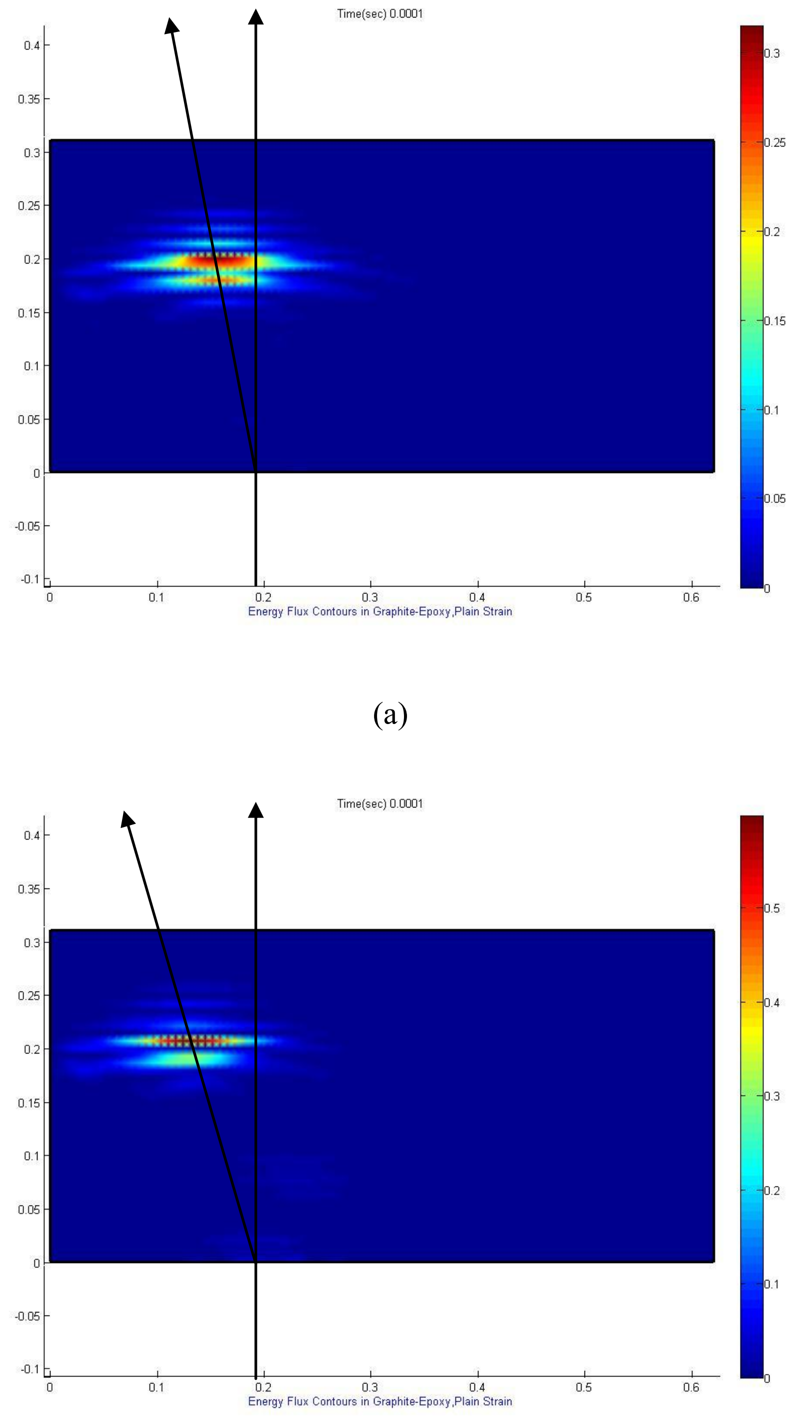

(a)

(b)

Figure 8.9 Normalized energy flux contours in Graphite/Epoxy at zero stress state for (a) 10^o (b) 20^o (c) 30^o (d) 40^o (e) 50^o (f) 60^o fiber orientation at time $1.0x10^{-04}$sec.

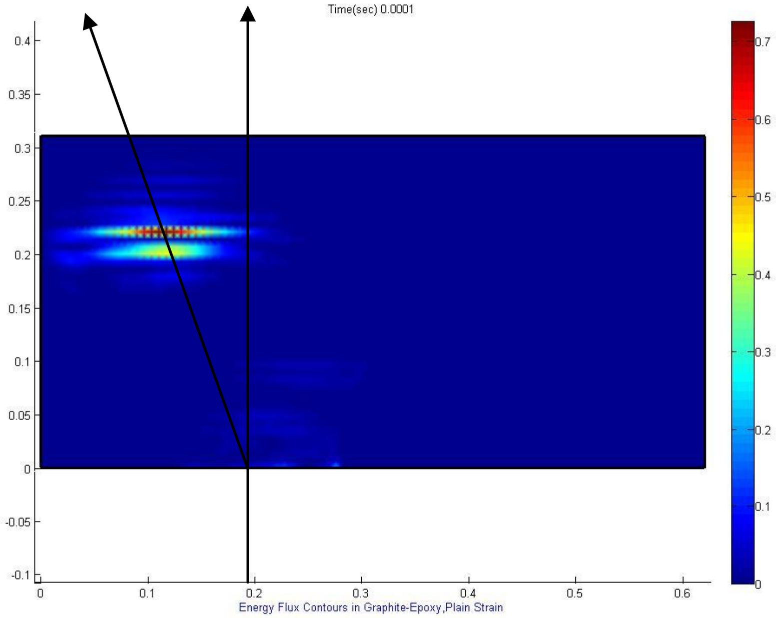
Time(sec) 0.0001
0.4
0.35
0.3
0.25
0.2
0.15
0.1
0.05
0
-0.05
-0.1
0
0.1
0.2
0.3
0.4
0.5
0.6
Energy Flux Contours in Graphite-Epoxy,Plain Strain
0.7
0.6
0.5
0.4
0.3
0.2
0.1
0

(c)

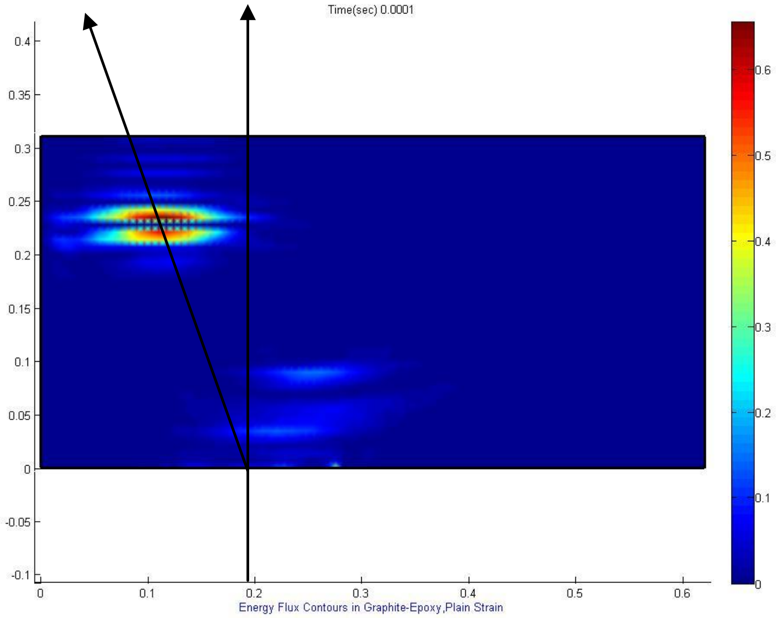
Time(sec) 0.0001
0.4
0.35
0.3
0.25
0.2
0.15
0.1
0.05
0
-0.05
-0.1
0
0.1
0.2
0.3
0.4
0.5
0.6
Energy Flux Contours in Graphite-Epoxy,Plain Strain
0.6
0.5
0.4
0.3
0.2
0.1
0

(d)

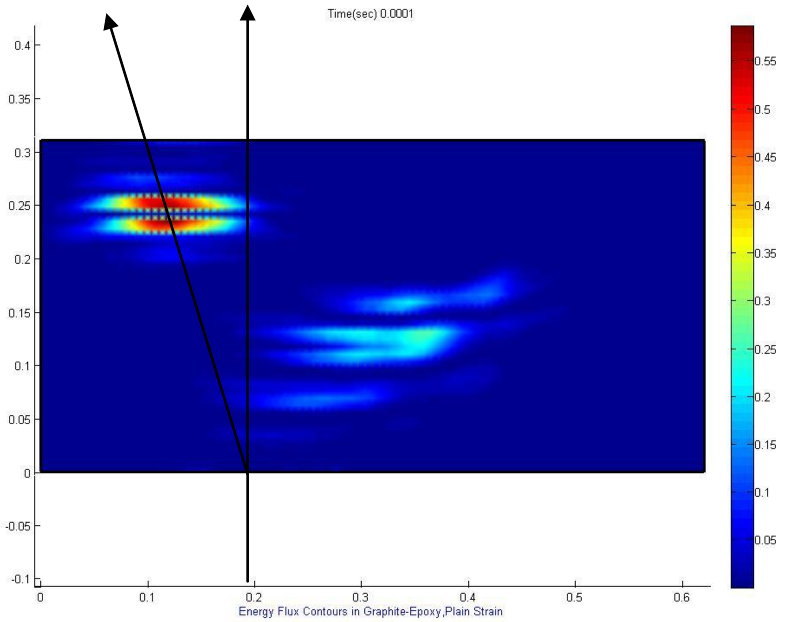
Time(sec) 0.0001
Energy Flux Contours in Graphite-Epoxy,Plain Strain
0.4
0.35
0.3
0.25
0.2
0.15
0.1
0.05
0
-0.05
-0.1
0
0.1
0.2
0.3
0.4
0.5
0.6
0.55
0.5
0.45
0.4
0.35
0.3
0.25
0.2
0.15
0.1
0.05

(e)

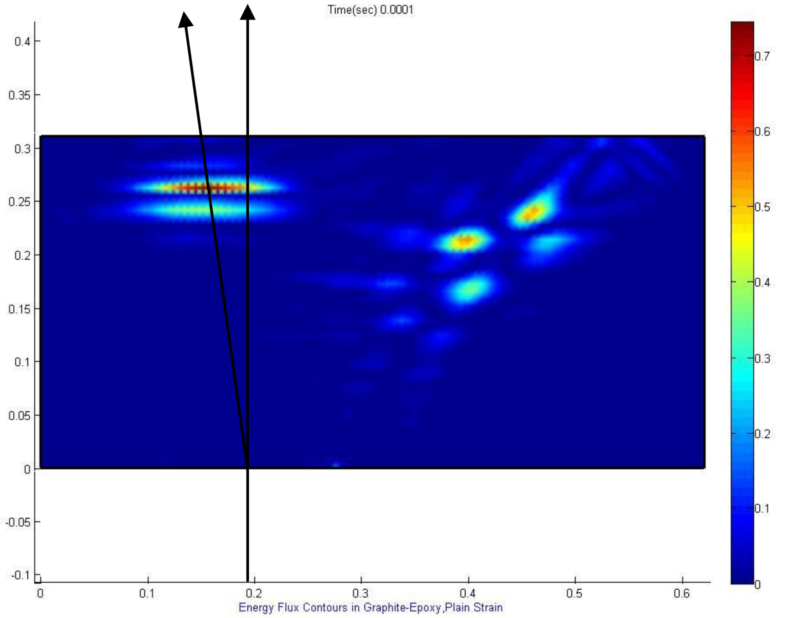
Time(sec) 0.0001
Energy Flux Contours in Graphite-Epoxy,Plain Strain
0.4
0.35
0.3
0.25
0.2
0.15
0.1
0.05
0
-0.05
-0.1
0
0.1
0.2
0.3
0.4
0.5
0.6
0.7
0.6
0.5
0.4
0.3
0.2
0.1
0

(f)

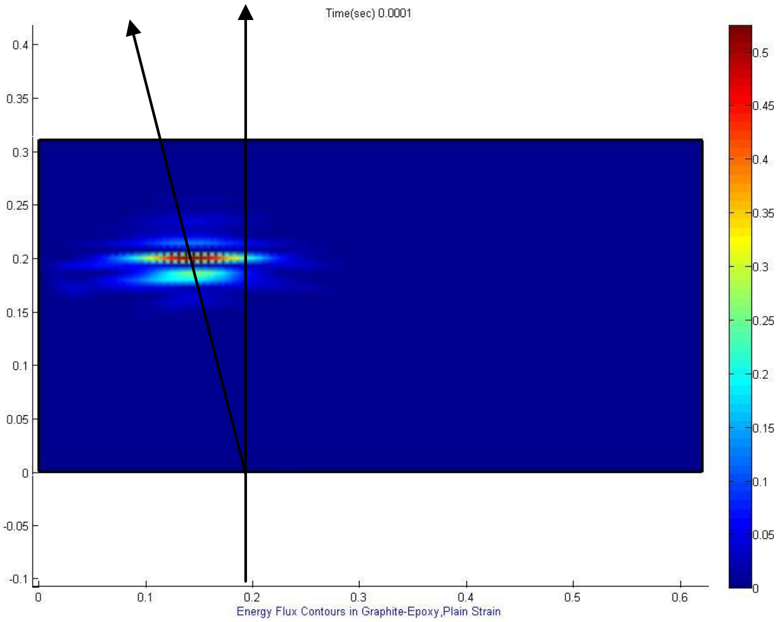

(a)

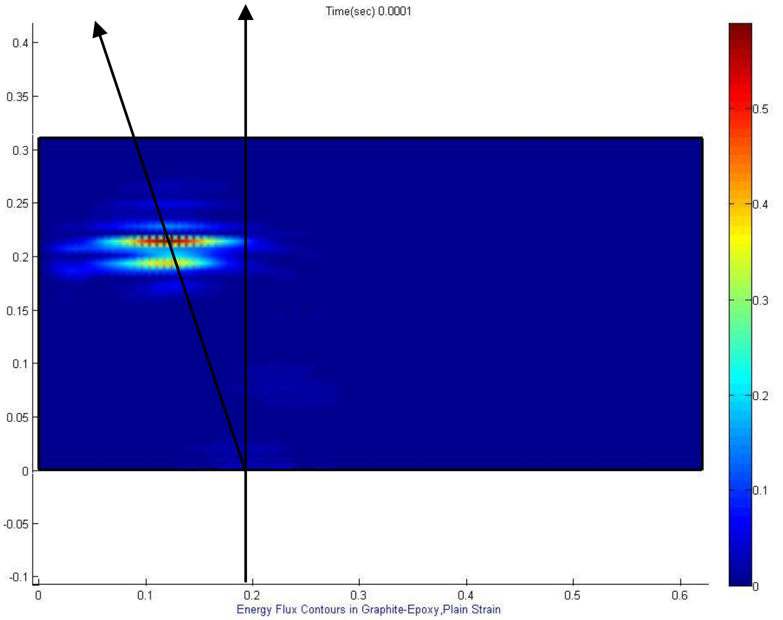

(b)

Figure 8.10 Normalized energy flux contours in Graphite/Epoxy for applied shear stress of 0.1 GPa (a) 10° (b) 20° (c) 30° (d) 40° (e) 50° (f) 60° fiber orientation at time 1.0x10^{-04}sec. (Movie_5)

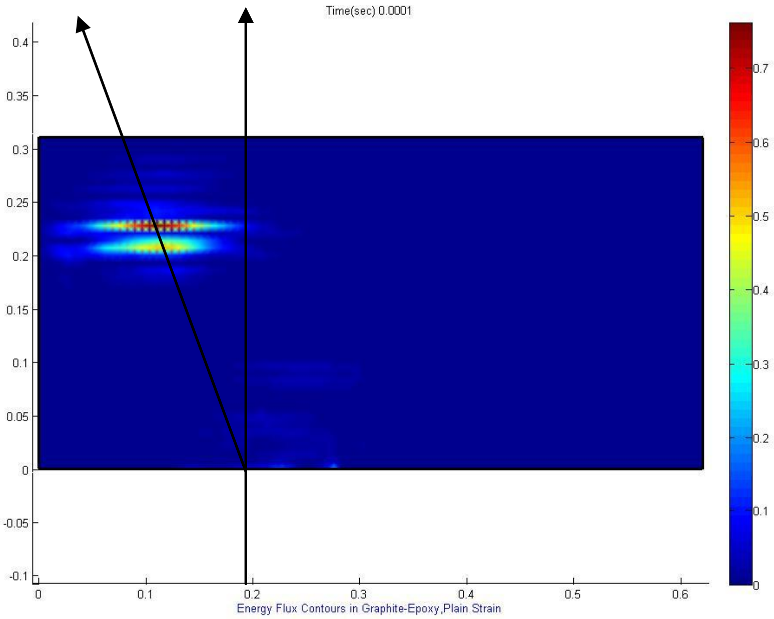
Time(sec) 0.0001
0.4
0.35
0.3
0.25
0.2
0.15
0.1
0.05
0
-0.05
-0.1
0
0.1
0.2
0.3
0.4
0.5
0.6
Energy Flux Contours in Graphite-Epoxy,Plain Strain
0.7
0.6
0.5
0.4
0.3
0.2
0.1
0

(c)

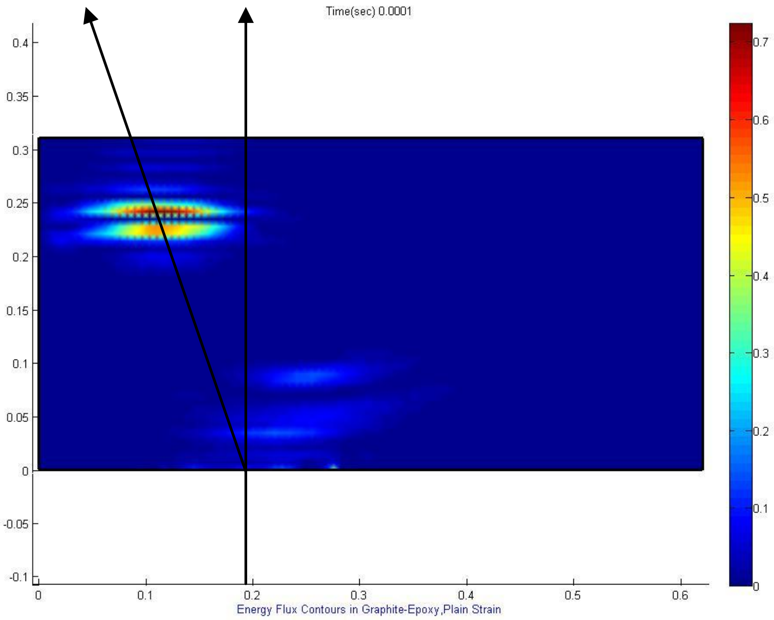
Time(sec) 0.0001
0.4
0.35
0.3
0.25
0.2
0.15
0.1
0.05
0
-0.05
-0.1
0
0.1
0.2
0.3
0.4
0.5
0.6
Energy Flux Contours in Graphite-Epoxy,Plain Strain
0.7
0.6
0.5
0.4
0.3
0.2
0.1
0

(d)

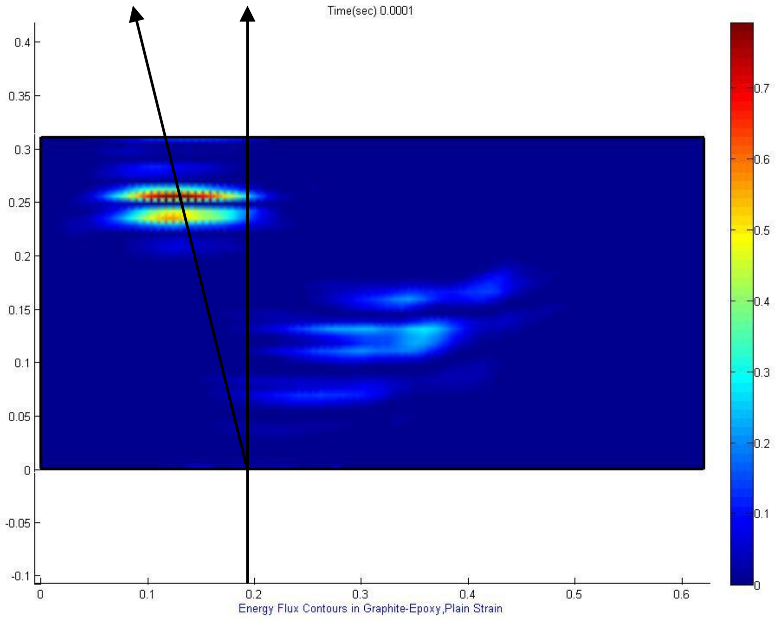
Time(sec) 0.0001
0.4
0.35
0.3
0.25
0.2
0.15
0.1
0.05
0
-0.05
-0.1
0
0.1
0.2
0.3
0.4
0.5
0.6
Energy Flux Contours in Graphite-Epoxy,Plain Strain
0.7
0.6
0.5
0.4
0.3
0.2
0.1
0

(e)

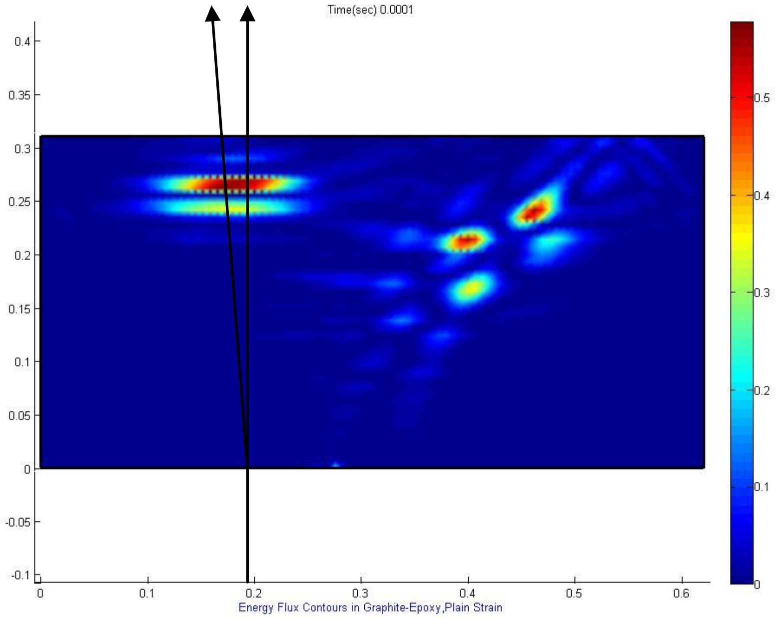
Time(sec) 0.0001
0.4
0.35
0.3
0.25
0.2
0.15
0.1
0.05
0
-0.05
-0.1
0
0.1
0.2
0.3
0.4
0.5
0.6
Energy Flux Contours in Graphite-Epoxy,Plain Strain
0.5
0.4
0.3
0.2
0.1
0

(f)

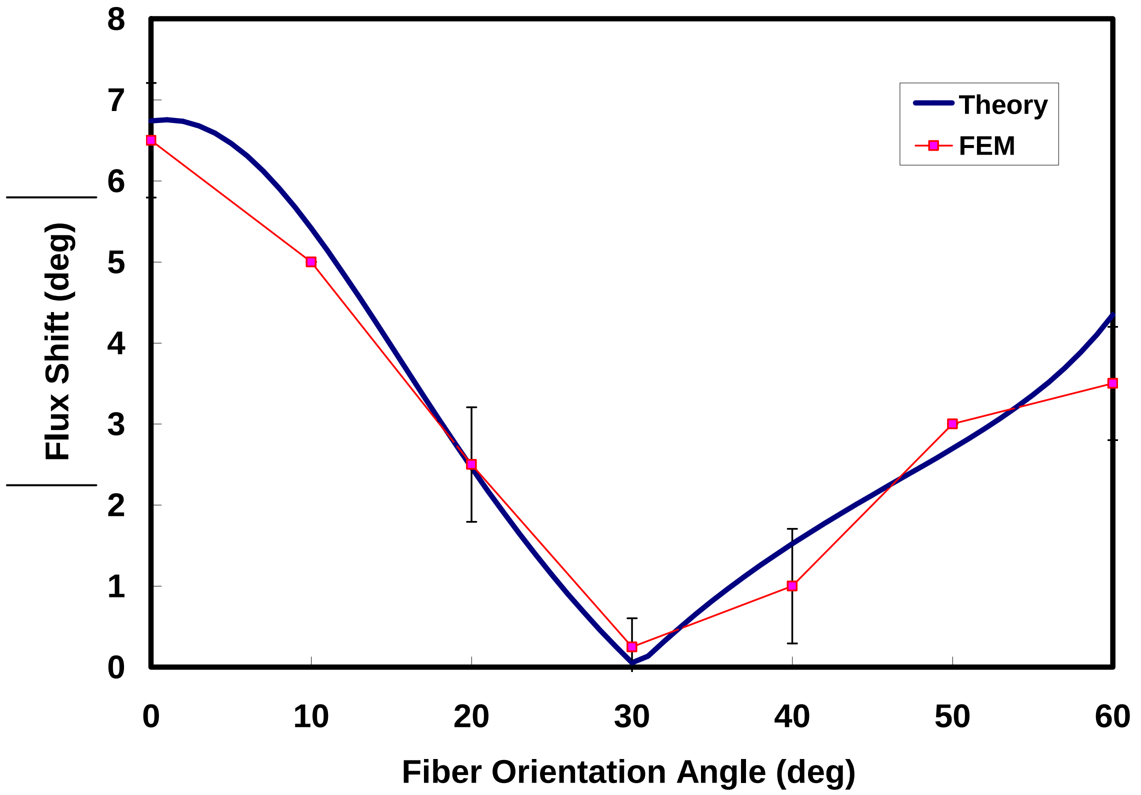

Figure 8.11 Comparison of flux shifts predicted by FEM and Acoustoelastic theory.

Chapter 9

Summary and Conclusions

9.1 Summary

In this work, several computational methods have been used to study nonlinear material behavior at nano and macro scales. At the nano scale molecular dynamics simulation was used to study the nanoindentation of Ni thin films of various thicknesses oriented in the (111) direction. These simulations included single crystals as well as films with low angle grain boundaries. The study included both elastic and plastic deformations of thin Ni films along with their deformation mechanisms. The thickness effects were described by a simple model. The indentation rate, different substrate conditions and different radius effects are also carried out. Comparison of the 20nm thick film was also carried out with simulation results for two different interatomic potentials. Finally, dynamic nanoindentation was carried out for a Ni thin

In the macro scale, acoustoelastic theory was used to study how nonlinear elastic properties of unidirectional graphite/epoxy effect the energy flux deviation due to an applied shear stress. Plane wave solutions for the christoffel equation were used to find the energy flux shift for QL, QT and PT waves for both normal and shear stresses. The finite element model of the equations of motion combined with Newmark method in time was used to confirm the flux shift predicted by acoustoelastic theory.

9.2 Conclusions

Conclusions of this research can be summed up as follows:

(i) The contact pressure necessary to emit the first dislocation is a material property in the single crystal films and is mostly independent of film thickness. For Ni described by the potential used (Voter et al) here, this value is 16 Gpa.

(ii) The deformation mechanism shows, the partial prismatic glide loop consisting of stacking-fault bounded by Shockely partials being emitted in multiple directions. These loops get reflected by the hard substrate.

(iii) The amount of dislocations emitted by thin films depends on film thickness; as the films thickness decreases so does the number of dislocations.

(iv) The elastic response of these thin films does not follow the Hertzian solution for indentation depths that are larger than 2.5% of the film thickness. Our results for indentations up to 20% of the film thickness indicate that thinner films require a higher force to achieve the same indentation depth than the thicker films. As the film thickness increases the slope of the elastic response of the film decreases.

(v) The contact pressure necessary to emit the first dislocation is a material property in the single crystal films and is mostly independent of film thickness. For Ni described by the potential used (Mishin et al) here this value is 28 Gpa. However, the forces and indentation depths that are required to achieve this contact pressure do depend on the film thickness.

(vi) Low angle grain boundaries perpendicular to the film surface in the thinnest films studied (4 nm) did not act as an effective site for emitting dislocations. This can be attributed to the fact that in these very thin films the possible emission of loops out of the grain boundary is limited by the thickness of the film. As the film thickness increases, the loops are observed to be emitted from these grain boundaries. Fitting these results to a simple model, we can conclude that the formation of dislocations in these boundaries required about half the stress necessary to form dislocations in the bulk (about 14 Gpa for Ni described by the potential), but an additional stress is required for this dislocation to be emitted into the crystal as a loop. This latter part can be significant in thin films, where the loop diameters are limited by the film thickness.

(vii) The contact pressures that were observed after the emission of the initial dislocation burst and found that these are not significantly affected by the presence of the low angle grain boundaries, but are significantly dependent on the film thickness. The initial burst relieves more stress as the film thickness increases.

(viii) Different indentation rates have hardly any effect on hardness value. Two boundary conditions studied in this work shows that one has strain hardening in the plastic region other one doesn’t show that. The different radius also has hardly any effect on the hardness value.

(ix) Comparison with experiments shows excellent agreement of hardness data with Voter- Chen interatomic potentials.

(x) Dynamic nanoindentation shows that there are more (12%) dislocations compared to quasi-static case.

(xi) The QL and QT waves exhibit flux deviation in gr/ep at zero shear stress due to the anisotropy of the material. Flux deviation of the PT wave is negligible as expected.

(xii) The application of normal stresses to gr/ep leads to flux shifts in QL, QT and PT from zero stress states with the QT wave having larger shift compared to QL and PT.

(xiii) The application of the shear stress also leads to flux deviation in QL, QT and PT waves, but QT has higher flux shift compared to QL and PT. The QT wave has significant flux shift at 0^o and 90^o due to the applied shear stress; whereas the flux shift of the QT wave under a normal stress at 0^o and 90^o is zero.

(xiv) The flux shift in the QT wave due to applied shear stress is much higher than that of flux shift in the QT wave due to normal stresses.

(xv) The flux shift has a linear variation with the applied shear stress.

(xvi) Finite element results reproduce the flux shift trend in the QT wave for fiber orientation angles of 0 to 60 degrees thus confirming the flux shift predicted by theory.

References

1. Landolt-Bornstein, *Numerical Data and Functional Relationships in Science and Technology (Group III: Crystal and Solid State Physics).* Springer-Verlag, New York., 1969. **Volume 2**.
2. Love, A.E.H., *A Treatise on the Mathematical Theory Elasticity*. 1944, New York: Dover.
3. Musgrave, M.J.P., *Crystal Acoustics*. 1970, San Francisco: Holden-Day.
4. Green, R.E.J., *Treatise on Materials Science and Technology*. Ultrasonic Investigation of Mechanical Properties, ed. H. Herman. Vol. 3. 1973, New York: Academic Press.
5. Kriz, R.D. and W.W. Stinchcomb, *Elastic-Moduli of Transversely Isotropic Graphite Fibers and Their Composites.* Experimental Mechanics, 1979. **19**(2): p. 41-49.
6. Prosser, W.H., *Ultrasonic Characterization of the Nonlinear Elastic Properties of Unidirectional Graphite/Epoxy Composites*. 1987, Johns Hopkins University: Baltimore, MD.
7. Prosser, W.H., R.D. Kriz, and D.W. Fitting, *Effect of Stress on Energy Flux Deviation of Ultrasonic-Waves in Gr/Ep Composites*, in *Ieee 1990 Ultrasonics Symposium : Proceedings, Vols 1-3*, B.R. McAvoy, Editor. 1990. p. 961-964.
8. Gerberich, W.W., et al., *Indentation induced dislocation nucleation: The initial yield point.* Acta Materialia, 1996. **44**(9): p. 3585-3598.
9. Volinsky, A.A. and W.W. Gerberich, *Nanoindentaion techniques for assessing mechanical reliability at the nanoscale.* Microelectronic Engineering, 2003. **69**(2-4): p. 519-527.
10. Weertman, J.R., et al., *Structure and mechanical behavior of bulk nanocrystalline materials.* MRS Bulletin, 1999. **24**(2): p. 44-50.
11. Van Swygenhoven, H., D. Farkas, and A. Caro, *Grain-boundary structures in polycrystalline metals at the nanoscale.* Physical Review B, 2000. **62**(2): p. 831-838.
12. Van Swygenhoven, H., A. Caro, and D. Farkas, *Grain boundary structure and its influence on plastic deformation of polycrystalline FCC metals at the nanoscale: A molecular dynamics study.* Scripta Materialia, 2001a. **44**(8-9): p. 1513-1516.
13. Van Swygenhoven, H., A. Caro, and D. Farkas, *A molecular dynamics study of polycrystalline FCC metals at the nanoscale: grain boundary structure and its influence on plastic deformation.* Materials Science and Engineering a-Structural Materials Properties Microstructure and Processing, 2001b. **309**: p. 440-444.
14. Schiotz, J. and K.W. Jacobsen, *A maximum in the strength of nanocrystalline copper.* Science, 2003. **301**(5638): p. 1357-1359.
15. Schiotz, J., *Atomic-scale modeling of plastic deformation of nanocrystalline copper.* Scripta Materialia, 2004. **51**(8): p. 837-841.
16. Espinosa, H.D., B.C. Prorok, and B. Peng, *Plasticity size effects in free-standing submicron polycrystalline FCC films subjected to pure tension.* Journal of the Mechanics and Physics of Solids, 2004. **52**(3): p. 667-689.
17. Espinosa, H.D., et al., *Discrete dislocation dynamics simulations to interpret plasticity size and surface effects in freestanding FCC thin films.* International Journal of Plasticity, 2006. **22**(11): p. 2091-2117.

18. Zong, Z., et al., *Indentation size effects in the nano- and micro-hardness of fcc single crystal metals.* Materials Science and Engineering a-Structural Materials Properties Microstructure and Processing, 2006. **434**(1-2): p. 178-187.
19. Christopher, D., R. Smith, and A. Richter, *Atomistic modelling of nanoindentation in iron and silver.* Nanotechnology, 2001. **12**(3): p. 372-383.
20. Li, J., et al., *Atomistic mechanisms governing elastic limit and incipient plasticity in crystals.* Nature, 2002. **418**(6895): p. 307-310.
21. Lilleodden, E.T., et al., *Atomistic simulations of elastic deformation and dislocation nucleation during nanoindentation.* Journal of the Mechanics and Physics of Solids, 2003. **51**(5): p. 901-920.
22. Iglesias, R.A. and E.P.M. Leiva, *Two-grain nanoindentation using the quasicontinuum method: Two-dimensional model approach.* Acta Materialia, 2006. **54**(10): p. 2655-2664.
23. Kim, K.J., et al., *Molecular dynamics simulation of dislocation behavior during nanoindentation on a bicrystal with a Sigma=5 (210) grain boundary.* Materials Letters, 2006. **60**(28): p. 3367-3372.
24. Lee, Y.M., et al., *Atomistic simulations of incipient plasticity under A1(111) nanoindentation.* Mechanics of Materials, 2005. **37**(10): p. 1035-1048.
25. Ma, X.L. and W. Yang, *Molecular dynamics simulation on burst and arrest of stacking faults in nanocrystalline Cu under nanoindentation.* Nanotechnology, 2003. **14**(11): p. 1208-1215.
26. Shiari, B., R.E. Miller, and W.A. Curtin, *Coupled atomistic/discrete dislocation simulations of nanoindentation at finite temperature.* Journal of Engineering Materials and Technology-Transactions of the ASME, 2005. **127**(4): p. 358-368.
27. Szlufarska, I., *Atomistic simulations of nanoindentation.* Materials Today, 2006. **9**(5): p. 42-50.
28. Schuh, C.A., *Nanoindentation studies of materials.* Materials Today, 2006. **9**(5): p. 32-40.
29. Hasnaoui, A., P.M. Derlet, and H. Van Swygenhoven, *Interaction between dislocations and grain boundaries under an indenter - a molecular dynamics simulation.* Acta Materialia, 2004. **52**(8): p. 2251-2258.
30. Parakala, P., et al., *Effects of thickness and indenter geometry in nanoindentation of nickel thin films*, in *Thin Films-Stresses and Mechanical Properties X*, S.G. Corcoran, et al., Editors. 2004. p. 355-360.
31. Nix, W.D. and H.J. Gao, *Indentation size effects in crystalline materials: A law for strain gradient plasticity.* Journal of the Mechanics and Physics of Solids, 1998. **46**(3): p. 411-425.
32. Huang, Y., et al., *A model of size effects in nano-indentation.* Journal of the Mechanics and Physics of Solids, 2006. **54**(8): p. 1668-1686.
33. Cordill, M.J., et al., *Plasticity responses in ultra-small confined cubes and films.* Acta Materialia, 2006. **54**(17): p. 4515-4523.
34. Zhang, F., et al., *Indentation of a hard film on a soft substrate: Strain gradient hardening effects.* International Journal of Plasticity, 2007. **23**(1): p. 25-43.
35. Saha, R., et al., *Indentation of a soft metal film on a hard substrate: strain gradient hardening effects.* Journal of the Mechanics and Physics of Solids, 2001. **49**(9): p. 1997-2014.

36. Abu Al-Rub, R.K. and G.Z. Voyiadjis, *Analytical and experimental determination of the material intrinsic length scale of strain gradient plasticity theory from micro- and nano-indentation experiments*. International Journal of Plasticity, 2004. **20**(6): p. 1139-1182.
37. Qu, S., et al., *The indentation size effect in the spherical indentation of iridium: A study via the conventional theory of mechanism-based strain gradient plasticity*. International Journal of Plasticity, 2006. **22**(7): p. 1265-1286.
38. Chen, S.H., L. Liu, and T.C. Wang, *Size dependent nanoindentation of a soft film on a hard substrate*. Acta Materialia, 2004. **52**(5): p. 1089-1095.
39. Haile, J.M., *Molecular dynamics simulation:elementary methods*. 1992, New York: Wiley.
40. Rapaport, D.C., *The art of molecular dynamics simulation*. Second ed. 2004, Cambridge: Cambridge University Press.
41. Allen, M.P., Tildesley, D.J, *Computer Simulation of Liquids*. Oxford Science Publications, 1987.
42. Plimpton, S., *Fast Parallel Algorithms for Short-Range Molecular-Dynamics*. Journal of Computational Physics, 1995. **117**(1): p. 1-19.
43. Daw, M.S. and M.I. Baskes, *Embedded-Atom Method - Derivation and Application to Impurities, Surfaces, and Other Defects in Metals*. Physical Review B, 1984. **29**(12): p. 6443-6453.
44. Finnis, M., *Interatomic Forces in Condensed Matter*. Oxford University Press, 2003: p. 129-186.
45. Mishin, Y., et al., *Interatomic potentials for monoatomic metals from experimental data and ab initio calculations*. Physical Review B, 1999. **59**(5): p. 3393-3407.
46. Voter, A.F., Chen, S.P, *High temperature ordered intermetallic alloys*. MRS Symposia Proceedings. **82**: p. 175.
47. Tokuoka, T., Iwashimizu, Y., International Journal of Solids Structures, 1968. **4**(383).
48. Man, C.S. and W.Y. Lu, *Towards an Acoustoelastic Theory for Measurement of Residual-Stress*. Journal of Elasticity, 1987. **17**(2): p. 159-182.
49. Degtyar, A.D. and S.I. Rokhlin, *Absolute Stress Determination in Orthotropic Materials from Angular Dependences of Ultrasonic Velocities*. Journal of Applied Physics, 1995. **78**(3): p. 1547-1556.
50. Degtyar, A.D. and S.I. Rokhlin, *Stress effect on boundary conditions and elastic wave propagation through an interface between anisotropic media*. Journal of the Acoustical Society of America, 1998. **104**(4): p. 1992-2003.
51. Zhuk, Y.A. and I.A. Guz, *Influence of prestress on the velocities of plane waves propagating normally to the layers of nanocomposites*. International Applied Mechanics, 2006. **42**(7): p. 729-743.
52. Parnell, W.J., *Effective wave propagation in a prestressed nonlinear elastic composite bar*. IMA Journal of Applied Mathematics, 2007. **72**(2): p. 223-244.
53. Barnett, D., Private communications, 1990.
54. Reddy, J.N., *An Introduction to the Finite Element Method*. McGraw-Hill International Editions, USA., 1993. **Second Edition**.
55. Bathe, K.J.a.W., E.L, *Numerical Methods in Finite Element Analysis*. Prentice-Hall, Englewood Cliffs, New Jersey, 1976.

56. Reddy, J.N., *Energy and Variational Methods in Applied Mechanics.* John Wiley and Sons, New York, 1984.
57. Voter, A.F., Chen, S.P, *High temperature ordered intermetallic alloys* MRS Symposia Proceedings, 1987. **82**: p. 175.
58. Kelchner, C.L., S.J. Plimpton, and J.C. Hamilton, *Dislocation nucleation and defect structure during surface indentation.* Physical Review B, 1998. **58**(17): p. 11085-11088.
59. Johnson, K.L., *Contact Mechanics.* Cambridge University Press, 1985.
60. Pan, D., T.G. Nieh, and M.W. Chen, *Strengthening and softening of nanocrystalline nickel during multistep nanoindentation.* Applied Physics Letters, 2006. **88**(16).
61. Uchic, M.D., et al., *Sample dimensions influence strength and crystal plasticity.* Science, 2004. **305**(5686): p. 986-989.
62. Greer, J.R., W.C. Oliver, and W.D. Nix, *Size dependence of mechanical properties of gold at the micron scale in the absence of strain gradients.* Acta Materialia, 2005. **53**(6): p. 1821-1830.
63. Volkert, C.A. and E.T. Lilleodden, *Size effects in the deformation of sub-micron Au columns.* Philosophical Magazine, 2006. **86**(33-35): p. 5567-5579.
64. Swadener, J.G., E.P. George, and G.M. Pharr, *The correlation of the indentation size effect measured with indenters of various shapes.* Journal of the Mechanics and Physics of Solids, 2002. **50**(4): p. 681-694.
65. Lilleodden, E.T. and W.D. Nix, *Microstructural length-scale effects in the nanoindentation behavior of thin gold films.* Acta Materialia, 2006. **54**(6): p. 1583-1593.
66. Hirth, J.P., Lothe, J, *Theory of Dislocations.* John Wiley & Sons, Inc, 1982. **second edition**.
67. Fischer-Cripps, A.C., *Nanoindentation.* Springer, 2002.
68. Saha, R. and W.D. Nix, *Effects of the substrate on the determination of thin film mechanical properties by nanoindentation.* Acta Materialia, 2002. **50**(1): p. 23-38.
69. Wang, H.R. and C.W. Ong, *Determination of film-only hardness by eliminating the effects of elastic deformation of substrate.* Surface & Coatings Technology, 2006. **200**(14-15): p. 4433-4439.
70. Hay, J.L., M.E. O'Hern, and W.C. Oliver, *The importance of contact radius for substrate-independent property measurement of thin films*, in *Fundamentals of Nanoindentation and Nanotribology*, N.R. Moody, et al., Editors. 1998. p. 27-32.
71. Lu, C.J. and D.B. Bogy, *The Effect of Tip Radius on Nano-Indentation Hardness Tests.* International Journal of Solids and Structures, 1995. **32**(12): p. 1759-1770.
72. Cheng, Y.T., W.Y. Ni, and C.M. Cheng, *Nonlinear analysis of oscillatory indentation in elastic and viscoelastic solids.* Physical Review Letters, 2006. **97**(7).
73. Fischer-Cripps, A.C., *Multiple-frequency dynamic nanoindentation testing.* Journal of Materials Research, 2004. **19**(10): p. 2981-2988.
74. Komvopoulos, K. and W. Yan, *Molecular dynamics simulation of single and repeated indentation.* Journal of Applied Physics, 1997. **82**(10): p. 4823-4830.
75. Cheong, W.C.D. and L.C. Zhang, *Effect of repeated nano-indentations on the deformation in monocrystalline silicon.* Journal of Materials Science Letters, 2000. **19**(5): p. 439-442.

76. Cordill, M.J., Houston, J., Lund,M.S, Leighton, C., Nair, A.K, Farkas, D., Warren, O., Asif, S., Moody, N.R, Gerberich, W.W, *The Nano-Jackhammer Effect in Probing Near-Surface Mechanical Properties (Submitted).* 2007.
77. Voter, A.F., Chen, S.P, *High temperature ordered intermetallic alloys.* MRS Symposia Proceedings, 1987. **82**: p. p.175.
78. Kriz, R.D., Ledbetter, H.M, *Elastic-wave surfaces in anisotropic media.* Rheology of anisotropic materials, 1986: p. 79-92.
79. Kriz, R.D. *Solid Mechanics Research for Quantitative Nondestructive Evaluation*. in 1987. Boston: Martinus Nijfoff.
80. Kriz, R.D., Heyliger, P.R, *Finite Element Model of Stress Wave Topology in Unidirectional Graphite/Epoxy: Wave Velocities and Flux Deviations.* Review of Progress in Quantitative Nondestructive Evaluation, 1989. **8A**: p. 141-148.
81. Nair, A.K. and P.R. Heyliger, *Elastic waves in combinatorial material libraries.* Wave Motion, 2006. **43**(7): p. 529-543.
82. Meirovitch, L., *Analytical methods in vibrations.* Macmillan, New York., 1967.

APPENDIX A

A.1 Assumptions involved in predicting energy flux deviation using Acoustoelastic theory

The main assumptions used in predicting energy flux deviation in graphite/epoxy using Acoustoelastic theory involves a choice of a unidirectional fiber orientation. This choice offers the highest elastic symmetry and therefore is the least complex orientation to analyze. The fibers are randomly distributed in the x_2-x_3 plane (Figure 1) which ensures the elastic symmetry of unidirectional fiber reinforced composite. More over a transversely isotropic material is one which has a preferred axis, perpendicular to which is a plane in which the material behaves in an elastically isotropic fashion. In this case the fiber axis (x_3) is the axis with a much larger elastic stiffness, so the isotropic plane is the plane perpendicular to x_3 axis (x_2-x_3 plane).

A transversely isotropic material has five linear elastic moduli (same as for hexagonal single crystal) and nine nonlinear moduli. The five linear elastic coefficients have the following relation with other moduli.

$$\begin{aligned} C_{11} &= C_{22} \\ C_{13} &= C_{23} \qquad\qquad (A.1) \\ C_{44} &= C_{55} \\ C_{66} &= 1/2(C_{11} - C_{12}) \end{aligned}$$

The reductions of components are possible due to the symmetry of stress and strain tensors, the existence of strain energy function and taking in to consideration of material symmetries. Similarly for the nonlinear elastic moduli the relations are

$$
\begin{aligned}
&C_{111} = C_{222}, && C_{355} = C_{344} \\
&C_{223} = C_{113}, && C_{166} = C_{266} = 1/4(C_{111} - C_{112}) \\
&C_{255} = C_{144}, && C_{233} = C_{133} \\
&C_{244} = C_{155}, && C_{366} = 1/2(C_{113} - C_{123}) \\
&C_{122} = C_{112}, && C_{456} = 1/2(C_{155} - C_{144})
\end{aligned}
\tag{A.2}
$$

All other linear elastic and nonlinear elastic coefficients are zero.

A.2 Validation of code

In order to validate the code that computes the new stiffness coefficients due to applied stresses. Equation (2.7) and (2.8) are expanded out by hand and compared with the computer output results. The C^*_{nlij} term that is selected for this is checking is C^*_{1113}. The applied shear stress $\sigma_{13} = 0.1$ GPa. So equation (2.7) can be written as

$$C^*_{1113} = K_{1113} + \sigma_{13}\delta_{11}$$

In order to find the K tensor terms equation (2.8) is expanded out. First the linear elastic terms are expanded and then the nonlinear terms. The applied shear stress of 0.1 GPa leads to a shear strain of $\varepsilon_{13} = \varepsilon_{31} = 0.0095$ (This was computed using the Hooke's law). All other strain tensor terms are zero.

First non zero linear elastic term: C_{1113}

Second non zero linear elastic term: $C_{3113}\varepsilon_{13}$

Third non zero linear elastic term: $C_{1313}\varepsilon_{13}$

Fourth non zero linear elastic term: $C_{1133}\varepsilon_{13}$

Fifth non zero linear elastic term: $C_{1111}\varepsilon_{31}$

First non zero nonlinear elastic term: $C_{111313}\varepsilon_{13} + C_{111331}\varepsilon_{31}$

Second non zero nonlinear elastic term: $C_{311331}\varepsilon_{31}\ \varepsilon_{13}$

Third non zero nonlinear elastic term: $C_{131331}\varepsilon_{31}\varepsilon_{13} + C_{131313}\varepsilon_{13}\varepsilon_{13}$

Fourth non zero nonlinear elastic term: $C_{113313}\varepsilon_{13}\varepsilon_{13} + C_{113331}\varepsilon_{31}\varepsilon_{13}$

Fifth non zero nonlinear elastic term: $C_{111113}\varepsilon_{13}\varepsilon_{31} + C_{111131}\varepsilon_{31}\varepsilon_{31}$

In table A.1 the comparison of K tensor and C^* tensor for normal stress and shear stress are shown. The numbers marked in red color are the additional terms that appear due to the application of shear stress. These additional terms are indeed responsible for the additional flux shift that is predicted by the Acoustoelastic theory and FEM as shown in chapter 7 and 8.

(Normal stress 0.1 GPa along x_1 axis)	**(Shear stress 0.1 GPa in x_1-x_3 plane)**
K(:,:,1,1) = $\begin{matrix} 13.1420 & 0 & 0 \\ 0 & 6.3839 & 0 \\ 0 & 0 & 6.3721 \end{matrix}$	K(:,:,1,1) = $\begin{matrix} 14.2246 & 0 & -0.6347 \\ 0 & 6.7680 & 0 \\ -0.6347 & 0 & 6.4654 \end{matrix}$
K(:,:,2,1) = $\begin{matrix} 0 & 3.6315 & 0 \\ 3.6315 & 0 & 0 \\ 0 & 0 & 0 \end{matrix}$	K(:,:,2,1) = $\begin{matrix} 0 & 3.7372 & 0 \\ 3.7372 & 0 & -0.0635 \\ 0 & -0.0635 & 0 \end{matrix}$
K(:,:,3,1) = $\begin{matrix} 0 & 0 & 5.0635 \\ 0 & 0 & 0 \\ 5.0635 & 0 & 0 \end{matrix}$	K(:,:,3,1) = $\begin{matrix} -0.6347 & 0 & 5.2354 \\ 0 & -0.5078 & 0 \\ 5.2354 & 0 & 0.2983 \end{matrix}$
K(:,:,1,2) = $\begin{matrix} 0 & 3.6315 & 0 \\ 3.6315 & 0 & 0 \\ 0 & 0 & 0 \end{matrix}$	K (:,:,1,2) = $\begin{matrix} 0 & 3.7372 & 0 \\ 3.7372 & 0 & -0.0635 \\ 0 & -0.0635 & 0 \end{matrix}$
K (:,:,2,2) = $\begin{matrix} 6.3839 & 0 & 0 \\ 0 & 14.1070 & 0 \\ 0 & 0 & 7.1189 \end{matrix}$	K (:,:,2,2) = $\begin{matrix} 6.7680 & 0 & -0.5078 \\ 0 & 14.2600 & 0 \\ -0.5078 & 0 & 6.4880 \end{matrix}$
K (:,:,3,2) = $\begin{matrix} 0 & 0 & 0 \\ 0 & 0 & 5.1385 \\ 0 & 5.1385 & 0 \end{matrix}$	K (:,:,3,2) = $\begin{matrix} 0 & -0.0635 & 0 \\ -0.0635 & 0 & 5.2672 \\ 0 & 5.2672 & 0 \end{matrix}$
K (:,:,1,3) =	K (:,:,1,3) =

$\begin{matrix} 0 & 0 & 5.0635 \\ 0 & 0 & 0 \\ 5.0635 & 0 & 0 \end{matrix}$	$\begin{matrix} -0.6347 & 0 & 5.2354 \\ 0 & -0.5078 & 0 \\ 5.2354 & 0 & 0.2983 \end{matrix}$
K (:,:,2,3) =	K (:,:,2,3) =
$\begin{matrix} 0 & 0 & 0 \\ 0 & 0 & 5.1385 \\ 0 & 5.1385 & 0 \end{matrix}$	$\begin{matrix} 0 & -0.0635 & 0 \\ -0.0635 & 0 & 5.2672 \\ 0 & 5.2672 & 0 \end{matrix}$
K (:,:,3,3) =	K (:,:,3,3) =
$\begin{matrix} 6.3721 & 0 & 0 \\ 0 & 7.1189 & 0 \\ 0 & 0 & 107.1698 \end{matrix}$	$\begin{matrix} 6.4654 & 0 & 0.2983 \\ 0 & 6.4880 & 0 \\ 0.2983 & 0 & 108.3662 \end{matrix}$
(Normal stress 0.1 GPa along x_1 axis)	**(Shear stress 0.1 GPa in x_1-x_3 plane)**
C^* (:,:,1,1) =	C^* (:,:,1,1) =
$\begin{matrix} 13.2420 & 0 & 0 \\ 0 & 6.3839 & 0 \\ 0 & 0 & 6.3721 \end{matrix}$	$\begin{matrix} 14.2246 & 0 & -0.6347 \\ 0 & 6.7680 & 0 \\ -0.5347 & 0 & 6.4654 \end{matrix}$
C^* (:,:,2,1) =	C^* (:,:,2,1) =
$\begin{matrix} 0 & 3.7315 & 0 \\ 3.6315 & 0 & 0 \\ 0 & 0 & 0 \end{matrix}$	$\begin{matrix} 0 & 3.7372 & 0 \\ 3.7372 & 0 & -0.0635 \\ 0 & 0.0365 & 0 \end{matrix}$
C^* (:,:,3,1) =	C^* (:,:,3,1) =
$\begin{matrix} 0 & 0 & 5.1635 \\ 0 & 0 & 0 \\ 5.0635 & 0 & 0 \end{matrix}$	$\begin{matrix} -0.6347 & 0 & 5.2354 \\ 0 & -0.5078 & 0 \\ 5.2354 & 0 & 0.3983 \end{matrix}$
C^* (:,:,1,2) =	C^* (:,:,1,2) =

$\begin{matrix} 0 & 3.6315 & 0 \\ 3.6315 & 0 & 0 \\ 0 & 0 & 0 \end{matrix}$	$\begin{matrix} 0 & 3.7372 & 0 \\ 3.7372 & 0 & -0.0635 \\ 0 & -0.0635 & 0 \end{matrix}$
C^* (:,:,2,2) = $\begin{matrix} 6.3839 & 0 & 0 \\ 0 & 14.1070 & 0 \\ 0 & 0 & 7.1189 \end{matrix}$	C^* (:,:,2,2) = $\begin{matrix} 6.7680 & 0 & -0.5078 \\ 0 & 14.2600 & 0 \\ -0.5078 & 0 & 6.4880 \end{matrix}$
C^* (:,:,3,2) = $\begin{matrix} 0 & 0 & 0 \\ 0 & 0 & 5.1385 \\ 0 & 5.1385 & 0 \end{matrix}$	C^* (:,:,3,2) = $\begin{matrix} 0 & -0.0635 & 0 \\ -0.0635 & 0 & 5.2672 \\ 0 & 5.2672 & 0 \end{matrix}$
C^* (:,:,1,3) = $\begin{matrix} 0 & 0 & 5.0635 \\ 0 & 0 & 0 \\ 5.0635 & 0 & 0 \end{matrix}$	C^* (:,:,1,3) = $\begin{matrix} -0.5347 & 0 & 5.2354 \\ 0 & -0.5078 & 0 \\ 5.2354 & 0 & 0.2983 \end{matrix}$
C^* (:,:,2,3) = $\begin{matrix} 0 & 0 & 0 \\ 0 & 0 & 5.1385 \\ 0 & 5.1385 & 0 \end{matrix}$	C^* (:,:,2,3) = $\begin{matrix} 0 & 0.0365 & 0 \\ -0.0635 & 0 & 5.2672 \\ 0 & 5.2672 & 0 \end{matrix}$
C^* (:,:,3,3) = $\begin{matrix} 6.3721 & 0 & 0 \\ 0 & 7.1189 & 0 \\ 0 & 0 & 107.1698 \end{matrix}$	C^* (:,:,3,3) = $\begin{matrix} 6.4654 & 0 & 0.3983 \\ 0 & 6.4880 & 0 \\ 0.2983 & 0 & 108.3662 \end{matrix}$

Table A.1 Comparison of components of K and C^* tensor for normal stress and shear stress.

APPENDIX B

B.1 Description of Movies

In this section the detailed description to five movies in this dissertation are listed below.

1. Movie_1

Nanoindentation of Ni thin film of thickness 33nm oriented in [111] direction was carried out using molecular dynamics simulation. The molecular dynamics algorithm used here is as implemented in the LAMMPS code by Plimpton. The boundary conditions used are periodic in the directions that are perpendicular to the indentation force. In the direction of the indentation force a free surface boundary condition for the top of the film (red atoms) and a fixed boundary condition for the bottom of the film (red atoms) were used, representing a hard substrate. A rigid spherical indenter of radius 15 nm was used. Dislocation loops are formed under the indenter and these dislocation loops then start to grow and expand inside the film and forming prismatic partial glide loops. Each side of the loop consists of stacking-fault and is bounded by Shockley partials (blue colored atoms). The prismatic partial loops glide down to the hard substrate as the indentation depth increases and cannot penetrate the substrate, hence get reflected back.

2. Movie_2

Dispersion study of planar waves propagating through unidirectional Graphite/Epoxy in fiber orientation 0 degrees oriented parallel to the direction of propagation, with 30x60 finite element mesh. Transducer simulated using 4, 8, 12, and 16 elements per wave length over the width of the transducer. Animation synchronizes the different simulations and reveals faster wave speeds exist for larger number of elements per wave length. The FEM wave speed converges to the non dispersive (continuum) state with increasing number of elements per wave length. Note, wave propagation is highly dispersive for 4 elements per wave length, see grid in the lower right corner.

3. Movie_3

Dispersion study of planar waves propagating through unidirectional Graphite/Epoxy in fiber orientation 90 degrees oriented perpendicular to the direction of propagation, with 30x60 finite element mesh. Transducer simulated using 4, 8, 12, and 16 elements per wave length over the width of the transducer. Animation synchronizes the different simulations and reveals faster wave speeds exist for larger number of elements per wave length. The FEM wave speed converges to the non dispersive (continuum) state with increasing number of elements per wave length. Note, wave propagation is highly dispersive for 4 elements per wave length, see grid in the lower right corner.

4. Movie_4

Energy flux deviation in unidirectional Graphite/Epoxy was studied due to the nonlinear elastic effects where the nonlinearity is due to applied shear stress. The study was carried out to predict the energy flux deviation when fibers where orientated parallel to the wave propagation direction (0-degrees) both with and without applied shear stresses using the Finite Element Method (FEM) with a mesh size of 45x90. FEM simulations show that energy flux deviation for QT waves deviate when a shear stress is applied. The top figures show no flux deviation with no applied shear stress and bottom figure shows a shift of energy flux when a shear stress of 0.1 GPa is applied. To visually track the deviation of energy flux, only one cycle is launched at the simulated transducer where 24 elements are used to model one wavelength over the width of the transducer. It was determined that 24 elements per wavelength results in acceptable dispersion.

5. Movie_5

Energy flux deviation in unidirectional Graphite/Epoxy was studied due to the nonlinear elastic effects where nonlinearity is due to applied shear stress. The study was carried out to predict the energy flux deviation for different fiber orientation angles ranging from 10 to 60 degrees using the Finite Element Method with a mesh size of 45x90. FEM simulations shows that energy flux deviation for QT wave starts to deviate away from wave normal for fiber orientation angle of 10 to 30 degrees and starts to deviate towards the wave normal. There is an additional flux shift due to the applied shear stress as compared to the zero stress state.